UNIVERSITÀ DELLA CALABRIA

UNIVERSITA' DELLA CALABRIA

Dipartimento di Fisica

Dottorato di Ricerca in

Scienze e Tecnologie Fisiche, Chimiche e dei Materiali in Convenzione Università della Calabria-Consiglio Nazionale delle Ricerche

CICLO XXXI

Interplay between geometry and interaction in many-body physics

Settore Scientifico Disciplinare FIS/02

Coordinatore: Ch.mo Prof. Vincenzo Carbone

Firma Vincenzo Carbone

Supervisore/Tutor: Ch.mo Prof. Francesco Plastina

Firma Plastina Francesco

Co-Supervisore: Dott. Nicolino Biagio Lo Gullo

Firma Nicolino Biagio Lo Gullo

Dottorando: Dott. Jacopo Settino

Firma

This page is intentionally left blank.

Thesis referees:

- Prof. Hrvoje Buljan, *University Of Zagreb*;
- Prof. Tommaso Roscilde, *Ecole Normale Supérieure de Lyon.*

The Ph.D. dissertation took place on 26/04/2019.
Examination committee:

- Prof. Luigi Amico, *Università Degli Studi Di Catania*
- Prof. Roberta Citro *Università Degli Studi Di Salerno*
- Dr. Tony John George Apollaro *University of Malta*

This page is intentionally left blank.

Ed arrivò un bambino con le mani in tasca
ed un oceano verde dietro le spalle
disse: "Vorrei sapere quanto è grande il verde,
come è bello il mare, quanto dura una stanza
è troppo tempo che guardo il sole, mi ha fatto male"

– Fabrizio De André, *Oceano*

Ringraziamenti

Il lavoro i cui risultati sono presentati in questo volume si è potuto realizzare grazie al contributo di alcune persone, che vorrei menzionare nelle righe seguenti.

Il Prof. Francesco Plastina ha saputo guidarmi con estrema saggezza e comprensione durante tutto il mio percorso di studi accademici. Ho cercato di apprendere il suo approccio ampio e profondo nell'analisi e nello studio della fisica.

Il Dott. Nicola Lo Gullo mi ha seguito quotidianamente con grande dedizione; ho condiviso con lui numerosi momenti piacevoli anche al di fuori del tempo dedicato alla ricerca.

La Prof.ssa Anna Minguzzi mi ha accolto al *Laboratoire de Physique et Modélisation des Milieux Condensés* di Grenoble calorosamente, rendendo il soggiorno proficuo e intellettualmente stimolante. Ho potuto osservare la sua gestione esemplare di un grande e complesso gruppo di ricerca.

In Francia ho conosciuto persone meravigliose, con cui ho condiviso giornate emozionanti: Piero, Etienne, Nicolas, Davide, Juan, Alex e Frederik.

Ringrazio i colleghi ed amici di sempre, che mi hanno accompagnato durante gli anni del dottorato trascorsi all'Università della Calabria, con i quali ho discusso dei più svariati argomenti: Oreste Pezzi, Emanuele Mendicelli, Cristian Vacacela, Emanuele Bevacqua, Domenico Trotta, Davide Micieli, "la collega prof." Federica Chiappetta, Andrea Larosa, Ilenia Grimaldi, Francesco Cosco, Filomena Catapano, Antonello Palermo, Daniel Filice e tanti altri che non riesco ad elencare.

Vorrei ringraziare la Dott.ssa Benedetta Aquino, psicologa ed amica, la quale mi ha dato conforto in alcuni momenti difficili che ho vissuto durante questo periodo.

Da Gennaio ad Aprile del 2019, durante il periodo di revisione della tesi, sono stato "prof" presso il Liceo Scientifico e Linguistico Pitagora di Rende. Vorrei ringraziare gli studenti tutti per avermi fatto riscoprire, attraverso i loro occhi, la bellezza del meravigliarsi di fronte alla scienza.

Qualsiasi parola è insufficiente per ringraziare la mia famiglia, la quale mi ha sempre supportato ed incoraggiato in ogni mia scelta - è principalmente grazie a loro se oggi riesco a raggiungere questo traguardo - e la mia compagna Mariagiovanna, costantemente e con immenso amore al mio fianco. A loro dedico questo mio lavoro.

Contents

Abstract - Introduzione

La fisica dei sistemi di molti corpi interagenti è un campo di ricerca molto attivo a causa dei sorprendenti progressi nella realizzazione, controllo e misurazione di tali sistemi, e dell'esistenza di problemi fondamentali ancora aperti.

I gas ultrafreddi, che ora è possibile preparare in una varietà di configurazioni nei laboratori di tutto il mondo, sono emersi come candidati ideali per realizzare simulazioni altamente controllabili della fisica della materia condensata [1, 2]. In particolare, è possibile immergere e manipolare in potenziali ottici sia atomi bosonici che fermionici [3]. L'assenza di fononi termici, insieme alla controllabilità delle interazioni per mezzo delle risonanze di Feschbach [4], ha permesso lo studio dettagliato di una moltitudine di diagrammi di fase di sistemi critici, sia all'equilibrio, sia lontano da esso [5,6].

Tra tutti i sistemi che è possibile realizzare nel contesto dei gas ultrafreddi, il gas Tonks-Giradeau (TG) merita una menzione speciale [7–12]. Introdotto da Giraedeau in [13], corrisponde ad un un sistema di bosoni impenatrabili (hardcore) e coincide con il limite di interazione infinita del modello Lieb-Liniger [14, 15]. Grazie alla possibilità di mappare la funzione d'onda di un gas di TG con uno di fermioni non interagenti, è stato possibile studiarne diverse sfaccettature: distribuzione dei momenti [16–20], matrice densità ridotta [17, 19–28] e proprietà dinamiche non di equilibrio [29–34].

Oltre alla capacità di ingegnerizzare e sintonizzare l'interazione, una caratteristica particolarmente interessante degli atomi freddi è la possibilità di manipolare la forma del potenziale esterno, caratteristica essenziale per le simulazioni di fisica della materia condensata. In pratica, qualsiasi geometria reticolare può essere realizzata con potenziali ottici, ingegnerizzando direzione, lunghezza d'onda, intensità, polarizzazione e fase del raggio laser. Anche la dimensionalità del sistema può essere modificata. Ad esempio, partendo da un sistema 3D, un reticolo di sistemi 1D (2D) può essere generat da un reticolo ottico 2D (1D). Le dinamiche sulle direzioni indesiderate vengono congelate utilizzando un potenziale di confinamento sufficientemente forte. Inoltre, l'aggiunta di un nuovo reticolo con frequenza diversa consente la creazione di reticoli doppi periodici, quasi-periodici o random. Da un punto di vista teorico, quando il reticolo principale è sufficientemente intenso rispetto all'energia termica, il sistema può essere descritto mediante l'approssimazione

del legame stretto (tight binding, TB). Essa consiste nel troncare la base Bloch di singola particella alla prima banda, ed espandendere gli operatori di campo nella base di Wannier, che è un insieme di funzioni d'onda di singola particella esponenzialmente localizzate.

Molte parti di questa tesi sono focalizzate su sistemi unidimensionali con una geometria quasi-periodica, realizzando quello che è noto come *modello di Aubry-André* (AAM) [35–44]. Questo è un modello con approssimazione TB che contiene *hopping* a primi vicini ed energie di sito ottenute da una combinazione di due funzioni periodiche con frequenze incommensurate. Il modello AAM mostra una transizione di fase da metallo ad isolante [35, 36].

L'interazione tra geometria e interazione in sistemi a molti corpi può generare una gamma impressionante di fenomeni fisici. Ad esempio, lo stato fondamentale di un gas di bosoni interagenti, soggetti ad un potenziale quasiperiodico, mostra un ricco diagramma di fase [45–47], che attraversa fasi di superfluido, Bose-glass e isolante di Mott, a seconda del filling, delle interazioni e della forza del potenziale esterno. È interessante notare che una soglia di mobilità (ME) appare quando un'estensione dell'AAM viene presa in considerazione, includendo nell'hamiltoniana dei termini di hopping più a lungo raggio, come i termini a secondi vicini [48,49], o "infiniti vicini" [50–52]. La transizione da fase estesa a localizzata dell'AAM, nell'ambito della fisica di molti corpi, è stata ampiamente investigata sia da un punto di vista teorico [53–56] che sperimentale [53, 57–63].

Il primo capitolo di questa tesi si occupa principalmente del gas di TG, mostrando come la geometria e l'interazione competano per determinare le proprietà statiche e dinamiche del sistema, come la distribuzione dei momenti e la funzione spettrale.

A questo scopo, esso esamina le proprietà dello stato fondamentale del sistema di bosoni fortemente interagenti e dei fermioni non interagenti, immersi in un reticolo bicromatico. Dopo aver descritto in sez. 1.1 il *mapping* del gas bosonico in fermioni non interagenti, motivando così la scelta di guardare entrambe le specie, in sez. 1.2.1 è introdotto l'AAM e sono richiamate le sue proprietà di singola particella. Quindi, in sez. 1.2.2 e sez. 1.2.3 sono descritti l'effetto della transizione da metallo ad isolante e l'influenza della presenza della soglia di mobilità sullo stato fondamentale del sistema a molti corpi, fermionico e TG.

La sez. 1.3 è focalizzata sulla funzione spettrale (SF) del gas di Tonks-Girardeau, che è una quantità primaria nella fisica many-body: contiene informazioni sulla probabilità di eccitare una particella o una lacuna a seguito di una perturbazione esterna. Inoltre, la SF può essere misurata negli esperimenti con gas ultrafreddi mediante spettroscopia di fotoemissione risolta in angolo (ARPES) o spettroscopia Raman stimolata. [64–67]. Tramite la teoria di Luttinger lineare e non lineare [68–74] è possibile studiarne solo alcune proprietà, come il supporto, le non analiticità e il comportamento

asintotico. Al contrario, gli approcci numerici sono spesso troppo esigenti dal punto di vista computazionale. La prima parte della sez. 1.3 mira a sviluppare un algoritmo efficiente per calcolare le funzioni di Green del gas di TG, e quindi la SF, in qualsiasi potenziale spaziale, scrivendole come funzionali in termini delle funzioni d'onda di singola particella. Nella seconda parte, tale metodo viene applicato a un gas di TG in un reticolo (periodico). Si mostra come la presenza del reticolo dia luogo ad alcune nuove non analiticità, che non hanno analoghi nel corrispondente sistema omogeneo.

La seconda parte di questa tesi (cap. 2 e 3) si interessa delle proprietà dinamiche di gas di Fermi interagente e non, in reticoli periodici o quasi-periodici, al fine di rispondere alla stessa domanda della prima parte: cioè di come la competizione tra geometria e interazione si rifletta sulle dinamiche del sistema a molti corpi. Per studiare le proprietà dinamiche di tali sistemi, si fa spesso ricorso al concetto di *quantum quench*. È un protocollo che prevede che un sistema quantistico, inizialmente preparato in uno stato di equilibrio, venga posto fuori da esso da una perturbazione esterna. In questo modo, alcune proprietà del sistema possono essere studiate osservando le dinamiche generate dall'evoluzione quantistica.

Il rilassamento di un sistema quantistico verso l'equilibrio, in seguito ad una perturbazione globale o locale, è stato ampiamente studiato nel recente passato. Tale argomento ha beneficiato dei progressi e delle recenti realizzazioni di sistemi fuori dall'equilibrio negli esperimenti con gas ultrafreddi. Uno dei punti chiave verso la comprensione dinamiche globali è la connessione tra le proprietà a singola particella e quelle a molti corpi. Un esempio rappresentativo è dato dalle *fasi many-body localizzate* riportate di recente in [75], dove il concetto di localizzazione spesso diventa ambiguo e richiede che siano adottati criteri differenti per una definizione significativa.

Il cap. 2 indaga la dinamica post-quench di un gas di Fermi non interagente, intrappolato da un potenziale ottico periodico in una dimensione. Le recenti realizzazioni di sistemi analoghi a quelli usuali della materia condensata hanno ispirato l'esame dello scenario in cui un'impurezza a due livelli è immersa nel gas, con l'ulteriore condizione che l'interazione tra essa ed il gas si verifichi solo quando la prima si trovi nel suo stato eccitato. Questo set-up, oltre a fornire un modo per introdurre una perturbazione localizzata nello spazio, consente anche la ricostruzione delle dinamiche many-body del gas, tramite l'interferometria Ramsey [76–79].

Lo spettro di singola particella è costituito da bande di energia di larghezza diversa, con gap diverse tra loro, generati dal potenziale di reticolo periodico. Le larghezze di banda e le gap sono naturalmente funzione dell'ampiezza del potenziale del reticolo. In particolare, quando questa ampiezza è sufficientemente maggiore di una certa soglia di riferimento, cioè la codidetta *recoil energy*, lo spazio che separa la prima e la seconda banda è così ampio che

il sistema può essere descritto, nel limite termodinamico, mediante gli stati della prima banda solamente. Questa condizione, stabilendo il cosiddetto regime di tight binding (TB), è stata ampiamente documentata in letteratura [2, 80, 81]. Molto meno è noto in tutti gli altri casi, quando una o più bande superiori vengono coinvolte nell'evoluzione e la dinamica del sistema può essere trattata solo con una descrizione continua (CNT).

Quindi, la sez. 2.1 pone l'attenzione su un gas intrappolato da un potenziale di tipo senquadro, e fa affidamento sull'equazione di Schrödinger di una particella singola per passare da regimi TB a non TB (CNT), impostando opportunamente la forza del potenziale di reticolo. Le sez. 2.2 - 2.4 esplorano la fisica del non equilibrio oltre l'approssimazione discreta. Inoltre, lavorando con una rappresentazione continua, si caratterizzano le transizioni interbanda indotte dal quench, approfondendo la loro dipendenza dalla prima gap di banda, dal potenziale chimico e dall'intensità sia del potenziale di reticolo che dell'interazione con l'impurezza.

Dal punto di vista metodologico, la sez. 2.2 impiega due differenti strategie: il formalmente esatto *functional determinant approach* (FD) (sez. 2.2.2), contenuto all'interno del formalismo Levitov [82, 83], e un approccio perturbativo (sez. 2.2.3), che va sotto il nome di *linked cluster expansion* (LCE).

Come primo risultato (sez. 2.3) si mostra che, nel limite di temperatura zero, il decadimento dell'eco nel tempo segue una legge a potenza (sez. 2.3.1) quando la banda ad energia più bassa è parzialmente occupata. Questa costituisce la firma della catastrofe di ortogonalità di Anderson (AOC) [84–86], che dà origine ad una *Fermi edge singularity* [87, 88] nel dominio delle frequenze. Le caratteristiche essenziali del meccanismo della AOC sono catturate dal secondo ordine della LCE. Questo ci permette inoltre di trovare un'espressione analitica per l'esponente caratteristico del decadimento. In secondo luogo, si esplorano gli effetti di taglia finita, che entrano in gioco entrando per tempi superiori al decadimento della AOC (sez. 2.3.2). Anch'essi sono descritti adeguatamente dalla LCE già al secondo ordine.

Infine, in sez. 2.4.2, si riporta la soppressione della AOC quando il sistema si avvicina alla configurazione di isolante, cioè quando le particelle del gas tendono ad occupare completamente i livelli della prima banda. In questo affascinante caso, il gas risponde alla perturbazione con dei peculiari *modi di Fano*, che sono chiaramente visibili nello spettro di assorbimento del sistema, calcolato con l'approccio FD. Se ne fornisce un'interpretazione usando il contributo dominante del terzo ordine della LCE.

Il cap. 3 riporta come l'evoluzione temporale di un sistema fermionico in un quasicristallo, in presenza di interazione, sia correlata allo spettro di una singola particella efficace. La scoperta dei quasicristalli nel 1982 [89] e dei protocolli per produrre campioni ampi e stabili [90] ha innescato diversi studi teorici volti a comprendere l'origine delle loro proprietà fisiche insolite.

Le loro peculiari caratteristiche di trasporto, come l'aumento della resistività al decrescere della temperatura e al crescere della purezza del campione [91], hanno attirato grande attenzione [92]. Ben presto ci si rese conto che questo comportamento fosse strettamente legato alla natura *singular continuous* (SC) dello spettro di energia di singola particella (SPES), accompagnato da autofunzioni critiche le cui proprietà di *scaling* possono spiegare l'anomalia del trasporto e della diffusione [92]. Prima della scoperta dei materiali quasi-cristallini, si pensava che l'idea dello spettro SC fosse una pura elucubrazione matematica, senza controparte fisica [93]. Infatti la componente SC non è facilmente accessibile e, spesso, la sua presenza è dedotta solamente dopo aver escluso l'esistenza delle componenti assolutamente continue (AC) e discrete (*pure point*, PP) dall'intero spettro.

Il ruolo degli spettri SC nelle dinamiche dei sistemi non interagenti è stato studiato in [94], ed il suo collegamento alla propagazione anomala delle correlazioni e della diffusione di un pacchetto di onde inizialmente localizzato è stato studiato in [95, 96]. Un modello fisico particolarmente interessante, in cui la natura dello spettro gioca un ruolo cruciale, è il AAM, citato in precedenza. È stato dimostrato che il suo spettro è AC e PP rispettivamente nelle fasi di metallo e di isolante, mentre è puramente SC nel punto di transizione [37, 97]. Tale modello è stato realizzato con atomi ultrafreddi immersi in un reticolo ottico bicromatico [62, 63, 98]. A causa della presenza di interazioni, esso possiede un diagramma di fase non banale [45–47], con la presenza di una soglia di mobilità [20, 99] e di fase *many-body-localized* che separa quella ergodica da quella localizzata [63, 98].

I recenti esperimenti [63,98], che riportano l'osservazione del rallentamento della dinamica di un gas interagente immerso in un reticolo bicromatico incommensurato, hanno suggerito di provare a fornire una spiegazione di queste osservazioni basata sulla natura dello spettro di energia a singola particella dell'AAM. Sono stati trovati diversi comportamenti: uno ergodico, a piccoli λ_s con AC SPES, ed uno localizzato, a grandi λ_s e moderatamente piccoli U con PP SPES. Questi due comportamenti estremi sono separati da una regione intermedia, caratterizzata da uno SC SPES, in cui la dinamica è ergodica, ma su scale temporali molto più grandi di quelle tipiche di singola particella. Le nostre osservazioni implicano che una concorrenza non banale tra l'ordine indotto dal potenziale e le interazioni *many-body* sono responsabili di questo comportamento.

I risultati di questa tesi sono stati presentati in quattro documenti, il primo dei quali è già stato pubblicato, il secondo è attualmente sottomesso ed in stato di revisione, mentre gli altri due sono in preparazione:

- J. Settino, N. Lo Gullo, A. Sindona, J. Goold and F. Plastina "Signatures of the single-particle mobility edge in the ground-state properties of Tonks-Girardeau and noninteracting Fermi gases in a

bichromatic potential."
Physical Review A 95, 1–9, 2017

- J. Settino, N. W. Talarico, F. Cosco, F. Plastina, S. Maniscalco, and N. Lo Gullo
"Disentangling the role of geometry and interaction in many-body system dynamics: the emergence of anomalous dynamics from the underlying singular continuous spectrum."
ArXiv:1809.10524, 2018 (submitted to *Physical Review Letter*)

- W.Talarico, J. Settino, F. Plastina, A. Sindona, S. Maniscalco, and N. Lo Gullo
"Sudden quench and long time dynamics in an ultracold fermionic gas" (in preparation).

- J. Settino. N. Lo Gullo, P. Vignolo, F. Plastina, A. Minguzzi
"Spectral function of the Tonks-Girardeau gas in a optical lattice" (in preparation)

Abstract - Introduction

Physics of interacting many-body systems is a very active research field, due to astonishing advances in realizing, controlling and measuring such systems, and to fundamental problems being still open, such as the behavior of systems with broken integrability.

Ultra-cold quantum gases, now prepared in a variety of configurations in laboratories worldwide, have emerged as ideal candidates for clean and controllable simulation of condensed matter physics [1, 2]. In particular, both bosonic and fermionic atoms can be loaded and manipulated in optical lattice potentials [3]. The lack of thermal phonons, togheter with the tunability of the interactions by mean of Feschbach resonances [4], has allowed for the detailed study of a multitude of phase diagrams of critical many-body systems, both at equilibrium, and away from it [5, 6].

Among all the systems realized in the framework of ultra-cold gas, special mention deserves the Tonks-Giradeau (TG) gas [7–12], a system of hardcore (impenatrable) bosons introduced by Giraedeau in Ref. [13], that corresponds to the infinite interaction limit of the Lieb-Liniger model [14, 15]. Thanks to the possibility of mapping the TG system into one of non-interacting fermions, several facets have been deeply investigated: momentum distribution [16–20], density matrix [17,19–28] and also some non-equilibrium dynamical properties [29–34].

Besides the ability to engineer and tune interactions, a particularly appealing feature of cold atoms is the possibility to manipulate the shape of the external potential, especially for the simulation of condensed matter physics. Practically, any lattice geometry may be achieved with optical potentials, by engineering the direction, wavelength, intensity, polarization, and phase of the laser beam. Also the dimensionality of the system can be modified. For instance, starting from a 3D system, an array of 1D (2D) systems can be generated by a 2D (1D) counterpropagating laser beams. The dynamics on the unwanted directions is frozen by using a sufficiently strong confining potential. Moreover, adding a new lattice of different frequency on top of the existing one allows to create a superlattice. It permits the creation of double well or quasi-periodic and random lattices. From an theoretical point of view, when the lattice is deep enough regarding to the thermal energy, the tight binding approximation can be performed. It consist of

describing the hamiltonian by truncating the single-particle Bloch basis to the first band, and expanding the field operators in the Wannier basis, a set of exponentially localized single-particle wavefunctions.

Many parts of this thesis are focused on 1D many-body systems in a *quasi-periodic geometry*, implemented via an external potential that realizes what is known as André-Aubry (AA) model [35–44]. This is a one dimensional tight binding model on a lattice, with nearest-neighbor hopping terms and on-site energies given by a combination of two periodic functions having non-commensurate wave numbers, which has been shown to display a metal-to-insulator transition [35, 36].

The interplay between geometry and interaction in many-body systems can generate an impressive range of physical phenomena. For example, the ground state properties of interacting bosons, subject to a quasi-periodic potential, show a rich phase diagram at zero temperature [45–47], displaying superfluid, Bose-glass and Mott insulator phases depending upon the filling of the lattice, the interactions and the strength of the potential. Interestingly, a mobility edge (ME) appears when an extension of the AA model is considered, allowing for longer-range hopping such as next-nearest-neighbor terms [48, 49] or a continuous model (infinite-range hopping) [50, 51], or even interactions [52]. The extended-to-localized phase transition of the AA model, within the framework of many body physics, has been widely investigated both from a theoretical point of view [53–56] and from an experimental one [53, 57–63].

The first chapter of this thesis mainly deals with the TG gas, showing how geometry and interaction compete to determine static and dynamical properties of the system, like the momentum distribution or the spectral function. To this aim, it examines the ground state properties of both non-interacting fermions and of strongly-interacting bosons in a bichromatic lattice. After having described the fermion-based representation of the strongly interacting bosonic gas in sec. 1.1, thus motivating the choice of looking at both species, sec. 1.2.1 introduces the considered model and recall its single particle properties, which are crucial to understand the results in the many-body case. Then, sec. 1.2.2 and sec. 1.2.3 describe the effect of the delocalization-to-localization transition and the influence of the mobility edge on the many-body ground state for a system of non-interacting, spinless fermions and a Tonks-Girardeau gas.

Sec. 1.3 is focused on the spectral function of the Tonks-Girardeau gas, that is a primary quantity in many-body physics: it embodies information on the probability of exciting a particle or a hole in the system by an external perturbation. Moreover it can be measured in ultracold gas experiments by angle-resolved photoemission spectroscopy (ARPES) or momentum-resolved stimulated Raman spectroscopy. [64–67]. It has been theoretically investigated by linear and non-linear Luttinger theory [68–74] for different systems,

but analytical calculations allow to explore only some of its properties such as support, nonanalyticities and asymptotic behaviour. Numerical approaches are often computationally demanding because of the complexity of many-body physics. The first part of sec. 1.3 aim at developing an efficient algorithm for evaluating the Green's functions of the TG gas, and therefore the SF, in any spatial potential, by writing them as a functional of single particle states. In the second part, it is applied to a TG gas in a lattice, and show how the presence of the lattice gives rise to some new non-analyticities that have no analogues in the homogeneous system.

The second part of this thesis (chap. 2 and 3) deals with dynamical properties of interacting and non-interacting fermions, again in periodic or quasi-periodic lattices, in order to answer to the same question of the first part: how the competition between geometry and interaction is reflected onto the many-body dynamics. In order to study the dynamical properties of these systems, the concept of *quantum quench*is resorted. It is a protocol according to which a quantum system, prepared in some initial equilibrium state, is brought out-of-equilibrium by an external perturbation. In this way, some properties of the system can be studied by looking at the dynamics generated by the quantum quench.

The relaxation of a quantum system towards equilibrium, following a global or local perturbation, has been extensively and widely studied over the recent past. This topic has certainly benefited from advances and recent realizations of out-of equilibrium systems in ultracold gas experiments, besides being interesting in its own from the theoretical point of view. One of the key points, towards the understanding of the global dynamics of these systems, is the connection between single-particle and many-body properties. A representative example is given by the recently reported many-body localized phases [75], where the concept of localization often gets blurry and requires different criteria to be adopted for a meaningful definition.

Chap. 2 investigates the post-quench dynamics of a non-interacting Fermi gas, trapped by a periodic optical potential in one dimension, and provide a clear link between the global evolution of the system and the energy spectrum of each single constituent of the gas, using the Loschmidt echo as a figure of merit. Recent realizations of condensed matter analogues have inspired to examine the scenario of a two-level impurity immersed in the gas, with the further condition that the gas-impurity interaction occurs only when the atom lies in its excited state. This set-up, besides providing a way of introducing a localized perturbation in space, allows also for the reconstruction of the many-body dynamics of the gas, via Ramsey interferometry [76–79].

The single particle spectrum is made up of energy bands of different widths, with different gaps between them, opened by the periodic lattice potential. The bandwidths and interband gaps are naturally function of the

lattice potential amplitude. In particular, when this amplitude is sufficiently larger than a certain reference energy, i.e., the recoil energy, the gap separating the first and second bands is so wide that the system can be described, in the thermodynamic limit, by means of the states of the first band only. This condition, establishing what is known as tight binding (TB) regime, has been widely documented in the literature, for gases of both fermions and bosons [2, 80, 81]. Much less is known in all other cases, when one or more bands higher than the lowest one get involved in the quench and the system dynamics can be treated only with a continuum (CNT) description.

Then, Sec. 2.1 sets the focus on a trapped gas in a sin-squared potential, and relies on the single-particle Schrödinger equation to switch between the TB and non-TB (CNT) regimes by tuning the strength of the lattice potential. Secs. 2.2 - 2.4 explore the non-equilibrium physics beyond the discrete approximation that is well suited only in the TB limit. Furthermore, working with a continuous representation, we characterize the quench-induced interband transitions, elucidating their dependence on the first band gap, the chemical potential and the strengths of both the lattice potential and the sudden (impurity) potential.

From the methodological point of view, sec. 2.2 emploies two comparative strategies based on a (formally exact) functional determinant (FD) approach (Sec. 2.2.2), within the Levitov formalism [82, 83], and a perturbation approach (Sec. 2.2.3), within the linked cluster expansion (LCE).

As a first result (Sec. 2.3), it is shown that the decay of the echo follows a power-law in time (Sec. 2.3.1), when lowest lying band is partly occupied in the zero temperature limit. This is a signature of the Anderson orthogonality catastrophe (AOC) [84–86], giving rise to a Fermi-edge singular spectrum [87, 88] in the frequency domain. The essential features of the AOC mechanism are captured by the second order of the LCE. This allows us to find an expression for the critical exponent of the decay. Secondly, the role of finite-size effects is explored, coming into play beyond the AOC decay (Sec. 2.3.2), which is found to be adequately described by the LCE already at the second order.

Finally (Secs.2.4.2), it is reported the suppression of the AOC mechanism, with the system approaching the band insulator configuration, i.e., with the particles in the gas tending to completely fill the first band levels at the absolute zero. In this fascinating case, the gas responds with peculiar Fano modes, which are clearly visible in the absorption spectrum of the system computed with the FD approach. They are interpreted using the dominant contribution to the third-order correction of the LCE, accounting for particle-hole or hole-particle excitations, dynamically screened by particle-hole recombinations.

Chap. 3 reports how the dynamical evolution is related to the effective single particle spectrum of a fermionic system in a quasicrystal in presence of

interaction. The discovery of quasicrystals in 1982 [89] and of protocols to produce large and stable samples [90] has triggered the theoretical studies aiming at understanding the origin of their unusual physical properties. Among others, their peculiar transport features, such as the increasing of the resistivity with both decreasing temperature and increasing the sample purity [91], have attracted great attention [92]. It was soon realized that this behavior is strictly linked to the singular continuous (SC) nature of the single-particle energy spectrum (SPES), with the accompanying critical eigenfunctions[1], whose scaling properties can account for anomalous transport and diffusion, and can partially explain the unusual behavior of these materials [92]. Before the discovery of quasicristalline materials, the mathematical concept of SC spectrum[2] was thought to be a purely mathematical lucubration with no physical counterpart [93]. The SC part is not easily accessible, and, often, its presence is inferred after removing the absolutely continuous (AC) and pure-point (PP) parts from the whole spectrum, provided a set of non-zero measure is left over.

The role of SC spectra in the dynamics of non-interacting systems has been investigated in Ref. [94] and its link to anomalous propagation of correlations and in the spreading of an initially localized wave-packet has been investigated in Refs. [95, 96]. A particularly interesting exemplary physical model where the nature of the spectrum plays a crucial role is the AAM, previously cited. It has been proven that its spectrum is AC and PP in the metal and insulating phases, respectively, whereas it is purely SC at the transition point [37, 97]. The model has been realized with ultra-cold atoms loaded in a bichromatic optical lattice [62, 63, 98]. Due to the presence of interactions, such system displays a non-trivial phase diagram [45–47], with the appearance of a mobility edge [20, 99] and of a many-body-localized phase separating an ergodic from a localized one [63, 98].

Recent experiments [63, 98] reporting the observation of the dynamical slowing down of an interacting gas loaded in an incommensurate bichromatic lattice have motivated to provide an explanation for these observations based on the nature of the single-particle energy spectrum of the AAM model. Different behaviors have been found : an ergodic one at small λs with an AC SPES, and a localized one at large λs and moderately small U with a PP SPES. These two extreme behaviors are separated by an intermediate region, characterized by a SC SPES, where the dynamics is still ergodic but on time scales much larger than the typical single-particle time scales. Our findings imply that a non-trivial competition between the underlying order

[1] An eigenfunction is said to be critical if it is not delocalized nor exponentially localized; althought there exist different types of such eigenfunctions most of them are characterized by a power law envelope and/or non-trivial (multi-)fractal properties.

[2] According to the Lesbegue decomposition theorem a positive measure can be split into three (mutually orthogonal) components: absolutely continuous (AC), singular continuous (SC) and pure point (PP) according to the nature of their support.

induced by the potential energy landscape and the many-body interactions is responsible for this behavior.

The results of this thesis have been presented in four papers, the first has been already published, the second is submitted and under review for publication, and other two are in preparation:

- J. Settino, N. Lo Gullo, A. Sindona, J. Goold and F. Plastina
  "Signatures of the single-particle mobility edge in the ground-state properties of Tonks-Girardeau and noninteracting Fermi gases in a bichromatic potential."
  Physical Review A 95, 1–9, 2017

- J. Settino, N. W. Talarico, F. Cosco, F. Plastina, S. Maniscalco, and N. Lo Gullo
  "Disentangling the role of geometry and interaction in many-body system dynamics: the emergence of anomalous dynamics from the underlying singular continuous spectrum."
  ArXiv:1809.10524, 2018 (submitted to *Physical Review Letter*)

- W.Talarico, J. Settino, F. Plastina, A. Sindona, S. Maniscalco, and N. Lo Gullo
  "Sudden quench and long time dynamics in an ultracold fermionic gas"
  (in preparation).

- J. Settino. N. Lo Gullo, P. Vignolo, F. Plastina, A. Minguzzi
  "Spectral function of the Tonks-Girardeau gas in a optical lattice"
  (in preparation)

1

Tonks-Girardeau gas in periodic and quasi-periodic potentials

Per il segno che c'è rimasto
non ripeterci quanto ti spiace
non ci chiedere più come è andata
tanto lo sai che è una storia sbagliata
tanto tu lo sai che è una storia sbagliata.

– Fabrizio De André, *Una storia sbagliata*

In this chapter we explore the ground state static and dynamical properties of cold atomic bosonic gases that can be well approximated by using a hard-core model for the two-body interaction (Tonks-Girardeau gas). The key idea is that a hard-core interaction for bosons mimics the Pauli exclusion principle and allows a simplified treatment of the system via the well know mapping [13]. After having reviewed the recognized methods for the static properties and developed original ones for the dynamics in sec. 1.1, we study two different situations on which these methods have been applied.

In sec. 1.2 we focus on cold gases trapped by the combination of two potentials (bichromatic lattice) with incommensurate periods. For such systems, two limiting cases have been thoroughly established. In the tight-binding limit, the single-particle states in the lowest occupied band show a localization transition, as the strength of the second potential is increased above a certain threshold. In the continuous limit, when the tight-binding approximation does not hold, a mobility edge is found, instead, whose position in energy depends upon the strength of the second potential. We study

how the crossover from the discrete to the continuum behavior occurs, and prove that signatures of the localization transition and mobility edge clearly appear in the generic many-body properties of the systems. Specifically, we evaluate the momentum distribution, which is a routinely measured quantity in experiments with cold atoms, and demonstrate that, both for non-interactiong fermions and TG bosons the single particle mobility edge can be observed in the ground state properties.

In sec. 1.3 we apply our main results to calculate the spectral function (SF), that is a measurable quantity in ultracold gases via ARPES technique, of a TG gas in a periodic confinement. We compare the results with existing literature regarding the homogeneous system and show how the presence of the lattice modifies non-analyticities and singularities of the SF.

1.1 The Tonks-Girardeau gas

Optical lattices allow to create trapping potentials that are tight enough in the transversal direction to freeze out all dynamics in these degrees of freedom [100]. A gas of N bosons in such a potential can then be approximately described by the one-dimensional Hamiltonian

$$\mathcal{H}_0 = \sum_{n=1}^{N} \left[-\frac{\hbar^2}{2m} \frac{\partial^2}{\partial x_n^2} + V(x_n) \right] + g \sum_{i<j} \delta(|x_i - x_j|) \tag{1.1}$$

where m is the mass of the particles contained in the kinetic energy term, V is the external potential [1] and g_{1D} is a 1D coupling constant which is derived from the renormalisation of the three-dimensional scattering process, $g = \frac{4\hbar^2 a_{3D}}{m w_\perp} \left(w_\perp - C a_{3D}\right)^{-1}$ [101]. Here $w_\perp$ is the trap width in the transversal direction (harmonic trapping), $C = -\zeta(1/2) \simeq 1.46035$ is a constant, and a_{3D} is the scattering length in three-dimensions. This Hamiltonian describes an inhomogeneous Lieb-Liniger gas, which in the strongly repulsive limit, $g \to \infty$, can be solved by using a mapping to an ideal and spinless fermionic system [13, 25]. The essential idea of this mapping is that one can treat the interaction term in Eq. (1.1) by replacing it with a boundary condition on the allowed bosonic wave-function

$$\Psi_B(x_1, x_2, \ldots, x_n) = 0 \quad \text{if} \quad |x_i - x_j| = 0 \,, \tag{1.2}$$

for $i \neq j$ and $1 \leq i \leq\ j \leq N$. This is the hard-core constraint, which says that probability for two particles to be at the same point in space is zero.

Such a constraint is automatically fulfilled by calculating the wave-function using a Slater determinant

$$\Psi_F(x_1, x_2, \ldots, x_N) = \frac{1}{\sqrt{N!}} \det_{(n,j)=(0,1)}^{(N-1,N)} \psi_n(x_j) \,, \tag{1.3}$$

[1] In the case of ultracold atoms, V comprises the trapping potential and eventually other periodic, quasiperiodic or disordered potentials.

where the ψ_n are the single particle eigenstates of the ideal system. This, however, leads to a fermionic rather than bosonic symmetry, which can be corrected by a multiplication with the appropriate unit antisymmetric function [13]

$$S = \prod_{1 \leq i < j \leq N} \mathrm{sgn}(x_i - x_j) \,, \tag{1.4}$$

to give [2]

$$\Psi_B(x_1, x_2, \ldots, x_N) = S(x_1, x_2, \ldots, x_N)\Psi_F(x_1, x_2, \ldots, x_N). \tag{1.5}$$

One consequence of this mapping is that all local quantities, e.g. the spatial density of particles, are exactly the same as those of a non-interacting fermionic gas. The difference between these two systems emerges in the non-local quantities such as momentum distribution or structure factor; signatures of the bosonic nature of the TG are still clearly visible, e.g. in the peak at zero momentum of the momentum distribution, whereas the features related to the unitary limit are encoded in their asymptotic behavior (tails, non-analiticities).

1.1.1 Reduced single particle density matrix and momentum distribution

The reduced single particle density matrix (RSPDM) allows the calculation of the properties of all single particle observables. Although eq. 1.5 enable to write the exact many-body wavefunction describbing the TG gas in compact form, the evaluation of the RSPDM is a difficult task [30, 102–112]. For a generic eigenstate of the many-body hamiltonian Pezer and Buljan in ref. [18] developed an efficient closed formula of the RSPDM of a generic many-body state $|\eta\rangle$as a function of single particle eigenfunctions. The RSPDM is defined as:

$$\begin{aligned} \rho_\eta(x, y) = \left\langle \hat{\psi}^\dagger(x)\hat{\psi}(y) \right\rangle_\eta &= \langle \eta | \hat{\psi}^\dagger(x) \frac{1}{N-1!} \int dX \, |X\rangle\langle X| \, \hat{\psi}(y) | \eta \rangle \\ &= \frac{1}{N-1!} \int dX \Psi^*_\eta(x, X) \Psi^(_\eta y, X) \end{aligned} \tag{1.6}$$

where we have used used the completeness relation in the $N-1$ particles Hilbert space in the position representation $1/(N-1)! \int dX \, |X\rangle\langle X| = \mathbb{I}$, with $X = x_2 ... x_N$, the action of the field operator to an eigenstate of a many body position operator $\hat{\psi}^\dagger(x) \, |X\rangle = |x, X\rangle$ and the definition of wavefunction

[2] Because of the sign function, one can easily verify that, in order to have a bosonic wavefunction with periodic boundary conditions, the fermionic one has to be periodic for odd N and anti-periodic for even N. In this thesis we will always work with open boundary conditions, which are fulfilled if the single particle wavefunctions satisfy open boundary conditions. [34]

$\langle X|\eta\rangle = \Psi_\eta(X)$ for a generic eigenstate $|\eta\rangle$ of the many-body hamiltonian. Each of the wave functions above can be written by using the mapping into non-interacting fermions of eq. 1.5 and simplifying the squares of sign functions:

$$\begin{aligned}\rho_\eta(x,y) &= \frac{1}{N-1!}\int dX \prod_{k=2}^{N} sign(x-x_k) \prod_{2\le i<j\le N}^{N} sign(x_i-x_j)\Psi_\eta^{F*}(x,X) \\ &\qquad \times \prod_{k=2}^{N} sign(y-x_k) \prod_{2\le i<j\le N}^{N} sign(x_i-x_j)\Psi_\eta^{F}(y,X) \\ &= \frac{1}{N-1!}\int dX \prod_{k=2}^{N} sign(x-x_k)\Psi_\eta^{F*}(x,X) \prod_{k=2}^{N} sign(y-x_k)\Psi_\eta^{F}(y,X).\end{aligned} \tag{1.7}$$

The fermionic wavefunctions coincide with the Slater determinant of single particle wavefunctions of occupied states. Labeling with $\vec{\eta} = \eta_1, \dots, \eta_N$ the collection of occupied states indexes, we use the Laplace expansion of the determinant to take out SP eigenfuctions that are not integrated and then apply the Andréief's integration formula [3] to combine the minors left:

$$\begin{aligned}\rho_\eta(x,y) &= \frac{1}{N-1!}\int dX \sum_{i,j\in\vec{\eta}} (-1)^{i+j}\phi_i(x)\phi_j^*(y) \\ &\qquad \times \prod_{k=2}^{N} sign(x-x_k)\det[\phi_l(x_m)]_{\substack{l\in\vec{\eta}\setminus\{i\}\\ m=2,N}} \prod_{k=2}^{N} sign(y-x_k)\det[\phi_l^*(x_m)]_{\substack{l\in\vec{\eta}\setminus\{j\}\\ m=2,N}} \\ &= \frac{1}{N-1!}\int dX \sum_{i,j\in\vec{\eta}} (-1)^{i+j}\phi_i(x)\phi_j^*(y) \\ &\qquad \times \det[sign(x-x_m)\phi_l(x_m)]_{\substack{l\in\vec{\eta}\setminus\{i\}\\ m=2,N}} \det[sign(y-x_m)\phi_l^*(x_m)]_{\substack{l\in\vec{\eta}\setminus\{j\}\\ m=2,N}} \\ &= \sum_{i,j\in\vec{\eta}} (-1)^{i+j}\phi_i(x)\phi_j^*(y)\det\left[\int \mathrm{d}\bar{x}\, sign(x-\bar{x})sign(y-\bar{x})\phi_l(\bar{x})\phi_m^*(\bar{x})\right]_{\substack{l\in\vec{\eta}\setminus\{i\}\\ m\in\vec{\eta}\setminus\{j\}}} \\ &= \sum_{i,j\in\vec{\eta}} \phi_i(x)\phi_j^*(y)A_{i,j}(x,y)\end{aligned} \tag{1.9}$$

with

$$A_{i,j}(x,y) = (-1)^{i+j}\det[\mathbf{P}]_{\vec{\eta}\setminus\{i\},\vec{\eta}\setminus\{j\}} = [\mathbf{P}^{-1}]_{j,i}\det[\mathbf{P}] \tag{1.10}$$

[3] [23] $$\int \mathrm{d}x_1 \cdots \int \mathrm{d}x_M \det[f_j(x_k]_{j,k=1,M}\det[g_j(x_k]_{j,k=1,M} = M!\det\left[\int \mathrm{d}x f_j(x)g_k(x)\right]_{j,k=1,M} \tag{1.8}$$

and

$$\begin{aligned} P_{l,m} &= \int \mathrm{d}\bar{x}\, \phi_l(\bar{x})\phi_m^*(\bar{x}) sign(x-\bar{x}) sign(y-\bar{x}) \\ &= \delta_{l,m} - 2\int_{\min(x,y)}^{\max(x,y)} \phi_l(\bar{x})\phi_m^*(\bar{x}) \end{aligned} \tag{1.11}$$

The eigenfunctions ($\varphi_i(x)$) and eigenvalues (λ_i) of the RSPDM, defined by $\int dx\rho(x,y)\varphi_i(x) = \lambda_i\varphi_i(y)$ and normalized such that $\sum_i \lambda_i = 1$, are the so called *natural orbitals* and their *populations*, respectively.

Moreover the diagonal part of the (double) Fourier transform of the RSPDM gives the momentum distribution (MD),

$$n(k) = \frac{1}{2\pi}\int dxdy \exp^{ik(x-y)} \rho(x,y), \tag{1.12}$$

which is directly measurable in cold atom experiments by time-of-flight measurements. The MD is conveniently expressed in terms of the natural orbitals and their corresponding eigenvalues,

$$n(k) = \sum_{j=1}^{N} \lambda_j |\tilde{\varphi}_j(k)|^2. \tag{1.13}$$

Here, $\tilde{\varphi}_j(k)$ is the Fourier transform of the j-th natural orbital.

For a non-interacting Fermi gas, as one could have expected, there are only N non-vanishing eigenvalues, which are all equal to $1/N$, and the corresponding eigenvectors coincide with the N occupied single particle energy states, or, because populations are degenerate, with a linear combinations of them. So, the RSPDM and MD of a non-interacting fermion gas in a many-body eigenstate of the hamiltonian can be expressed via the single particle eigenstates:

$$\rho_F(x,y) = \sum_{j\in\vec{\eta}} \phi_j^*(x)\phi_j(y) \tag{1.14}$$

and

$$n(k) = \sum_{j\in\vec{\eta}} \left|\tilde{\phi}_j(k)\right|^2 \tag{1.15}$$

where $\tilde{\phi}_j(k)$ is the Fourier transform of $\phi_j(x)$ [18].

In sec. 1.2 we will show that a similar analysis for a Tonks-Girardeau gas is much less trivial.

Finite temperature. The non-interacting fermionic RSPDM for finite temperature is

$$\rho_F(x_k, x_l) = \sum_{j=1}^{\infty} f_j \psi_j^*(x)\psi_j(y) \tag{1.16}$$

which is the analogous of eq 1.14 with each term weighted by the Fermi-Dirac occupation factors $f_j = [e^{(\varepsilon_j-\mu)/k_BT}+1]^{-1}$.

The finite temperature calculation of the RSPDM for the TG gas has been developed since 1966 by Lenard [21] but more efficient formulas came from Vignolo and Minguzzi in ref. [17] and Atas et al. in ref. [28]. In the grand-canonical ensemble the starting point is to write the thermal average of eq. 1.6:

$$\rho^T(x,y) = \sum_{N,\eta} P_{N,\eta}\rho_\eta(x,y) \tag{1.17}$$

where $P_{N,\eta} = e^{-\beta(E_{N,\eta}-\mu N)}/Z$ is the thermal distribution function, $Z = \sum_{N,\eta} e^{-\beta(E_{N,\eta}-\mu N)}$ is the partition function with $E_{N,\eta} = \sum_{j\in\vec{\eta}}\varepsilon_j$, $\beta = 1/k_BT$ and μ the chemical potential. It's possible to write the previous equation as a series of j-dimensional integrals [21]:

$$\rho^T(x,y) = \sum_{j=0}^{\infty}[sign(x-y)]^j \int_x^y \mathrm{d}x_2 \cdots \int_x^y \mathrm{d}x_{j+1}\, \det[\rho_F(x_k,x_l)]_{k,l=1}^{j+1} \tag{1.18}$$

written for $x \leq y$, where one has to take $x_{k=1} = x$ and $x_{l=1} = y$.

Each multidimensional integral is considerably simplified by recasting it to a combination of single-variable integrals [17]. The most efficient closed formula is obtained by Atas et al. in ref. [28] who recognized eq. 1.18 being a product between a Fredholm determinant and the associated resolvent operator, which lead to:

$$\rho^T(x,y) = \sum_{i,j=1}^{\infty} \sqrt{f_i}\phi_i(x) A^T_{i,j}(x,y)\sqrt{f_j}\phi^*_j(y). \tag{1.19}$$

The element $A^T_{i,j} = [\mathbf{P^T}^{-1}]_{j,i}\det[\mathbf{P^T}]$ are slightly different with respect to the zero temperature counterpart

$$P^T_{l,m}(x,y) = \delta_{l,m} - 2\sqrt{f_l f_m}\int_{\min(x,y)}^{\max(x,y)} \phi_l(\bar{x})\phi^*_m(\bar{x}). \tag{1.20}$$

The advantage of this formula is that it is recast into single particle wave-functions, which can be numerically calculated in any spatial potential.

1.1.2 Single particle Green's function

When it comes to quantities at different times, the situation is even more complicated. They are essential to investigate the response properties of the system or to study its dynamics. One extremely important quantity is the spectral function, which gives information on the accessible energies of the system and, therefore, to its transport properties (e.g. through the Landauer-Büttiker formula).

Another important quantity, strictly related to the spectral function, is the Fourier transform of the single-particle Green's function, which is the outcome of a typical ARPES experiment as the latter explores only initially occupied (particle) states and it is blind to the empty (hole) ones.

To compute these quantities, we resort to the non-equilibrium Green's function formalism [81], which naturally embodies the equilibrium one as a limit case. The NEGFs are the most natural framework to study the out-of-equilibrium dynamics of many-body quantum systems from a microscopic picture and, at the same time, allows to include many-body correlations. Due to the recent intense investigation of many-body quantum systems out-of-equilibrium, our results would be readily available to study quantum quenches or transport in a TG gas, as the NEGFs formalism allows for the inclusion of external reservoirs within the same formalism. In what follows, we will give an expression for the single-particle Green's functions:

- the lesser GF (particle propagator)

$$G^{<}(x,t;y,t') = \mp\imath \left\langle \hat{\Psi}^{\dagger}(y,t')\hat{\Psi}(x,t) \right\rangle ; \tag{1.21}$$

- the greater GF (hole propagator)

$$G^{>}(x,t;y,t') = -\imath \left\langle \hat{\Psi}(x,t)\hat{\Psi}^{\dagger}(y,t') \right\rangle ; \tag{1.22}$$

- the retarded Green function, that is nonzero for $t > t'$ only, and contains information about spectral properties, densities of states and scattering rates.

$$G^{R}(x,t;y,t') = \theta(t-t') \left[G^{>}(x,t;y,t') - G^{<}(x,t;y,t') \right] . \tag{1.23}$$

In the expression for the lesser Green's function, the minus and plus signs refer to bosonic and fermionic fields respectively. The knowledge of these functions will allow for the calculation of the spectral function

$$A(k,\omega) = -\frac{1}{\pi}\mathrm{Im}G^{R}(k,\omega) \tag{1.24}$$

with

$$G^{R}(k,\omega) = \int_{-\infty}^{\infty} \frac{dt}{2\pi} \int_{-\infty}^{\infty} \frac{dxdy}{(2\pi)^2} e^{\imath\omega t} e^{-\imath k(x-y)} G^{R}(x,t;y,0) \tag{1.25}$$

In the case of fermionic fields, the spectral function corresponds to the probability to excite a particle (hole) with energy ω ($-\omega$) and momentum k, as the spectral function can be normalized being always non-negative. In the bosonic case, the spectral function loses this nice property, as it can acquire negative values [81], and it is customary to look separately at the Fourier transforms of the lesser and greater Green's functions, which, instead, can be interpreted as the probability for a particle (hole) to be excited (filled).

In this section we discuss one of the main results of this thesis, namely the expression of the lesser and greater Green's functions gas in a efficient closed formula of the Tonks-Girardeau gas, outlining the procedure of them.

As in the previous section, let us assume that our system is made of N particles placed in N single-particle eigenstates labeled by the indexes $\vec{\eta} = \{\eta_1, \dots, \eta_N\}$; the many-body state of a TG gas is then given by the standard procedure of taking the Slater determinant, properly corrected with the sign function to account for the bosonic statistics, of the states. In the case of zero temperature $\vec{\eta} = \{1, \dots, N\}$ will label the lowest N single-particle energy states.

Lesser Green's function: $G^<(x,t,y,t')$.

We want to write the "lesser" Green's function ($G^<(x,t,y,t')$) for a TG gas as a function of single particle states directly. In order to easily apply that mapping, we should write the Green's function in the first quantization formalism. The main difference with the calculation of the RSPDM is that, because of dynamics, we have to perform two summations on the whole many-body Hilbert space that is reflected in the finale result into a small number of summations on the whole single-particle Hilbert space (eventually truncated). From the definition we can make explicit the time evolution:

$$\begin{aligned} \imath G^<(x,t,y,t')_\eta &= \left\langle \hat{\psi}^\dagger(y,t')\hat{\psi}(x,t) \right\rangle_\eta \\ &= \left\langle e^{iHt'}\hat{\psi}^\dagger(y)e^{-iHt'}e^{iHt}\hat{\psi}(x)e^{-iHt} \right\rangle_\eta \end{aligned} \tag{1.26}$$

In order to write it in the first quantization formalism and to apply the time evolution operator, we introduce the completeness relation in the $N-1$ particles Hilbert space $\sum_n |n\rangle\langle n| = \mathbb{I}_{N-1}$, with $|n\rangle$ being an eigenstate of the TG Hamiltonian and the sum being restricted on inequivalent states, and the completeness relation in the $N-1$ particles Hilbert space in the position representation $\frac{1}{N-1!}\int \mathrm{d}X\, |X\rangle\langle X| = \mathbb{I}_{N-1}$, with $X = x_2 \dots x_N$.

$$\begin{aligned} \imath G^<(x,t,y,t')_\eta &= \frac{1}{(N-1!)^2}\left\langle e^{iHt'}\hat{\psi}^\dagger(y)\int \mathrm{d}Y\, |Y\rangle\langle Y|\, e^{-iHt'}(\sum_n |n\rangle\langle n|)e^{iHt}\int \mathrm{d}X\, |X\rangle\langle X|\, \hat{\psi}(x)e^{-iHt}\right\rangle_\eta \\ &= \frac{1}{(N-1!)^2}\sum_n \int dY \int dX_{t'}\langle \eta|y,Y\rangle\, \langle Y|n\rangle_{t'\,t}\langle n|X\rangle\, \langle x,X|\eta\rangle_t \\ &= \frac{1}{(N-1!)^2}\sum_n \int dY\, \Psi^*_\eta(y,Y;t')\Psi_n(Y;t') \int dX\, \Psi_\eta(x,X;t)\Psi^*_n(X;t) \end{aligned} \tag{1.27}$$

We have used the definition of many-body wavefunction $\langle X|\eta\rangle = \Psi_\eta(X)$.

We can apply the mapping of eq. 1.5 for each many body obtaining the TG version of the precious equation:

$$\imath G^{<}(x,t,y,t') = \frac{1}{(N-1!)^2}\sum_n \int dX \prod_{k=2}^{N} sign(x-x_k)\Psi_\eta^F(x,X;t)\Psi_n^{*F}(X;t) \times \int dY \prod_{k=2}^{N} sign(y-y_k)\Psi_\eta^{*F}(y,Y;t')\Psi_n^F(Y;t') \tag{1.28}$$

Each one of the two many body integrals can be evaluated separately; we will start writing the first one as a function of single particle states, by using the Slater determinant definition. We identify the generic $(N-1)$ particles eigenstate of the free fermions Hamiltonian, labeled by n, as the one with SP orbitals $\vec{\alpha} = \{\alpha_2, ..., \alpha_N\}$. Expanding the determinant of $\psi_\eta^F(x,X;t)$ into the first column, we have

$$\begin{aligned}
&\int dX \prod_{k=2}^{N} sign(x-x_k)\Psi_\eta^F(x,X;t)\Psi_n^{*F}(X;t) \\
&= \sum_{i=1}^{N}(-1)^{i+1}\phi_{\eta_i}(x,t)\int dX \prod_{k=2}^{N} sign(x-x_k) \\
&\qquad \times \begin{vmatrix} \phi_{\eta_1}(x_2,t) & ... & \phi_{\eta_1}(x_N,t) \\ \vdots & ... & \vdots \\ \phi_{\eta_{i-1}}(x_2,t) & ... & \phi_{\eta_{i-1}}(x_N,t) \\ \phi_{\eta_{i+1}}(x_2,t) & ... & \phi_{\eta_{i+1}}(x_N,t) \\ \vdots & \vdots & \vdots \\ \phi_{\eta_N}(x_2,t) & ... & \phi_{\eta_N}(x_N,t) \end{vmatrix} \begin{vmatrix} \phi^*\alpha_2(x_2,t) & ... & \phi^*\alpha_2(x_N,t) \\ \vdots & \ddots & \vdots \\ \phi^*\alpha_N(x_2,t) & ... & \phi^*\alpha_N(x_N,t) \end{vmatrix}
\end{aligned} \tag{1.29}$$

We can combine the two determinants using the Andréief's integration formula of eq. 1.8. Then noticing the fact that $\int_{-\infty}^{\infty} sign(x-\bar{x})f(\bar{x})\mathrm{d}\bar{x} = \int_{-\infty}^{\infty} f(\bar{x})\mathrm{d}\bar{x} - 2\int_x^{\infty} f(\bar{x})\mathrm{d}\bar{x}$ we obtain

$$\int \mathrm{d}X \prod_{k=2}^{N} sign(x-x_k)\Psi_\eta^F(x,X;t)\Psi_n^{*F}(X;t) = (N-1)!\sum_{i=1}^{N}(-1)^{i+1}\phi_{\eta_i}(x,t)\det[\mathbf{P}(x,t)]_{\vec{\eta}\setminus\{\eta_i\},\vec{\alpha}}. \tag{1.30}$$

The determinant $\det[\mathbf{P}]_{\vec{\eta}\setminus\{\eta_i\},\vec{\alpha}}$ is the $N-1$ order minor of the matrix $\mathbf{P}$ having selected the rows $\vec{\eta}\setminus\{\eta_i\}$ and the columns $\vec{\alpha}$, and

$$\begin{aligned}
P_{l,m}(x,t) &= \int_{-\infty}^{\infty}\phi_l(\bar{x},t)\phi_m^*(\bar{x},t)\mathrm{d}\bar{x} - 2\int_x^{\infty}\phi_l(\bar{x},t)\phi_m^*(\bar{x},t)\mathrm{d}\bar{x} \\
&= \delta_{l,m} - 2\, e^{-\imath t(e_l-e_m)}\int_x^{\infty}\phi_l(\bar{x})\phi_m^*(\bar{x})\mathrm{d}\bar{x}
\end{aligned} \tag{1.31}$$

In the same way we can write the second integral in the expression for $G^<$, obtaining:

$$\imath G^<(x,t,y,t') = \widetilde{\sum_{\vec{\alpha}}} \sum_{i,j=1}^{N} (-1)^{i+j} \phi_{\eta_i}(x,t)\phi^*_{\eta_j}(y,t') \det[\mathbf{P}(x,t)]_{\vec{\eta}\setminus\{\eta_i\},\vec{\alpha}} \det\left[\mathbf{P}(y,t')\right]_{\vec{\alpha},\vec{\eta}\setminus\{\eta_j\}} \tag{1.32}$$

The sum over n corresponds to the sum over $\vec{\alpha}$ in the equation above, that has to be restricted to collections of indexes that are not related by permutations, and that will be indicated from now on by $\widetilde{\sum}$. This sum can be simplified by using the generalized Cauchy-Binet formula for the product of minors[4], obtaining:

$$(-1)^{i+j} \sum_{\vec{\alpha}} det[\mathbf{P}(x,t)]_{\vec{\eta}\setminus\{\eta_i\},\vec{\alpha}}\, det[\mathbf{P}(y,t')]_{\vec{\alpha},\vec{\eta}\setminus\{\eta_j\}} = (-1)^{i+j}\, det[\mathbf{P}(x,t)\mathbf{P}(y,t')]_{\vec{\eta}\setminus\{\eta_i\},\vec{\eta}\setminus\{\eta_j\}}$$
$$= \{[\mathbf{P}(x,t)\mathbf{P}(y,t')]_{\vec{\eta},\vec{\eta}}\}^{-1^T} det[\mathbf{P}(x,t)\mathbf{P}(y,t')]_{\vec{\eta},\vec{\eta}} \tag{1.34}$$

where in the last step we have used the definition of the inverse of a matrix via minors. It is important to note that the the product between matrices in the last equation is NOT constrained to the $\vec{\eta}$ elements of the single particle Hilbert space, but to the whole single particle Hilbert space (eventually truncated).

We can finally write:

$$\imath G^<(x,t,y,t') = \sum_{i,j=1}^{N} \phi_{\eta_i}(x) e^{-\imath e_{\eta_i} t} \phi^*_{\eta_j}(y) e^{\imath e_{\eta_j} t'} A_{\eta_i,\eta_j}(x,t,y,t') \tag{1.35}$$

with

$$\mathbf{A}_{\vec{\eta},\vec{\eta}}(x,t,y,t') = \{[\mathbf{P}(x,t)\mathbf{P}(y,t')]_{\vec{\eta},\vec{\eta}}\}^{-1^T} \det\left[\mathbf{P}(x,t)\mathbf{P}(y,t')\right]_{\vec{\eta},\vec{\eta}} \tag{1.36}$$

in clear analogy with the RSPDM expression of eq. 1.9 when $|\eta\rangle$ corresponds to the ground state.

Greater Green's Function

We want to write the "greater" Green's function ($G^>(x,t,y,t')$) for a TG gas as a function of single particle states directly, using the mapping to free fermions and developing the Slater determinants. As for the "lesser" one calculation, we should write the Green's function in the first quantization formalism. From the definition we can make explicit the time evolution:

[4]
$$\widetilde{\sum_{\vec{\alpha}}} \det[\mathbf{A}]_{\vec{I},\vec{\alpha}} \det[\mathbf{B}]_{\vec{\alpha},\vec{J}} = \det[\mathbf{A}\ \mathbf{B}]_{\vec{I},\vec{J}} \tag{1.33}$$

For a generic eigenstate of the many-body hamiltonian ($|\eta\rangle$), we can write:

$$\begin{aligned} \imath G^{>}(x,t,y,t')_\eta &= \left\langle \hat{\psi}(x,t)\hat{\psi}^\dagger(y,t') \right\rangle_\eta \\ &= \left\langle e^{iHt}\hat{\psi}(x)e^{-iHt}e^{iHt'}\hat{\psi}^\dagger(y)e^{-iHt'} \right\rangle_\eta \end{aligned} \tag{1.37}$$

In order to write it in the first quantization formalism and to apply the time evolution operator, we introduce the completeness relation in the $N+1$ particles Hilbert space $\sum_n |n\rangle\langle n| = \mathbb{I}_{N+1}$, with $|n\rangle$ being an eigenstate of the TG Hamiltonian and the sum being restricted on inequivalent states only, and the completeness relation in the N particles Hilbert space in the position representation $\frac{1}{N!}\int \mathrm{d}X\, |X\rangle\langle X| = \mathbb{I}_N$, with $X = x_1 \dots x_N$.

$$\begin{aligned} \imath G^{>}(x,t,y,t')_\eta &= \frac{1}{(N!)^2}\left\langle e^{iHt}\int dX\, |X\rangle\langle X|\, \hat{\psi}(x)e^{-iHt}(\sum_n |n\rangle\langle n|)e^{iHt'}\hat{\psi}^\dagger(y)\int dY\, |Y\rangle\langle Y|\, e^{-iHt'}\right\rangle_\eta \\ &= \frac{1}{(N!)^2}\sum_n \int dX \int dY\, {}_t\langle\eta|X\rangle\, \langle x,X|n\rangle_{t\ t'}\langle n|y,Y\rangle\, \langle Y|\eta\rangle_{t'} = \\ &= \frac{1}{(N!)^2}\sum_n \int dX \Psi^*_\eta(X;t)\Psi_n(x,X;t)\int dY \Psi_\eta(Y;t')\Psi^*_n(y,Y;t') \end{aligned} \tag{1.38}$$

We have used the definition of many-body wavefunction $\langle X|\eta\rangle = \Psi_\eta(X)$. We can apply the mapping of eq. 1.5 for each many body obtaining the TG version of the precious equation:

$$\begin{aligned} \imath G^{>}(x,t,y,t') = \frac{1}{(N!)^2}\sum_n \int \mathrm{d}X \prod_{k=1}^{N} sign(x-x_k)\Psi^{F*}_\eta(X;t)\Psi^F_n(x,X;t) \\ \times \int \mathrm{d}Y \prod_{k=1}^{N} sign(y-y_k)\Psi^F_\eta(Y;t')\Psi^{F*}_n(y,Y;t') \end{aligned} \tag{1.39}$$

Each one of the two many body integrals can be evaluated separately; we will start writing the first one as a function of single particle states, by using the Slater determinant definition. We identify the generic $(N+1)$ particles eigenstate of the free fermions Hamiltonian labeled by n, as the one with SP orbitals $\vec{\alpha} = \{\alpha_1, ..., \alpha_{N+1}\}$. Expanding the determinant of $\psi^F_n(x,X;t)$ into

the first column, we have

$$\int \mathrm{d}X \prod_{k=1}^{N} sign(x-x_k)\Psi^*_\eta(X;t)\Psi_n(x,X;t)$$
$$= \sum_{i=1}^{N+1} (-1)^{i+1}\phi_{\alpha_i}(x,t) \int \mathrm{d}X \prod_{k=1}^{N} sign(x-x_k)$$
$$\times \begin{vmatrix} \phi^*_{\eta_1}(x_1,t) & \dots & \phi^*_{\eta_1}(x_N,t) \\ \vdots & \ddots & \vdots \\ \phi^*_{\eta_N}(x_1,t) & \dots & \phi^*_{\eta_N}(x_N,t) \end{vmatrix} \begin{vmatrix} \phi_{\alpha_1}(x_1,t) & \dots & \phi_{\alpha_i}(x_{N+1},t) \\ \vdots & \dots & \vdots \\ \phi_{\alpha_{i-1}}(x_1,t) & \dots & \phi_{\alpha_{i-1}}(x_{N+1},t) \\ \phi_{\alpha_{i+1}}(x_1,t) & \dots & \phi_{\alpha_{i+1}}(x_{N+1},t) \\ \vdots & \vdots & \vdots \\ \phi_{\alpha_{N+1}}(x_1,t) & \dots & \phi_{\alpha_{N+1}}(x_{N+1},t) \end{vmatrix} \tag{1.40}$$

As for the lesser GF, we can combine the two determinants using the Andréief's integration formula of eq. 1.8. Then noticing the fact that $\int_{-\infty}^{\infty} sign(x-\bar{x})f(\bar{x})\mathrm{d}\bar{x} = \int_{-\infty}^{\infty} f(\bar{x})\mathrm{d}\bar{x} - 2\int_{x}^{\infty} f(\bar{x})\mathrm{d}\bar{x}$ we obtain

$$\int \mathrm{d}X \prod_{k=1}^{N} sign(x-x_k)\Psi^{F*}_\eta(X;t)\Psi^F_n(x,X;t) = N! \sum_{i=1}^{N+1}(-1)^{i+1}\phi_{\alpha_i}(x,t)\, det[\mathbf{P}(x,t)]_{\vec{\alpha}\setminus\{\alpha_i\},\vec{\eta}} \tag{1.41}$$

The determinant $\det[\mathbf{P}(x,t)]_{\vec{\alpha}\setminus\{\alpha_i\},\vec{\eta}}$ is the N order minor of the matrix $\mathbf{P}$ having selected the rows $\vec{\alpha}\setminus\{\alpha_i\},\vec{\eta}$ and the columns $\vec{\eta}$, and $P_{l,m}(x,t)$ defined as in eq. 1.31. The main difference with the "Lesser" calculation is that in this form we cannot apply the Cauchy-Binet theorem. We have to reinsert all the $\phi_{\alpha_i}(x,t)$ elements into an extended "P" matrix, by adding a "0" column, as it follows:

$$\int dX \prod_{k=1}^{N} sign(x-x_k)\Psi^{F*}_\eta(X;t)\Psi^{F*}_n(x,X;t) = N!\det\left[\vec{\phi}(x,t),\mathbf{P}(x,t)\right]_{\vec{\alpha},\{0\}\cup\vec{\eta}} \tag{1.42}$$

in which we have defined a column vector $\vec{\phi}(x,t) = [\phi_1(x,t),\dots,\phi_M(x,t)]^T$ on the whole Hilbert space (eventually truncated at M states). Following the same line for the second integral, we reach:

$$\imath G^{>}(x,t,y,t') = \widetilde{\sum_{\vec{\alpha}}} det\begin{bmatrix}\vec{\phi}(y,t')^\dagger \\ \mathbf{P}(y,t')\end{bmatrix}_{\{0\}\cup\vec{\eta},\vec{\alpha}} det\left[\vec{\phi}(x,t) \qquad \mathbf{P}(x,t)\right]_{\vec{\alpha},\{0\}\cup\vec{\eta}} \tag{1.43}$$

The sum $\widetilde{\sum}_{\vec{\alpha}}$ has to be restricted to collections of indexes that are not related by permutations. Now we can apply the generalized Cauchy-Binet formula,

for products between determinats, obtaining:

$$\begin{aligned}\imath G^{>}(x,t,y,t') &= det\begin{bmatrix}\vec{\phi}(y,t')^\dagger\vec{\phi}(x,t) & \vec{\phi}(y,t')^\dagger\mathbf{P}(x,t)\\ \mathbf{P}(y,t')\vec{\phi}(x,t) & \mathbf{P}(y,t')\mathbf{P}(x,t)\end{bmatrix}_{\{0\}\cup\vec{\eta},\{0\}\cup\vec{\eta}}\\ &= \det\big[\mathbf{P}(y,t')\mathbf{P}(x,t)\big]_{\vec{\eta},\vec{\eta}}\\ &\times\Big(\vec{\phi}(y,t')^\dagger\vec{\phi}(x,t) - [\vec{\phi}(y,t')^\dagger\mathbf{P}(x,t)]_{1,\vec{\eta}}\,[\mathbf{P}(y,t')\mathbf{P}(x,t)]^{-1}_{\vec{\eta},\vec{\eta}}\,[\mathbf{P}(y,t')\vec{\phi}(x,t)]_{\vec{\eta},1}\Big)\end{aligned} \tag{1.44}$$

in which all the products, where not indicated, should be thought as in the whole Hilbert space (eventually truncated).

Summary

The lesser and greater Green's functions for an eingenstate η of the TG hamiltonian of eq. 1.1 can be expressed as:

$$\imath G^{<}(x,t,y,t') = \det\big[\mathbf{P}(x,t)\mathbf{P}(y,t')|_{\vec{\eta}\vec{\eta}}\big]a^{<}(x,t,y,t') \tag{1.45a}$$

$$\imath G^{>}(x,t,y,t') = \det\big[\mathbf{P}(y,t')\mathbf{P}(x,t)|_{\vec{\eta}\vec{\eta}}\big]a^{>}(x,t,y,t') \tag{1.45b}$$

with

$$a^{<}(x,t,y,t') = \vec{\phi}(x,t)^T_{\vec{\eta}}\,[\mathbf{P}(x,t)\mathbf{P}(y,t')]^{-1T}|_{\vec{\eta}\vec{\eta}}\,\vec{\phi}^*(y,t')_{\vec{\eta}} \tag{1.46a}$$

$$\begin{aligned}a^{>}(x,t,y,t') = \vec{\phi}(y,t')^\dagger\vec{\phi}(x,t) - [\vec{\phi}(y,t')^\dagger\mathbf{P}(x,t)]_{\vec{\eta}}\\ [\mathbf{P}(y,t')\mathbf{P}(x,t)]^{-1}|_{\vec{\eta}\vec{\eta}}\,[\mathbf{P}(y,t')\vec{\phi}(x,t)]_{\vec{\eta}}\end{aligned} \tag{1.46b}$$

we have defined the single-particle eigenfunctions column-vector $\vec{\phi}(x,t) = [\phi_1(x,t),\ldots,\phi_M(x,t)]^T$, the signed overlap $\mathrm{P}_{lm}(x,t) = \delta_{l,m} - 2\,e^{-\imath t(e_l-e_m)}\int_x^\infty \phi_l(\bar{x})\phi_m^*(\bar{x})\mathrm{d}\bar{x}$ where ϵ_l is the eigenenergy corresponding to the state $\phi_l(x)$. For fixed spatial and temporal coordinates all the products have to be intended in the whole single-particle Hilbert space and then restricted to the states in $\vec{\eta}$.

From the above expressions it is possible to recover the limit of non-interacting fermions by setting $\mathrm{sign}(x-y) = 1$, obtaining $P_{l,m}(x,t) = \delta_{l,m}$ and so $G_F^{<}(x,t,y,t') = \imath\sum_{\vec{\eta}} e^{\imath e_i t'}\phi_i^*(y)\phi_i(x)e^{-\imath e_i t}$ and $G_F^{>}(x,t,y,t') = -\imath\sum_{\bar{\vec{\eta}}} e^{\imath e_i t'}\phi_i^*(y)\phi_i(x)e^{-\imath e_i t}$ that are the right single particle GFs for a gas of N non interacting fermions in the states $\vec{\eta}$ [81].

Most importantly our expressions for the lesser Green's function in Eq. (1.45a) contains as a limiting case the result derived by Pezer and Buljan in Ref. [18] and reviewed in sec. 1.1.1 for the single-particle density matrix $\rho(x,y) = -iG^{<}(x,0;y,0)$. This is an important point, because the algorithm to compute the density matrix in Ref. ([18]) is still one of the most efficient, and allowed to perform several studies on the properties of the TG. Therefore

it is important to stress that, due to the formal analogy of our expression for the lesser Green's function with that in Ref. ([18]), the computational complexity for each given pair of times (t, t') is nearly the same, except the unavoidable sums on the whole single particle Hilbert space.

Another point to mention is that the requirement to truncate the whole Hilbert space has to be done carefully, especially in the case of out-of-equilibrium dynamics such as quantum quenches, where a change in the Hamiltonian's parameters might be in order. We also want to point out that, although both the above expressions and their derivation refer to a many-body state with N particles, they could be generalized to a grand-canonical ensemble following for instance the derivation in Refs. [17, 28].

1.2 TG and fermionic gas in a quasiperiodic potential

1.2.1 Single particle problem

Let us consider the time independent Schrödinger equation for a particle in an external potential:

$$\left[-\frac{\hbar^2}{2m}\frac{\partial^2}{\partial x^2} + V_{ext}(x)\right]\psi_n(x) = e_n\psi_n(x). \tag{1.47}$$

In what follows, we will consider an external potential which describes a bichromatic lattice,

$$V_{ext}(x) = V_1 \sin^2(k_1 x) + V_2 \sin^2(k_2 x)\,. \tag{1.48}$$

Although any irrational number would work as well, to be specific we will take $k_1/k_2 = (1+\sqrt{5})/2 = \tau$, the golden ratio, and assume $V_1 > V_2$. For $V_2 = 0$ and $V_1 \geq 5E_R$ it is possible to resort to the so called tight-binding (TB) limit to approximately describe the system. Here $E_R = \hbar^2 k_1^2/(2m)$ is the recoil energy associated to the first potential, giving an estimation of the energy at which the modulation V_1 opens the first gap of width $\propto V_1$ in the otherwise gapless free particle spectrum (for $V_1 = V_2 = 0$). The above condition therefore ensures that all particles with energy $E < E_R$ do not have enough energy to overcome the first gap and, therefore, that they are confined in the lowest band of the potential. In this limit, the properties of the system are dominated by the external potential and it is possible to rewrite the single particle Hamiltonian in Eq. (1.47) in terms of states $|i\rangle$, localized around the minima of the potential, whose wave functions $w_i(x) = \langle x|i\rangle$ are the so called Wannier functions. In the presence of the second potential $V_2 < V_1$, and in the TB limit, the continuum model described by Eq. (1.47) can be mapped into the so called Aubry-André model (AAM):

$$\hat{H} = \Delta\sum_j \cos(2\pi\tau j)\,|j\rangle\langle j| - \frac{J}{2}\sum_j(|j+1\rangle\langle j| + |j\rangle\langle j+1|). \tag{1.49}$$

The first term on the r.h.s., proportional to Δ, accounts for the on-site energy, whereas the second one, proportional to the hopping constant J, is responsible for nearest-neighbor tunnelling between adjacent sites. Both Δ and J depend upon the choice of the set of Wannier functions, which in turn depend upon the first potential only if the condition $V_2 \ll V_1$ is satisfied.

The AAM has been widely studied from different points of view. For what we are concerned here, it is worth recalling that the AAM shows a delocalized-to-localized (or metal-to-insulator) transition at $\Delta/J = 1$. This point marks the change from a delocalized phase ($\Delta/J < 1$), in which all of the eigenstates have an extended character with a corresponding absolutely continuous spectrum, to a phase where all states are localized and the spectrum is discrete [37]. As for the many-body properties of this system, it has been predicted numerically and verified experimentally that bosons with the addition of on-site interaction in the AAM enjoy a particularly rich phase diagram, which includes a superfluid to Bose-glass transition at low filling, and also a Mott insulator phase for higher filling and interaction strength.

In the continuum, outside the range of validity of the TB approximation, it is known that the sharp delocalized-to-localized transition of the lowest energy band transforms into a mobility edge, whose position in energy changes with V_2 [48, 49]. Our aim is to study in detail how this crossover from the discrete to the continuum behavior occurs, and to show that signatures of this transition are displayed in the many-body properties of both non-interacting fermions and strongly-interacting bosons. We will therefore always work with the continuous model of Eq. (1.47) and move from the discrete to the continuous limits by changing the strength of the main potential V_1. For each set of parameters $\{V_1, V_2\}$ we have numerically solved the eigenvalue problem given by Eq. (1.47) via a fifth order Matrix Numerov Method [113], considering systems with $N_s = 100$ lattice sites and total length $k_1 L = 100\pi$.

Mobility edge in the single particle problem In the discrete model, all of the eigenfunctions of the Hamiltonian of Eq. (1.47) in the TB regime are either extended or localized, depending on weather the value of V_2 is below or above a certain threshold value V_2^t. On the other hand, if $V_1 < 5E_R$ a Mobility Edge (ME) appears such that, for a fixed value of V_2, states with energy lower then the ME are localized whilst the others are delocalized [50]. The ME is found at higher energies for increasing V_2. It is possible to obtain an estimation of the localization threshold V_2^t by calculating explicitly Δ and J of the AAM – as a function of V_1 and V_2 – and inverting the condition $\Delta/J = 1$, by solving for V_2.

From Eqs. (14) and (15) of ref. [38] and by fitting the free parameters in those equations with our data, we obtain the following expression for V_2^t:

$$V_2^t = 2E_{R_2} 14.9752 e^{\frac{0.381966}{\sqrt{V_1/E_{R_1}}} - 2.07\sqrt{V_1/E_{R_1}}} (V_1/E_{R_1})^{0.98} \tag{1.50}$$

In the following we will use the rescaled quantity $v_2 = V_2/V_2^t$ in order to compare systems with different V_1 and V_2. This guarantees that the transition point in the TB limit always occurs at $v_2 = 1$. However, it is important to notice that the computation of V_2^t is meaningful only in the TB limit. As we will also consider parameters for which the TB approximation does not hold, then the value $v_2 = 1$ will lose its importance and its role of transition point. To quantitatively discuss the transition in the general case, we will employ the Inverse Participation Ratio $\mathrm{IPR}(\psi) = \int |\psi(x)|^4 dx / \int |\psi(x)|^2 {}^2 dx$ for the eigenfunctions of the first energy band of the Hamiltonian. This quantity measures the inverse of the average spatial region occupied by the eigenfunction. We will consider an eigenfunction to be localized if its IPR is larger than $1/(5l)$ where l is the distance between two neighbor lattice sites. Fig. 1.1 shows the number of localized states as a function of V_2 for different values of V_1: in the TB regime (upper, red curve) the transition is sharp, whereas in the continuum there is an ME, as witnessed by the plateau in Fig. 1.1, that correspond to the gaps opened by V_2 inside the first energy band. Moreover, as anticipated above, Fig. 1.1 shows that the estimation of the transition point V_2^t given in Eq. (1.50) fails when the TB description does not provide a good approximation (see, e.g. the lower curve, corresponding to $V_1 = E_R$). We finally show in Fig. 1.2 the IPR of the ground state wave function, normalized to one lattice length, together with the function itself and its Fourier transform for various values of v_2.

In the remainder of the chapter we will show how both the sharp transition, occurring in the TB limit, and the appearance of the ME affect the many-body properties of non-interacting spinless fermions and Tonks-Girardeau bosons. It is known that the excitation spectrum of the Tonks-Girardeau model is the same as that of non-interacting spinless fermions and that all local quantities are the same for the two systems. On the other hand, non local quantities, such as the momentum distribution, are different and reveal the fermionic and bosonic nature of the two systems. More importantly, we shall see that the different statistical nature of the two kind of particles also shows up in the way the localization transition and the appearance of the ME manifest themselves in the momentum distributions.

1.2.2 Fermions in a bichromatic lattice

In this section, we consider the effect of the ME of the single-particle spectrum on the ground state properties of a system of N non-interacting fermions loaded into the bichromatic lattice, and, more generally, discuss the signatures of the transition from discrete to continuum, occurring as V_1 is decreased.

The many-body wavefunction describing a system of N non-interacting spinless fermions is given by a Slater determinant of single particle states (see Eq. (1.3)). Below, we focus on the reduced single particle density matrix (RSPDM), defined in eq. (1.6), whose knowledge is sufficient to evaluate the

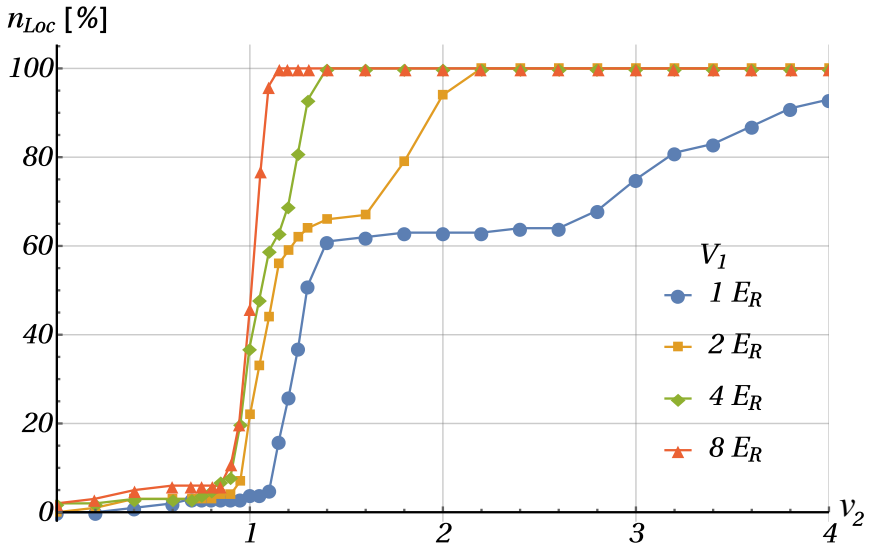

Figure 1.1: Number of localized states as a function of v_2 for different values of V_1. An eigenfunction is considered to be localized if its IPR is greater than $1/5l$ where l is the distance between two neighboring sites. For the system considered here, $5l$ corresponds to the 5%of the whole lattice length L.

expectation values of all single-particle operators, and its Fourier transform, the momentum distribution (MD), defined in eq. (1.12), which is directly measurable in cold atom experiments. For non interacting fermions, both can be evaluated by using single particle wavefunctions only via eq. (1.14) and eq. (1.15).

We analyze the TB limit first, where, interestingly enough, the MD offers a signature of the localization transition inherited from the single particle properties. On the delocalized side, the Fourier transform of each single particle state displays peaks at the wave numbers $k(m,n) = 2mk_1 + 2nk_2$ with $m, n \in \mathbb{Z}$, and the MD shows several Fermi-Dirac-like flat structures due to the occupation of states with nearby momentum peaks. This is shown in Fig. 1.3, where explicit reference to gases of $N = 15$ and $N = 65$ fermions is made. In the delocalized region ($v_2 < 1$), indeed, some nearly flat regions appear in the MD. They are centered at different $k(n,m)$'s, and are due to the fact that each single particle wavefuction contributes with at least two momenta (but in general more, for higher energy states); these momenta pile up in the total $n(k)$ to give a sequence of nearby peaks forming these Fermi-Dirac-like (almost) flat regions, whose width is proportional to the number of particles.

On the other hand, again in the TB regime, but now in the localized domain, the MD suddenly smoothens for $v_2 > 1$, due to the fact that single

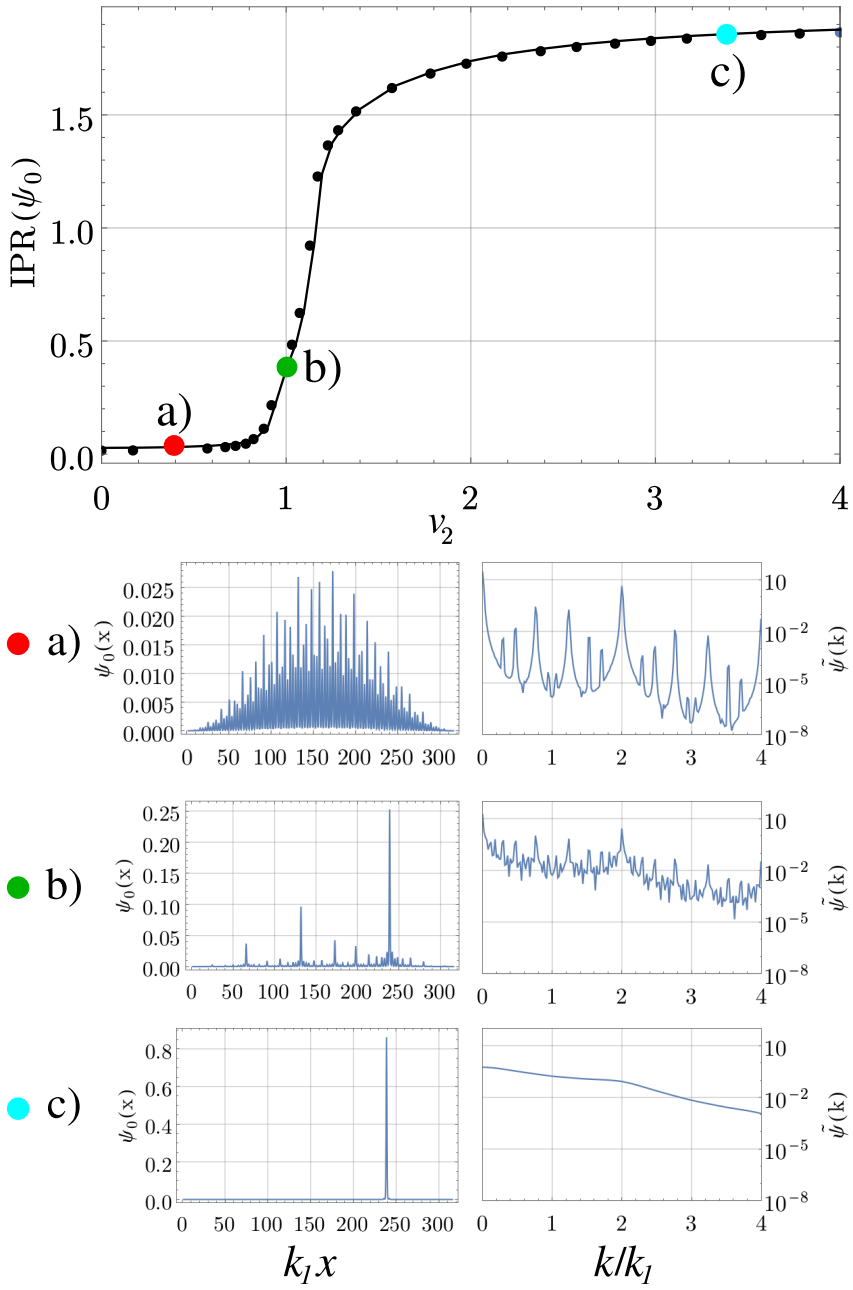

Figure 1.2: (Top) Normalized IPR of the single particle ground state of the system as a function of v_2 for $V_1 = 8E_R$. (Bottom) Single particle ground state and its Fourier Transform in the delocalized, critical and localized regions corresponding to the values of v_2 reported in red, green and cyan colors, respectively, in the top figure.

particle states are all localized, so that their Fourier transform flattens over in momentum space. Before shifting our attention to the continuum case, it is instructive to discuss the nature and origin of the structures that appear at the edges of the flat regions. They are particularly well visible in the case of $N = 65$. Conversely, for $N = 15$, they only show up as very small peaks, whose height slightly increases with increasing v_2 until the transition point $v_2 = 1$ is reached, where they disappear leaving structure-less bumps.

To understand why this happens, we recall that the addition of the second potential leads to a fragmentation of the energy spectrum into sub-bands separated by gaps whose width depends, at first order in a perturbation analysis, on the amplitudes of the Fourier transform of the potential itself. Furthermore, the sub-bands tend to flatten out as the potential is increased. This implies that the density of states increases at the sub-band edges and more particles can be accommodated there. As a result, the structures at the edges of the flat regions become better and better defined as the number of particles increases.

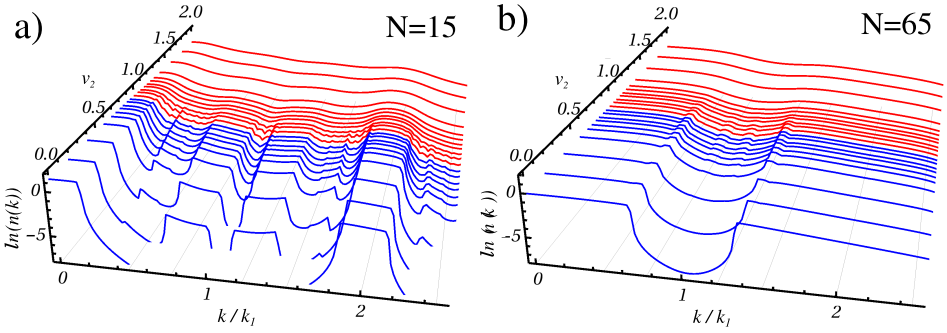

Figure 1.3: Momentum distribution $n(k)$ as a function of v_2 for a system of non-interacting fermions with $V_1 = 8E_r$ (TB limit). The two panels refer to a different number of fermions: a) N=15 and b) N=65. Blue and red curves are for $v_2 < 1$ and $v_2 > 1$ respectively.

In the continuum, namely $V_1 \approx E_R$, the delocalized-to-localized transition turns into the appearance of an ME. Indeed, Fig. 1.4 b) shows that it is possible to observe structures in the MD of an $N = 65$ fermion gas at any value of v_2, and in particular well beyond the transition point $v_2 = 1$, which used to mark a sharp transition in the TB approximation. The persistence of such structures is a signature of the existence of occupied single particle states, which remain delocalized beyond $v_2 = 1$.

However, this seems not to be the case if one looks at Fig. 1.4 a), where $n(k)$ is shown for $N = 15$ fermions, instead. Here, the structures of the MD quickly disappear when increasing v_2 beyond 1. In fact, as we considered a smaller number of fermions in this case, less states are occupied, and all of them become localized for $v_2 > 1$ (giving rise to a quick smoothing of $n(k)$).

The comparison between Fig. 1.4 a) and Fig. 1.4 b), therefore, shows that, in the same band, there exist both localized single particle states (at low energy) and delocalized ones (at higher energy), which is a clear manifestation of the ME.

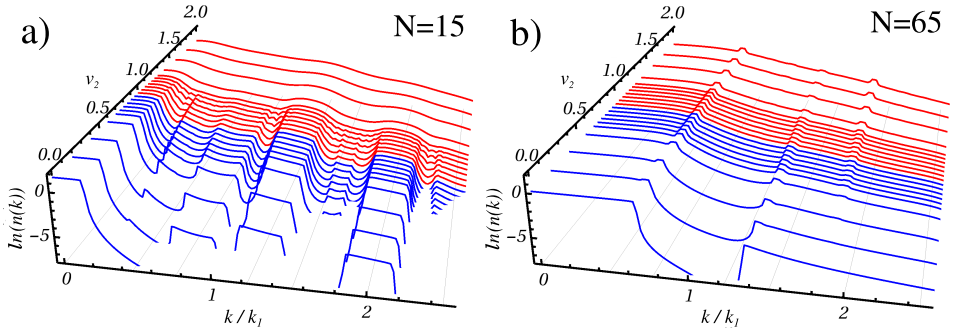

Figure 1.4: $n(k)$ as a function of v_2 for a system of non-interacting fermions with $V_1 = E_r$. The same parameters and coloring as Fig. 1.3 is used. A persistence of the edge-structures well beyond $v_2 = 1$ is observed for $N = 65$, but not for $N = 15$ as, for these parameters, the first 15 single particle states remain below the ME.

In order to characterize quantitatively this phenomenon, we resort to an approach already used in Ref. [114] to study the degree of delocalization of phonon modes in quasi-crystalline structures. The idea behind it is to evaluate the area under the MD peaks, in order to quantify the total power spectrum coming from coherent sources, which in our case correspond to delocalized single particle states. Because we would like to quantify the presence of isolated peaks, as explained in Fig. 1.4, that manifests the existence of the mobility edge, we have removed a continuous ("smooth") background from the MD and then we have evaluated the total area I_d below the edge-peaks. On the delocalized side ($v_2 < 1$) I_d increases as a function of v_2 due to the appearance of new peaks, induced in the single particle states by the second potential, when the transition point is approached. Moreover, for small numbers of fermions ($N = 15$) such an increase is approximately linear, up until saturation is reached. This behavior stems from the fact that only the lower energy eigenstates are occupied and, therefore, large values of the second potential are needed to make them develop a spatial structure, which involves more momenta. On the other hand, for $N = 65$, saturation occurs well before, due to the fact that higher energy eigenstates are occupied even at small values of v_2, which contribute to $n(k)$ with more momenta and, therefore, more peaks.

When the localized eigenstates start to be occupied, I_d decreases due to the smoothing of the MD profile. In the TB-regime, I_d suddenly goes to zero

for $v_2 > 1$, regardless of the number of fermions, as all of the eigenstates suddenly localize. On the other hand, in the continuous limit with $V_1 \approx E_r$, we observe the appearance of an ME as I_d decreases for $v_2 > 1$ and reaches a plateau (blue and yellow curves in Fig. 1.5 b). The plateau, in particular, witness the ME moving through the band towards higher energies.

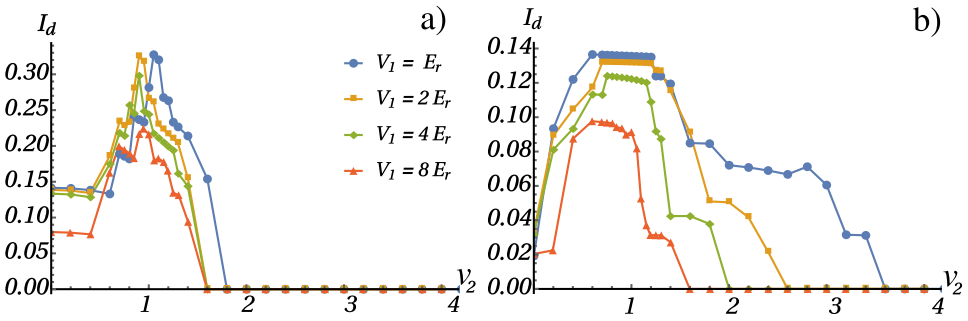

Figure 1.5: Area under the edge peaks, I_d, for a) $N = 15$ and b) $N = 65$ fermions.

1.2.3 Tonks-Girardeau gas in a bichromatic lattice

In Sec.1.2.2 we have seen that signatures of the ME appear in the momentum distribution of the the RSPDM of a many-body system of spinless fermions. In this section we look at a strongly-interacting boson gas (i.e., the Tonks-Girardeau gas), whose ground state properties can be related to the fermionic ones via the prescription outlined in Sec.1.1.

The many body spectrum of a hard-core boson system is, in fact, the same as that of the noninteracting fermion gas, loaded into the same optical potential $V(x)$. Moreover, it is possible to show that the mapping from hard-core bosons to non-interacting fermions leaves all *local* quantities unchanged; for instance, given the many-body wavefunction for N hard-core bosons, the density of bosons is the same as that of N non interacting fermions. Conversely, non-local properties, such as correlation functions, are different in the two cases. For this reason we expect the MD, which is derived from the off-diagonal entries of the RSPDM, to be markedly different from that observed in Sec.1.2.2, because of the presence of spatial coherences, typical of a boson gas.

In Ref. [18], it has been shown that the RSPDM and the momentum distribution of N hard-core bosons can be obtained by the single particle eigenstates of the equivalent non-interacting fermion problem (see Sec. 1.1.1 and eqs. (1.9) (1.12))

As expected, the bosonic MD is markedly different from that of the non-interacting fermion case. Due to their bosonic nature, at zero temperature the particles would tend to occupy the single particle modes with lowest

energy. On the other hand, due to the very strong repulsion between two bosons in states with a large spatial overlap, particles tend to occupy states in such a way as to lower their overlap. The interplay between these two effects is the key mechanism that explains the behavior of the MD for strongly interacting bosons, which we will now analyze.

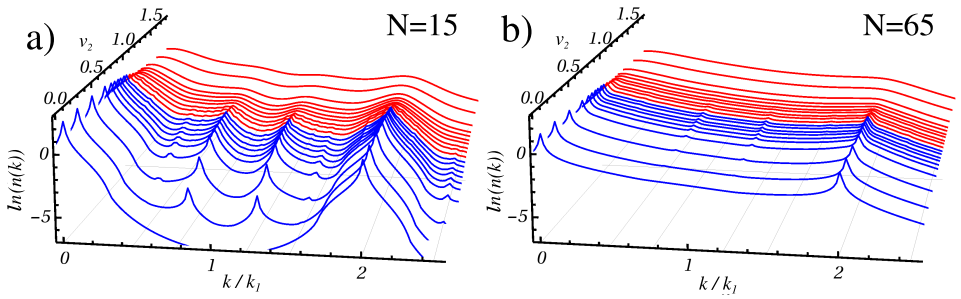

Figure 1.6: Momentum distribution $n(k)$ as a function of v_2 for a system of strongly-interacting bosons with $V_1 = 8E_r$ (TB limit). Different figures refer to a different number of bosons: a) N=15 and b) N=65. Blue and red curves are for $v_2 < 1$ and $v_2 > 1$ respectively.

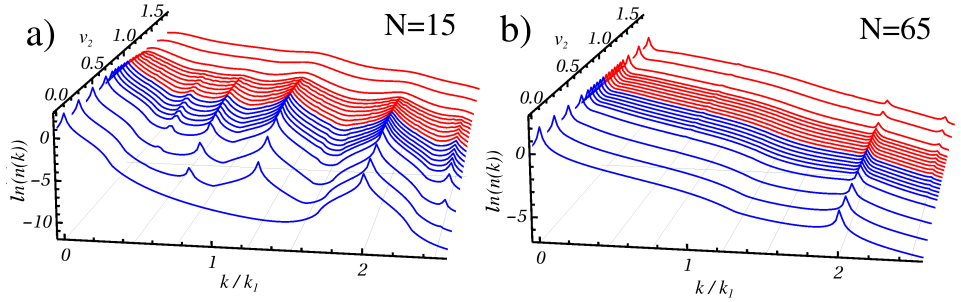

Figure 1.7: Momentum distribution $n(k)$ as a function of v_2 for a system of strongly-interacting bosons with $V_1 = E_r$. The two figures are drawn for: a) N=15, and b) N=65 bosons in the lattice. Blue and red curves are for $v_2 < 1$ and $v_2 > 1$ respectively.

On the delocalized side $v_2 < 1$, the sharp peaks of the noninteracting fermion case are replaced by broad peaks centered at specific momenta of the form $k(m, n) = 2mk_1 + 2nk_2$, induced by the trapping potential.

Indeed, as stated above, bosons would want to occupy a low energy mode, but not all of them can occupy the same one, as this would lead to a large overlap between their wavefunctions and, therefore, to an increase of the total energy. This effect is taken into account by the presence of the factors A_{ij} in the RSPD matrix, as built from single particle eigenfunctions in Eq.

(1.9). Such a behavior gets more and more pronounced with increasing the number of bosons, as witnessed by panel a) and b) in Fig. 1.6, where we display the MD for $V_1 = 8E_r$ in a system of $N = 15$ and $N = 65$ bosons as a function of v_2. In the first case (Fig. 1.6 a), $N = 15$), two new peaks appear as the second potential is switched on, which are very well pronounced and persist up until the transition point $v_2 = 1$ is reached. For $v_2 > 1$, instead, the peaks broaden, $n(k)$ smoothen out and any structure is lost.

In the second case (Fig. 1.6 b), $N = 65$), the two peaks emerge from an already large background, which is due to the large number of bosons in the system that tend to occupy more states. This implies that the tails of the main peaks, due to the main potential V_1, are quite high. Notwithstanding the fact that they are immersed in these tails, they are still visible, therefore witnessing the spatial coherence of delocalized modes.

When moving away from the TB regime, as for the fermionic gas, we find that the presence of the single particle mobility edge is reflected into the bosonic MD: in Fig. 1.7b, which shows the MD for 65 bosons, the two main peaks described above persist at high value of v_2, witnessing the coexistence of localized and delocalized single particle states. In Fig. 1.7a for $N = 15$, peaks due to the delocalized levels are shown to survive slightly beyond the threshold, being rapidly washed out as the ME quickly moves above the occupied states with increasing v_2. For a larger number of bosons, instead, the peaks are still clearly visible even for larger amplitudes of the second potential.

To better highlight such structures, we performed a peak-area analysis, similar to that discussed for fermions (Fig. 1.8).

The discrete part of the bosonic MD, as quantified by the parameter I_d, differently from the fermionic case, monotonically decreases with v_2, as the peak broadening due to the localization gives a more pronounced effect than the tendency of the bosons to create new structures. A comparison with the corresponding picture for the fermion case, Fig. 1.5, shows that, for fermions, it was exactly the other way around.

Coming back to the interacting boson case, Fig. 1.8a shows that, for a small number of particles, I_d quickly decays to zero near $v_2 = 1$ because of the sudden transition of the whole range of occupied single particle states. On the other hand, for a larger number of particle, $N = 65$ in Fig. 1.8b, the behavior of the tight-binding versus the continuum regime is different. While the transition in the former is always sudden (red line in Fig. 1.8b), independently of the particles number, the presence of ME in the latter implies a smooth decrease of I_d (see, e.g. the blue line in Fig. 1.8b, which reaches zero only for $v_2 > 3$), meaning, once again, that high energy delocalized single particle states are still populated when the low energy ones are localized.

Unlike the non-interacting fermion case, where the occupancy of each natural orbital was either 0 or 1, here it is meaningful to look at their distribution and at the entropy of the RSPDM given by $S(\rho_B) = -\sum_i \lambda_i \ln \lambda_i$.

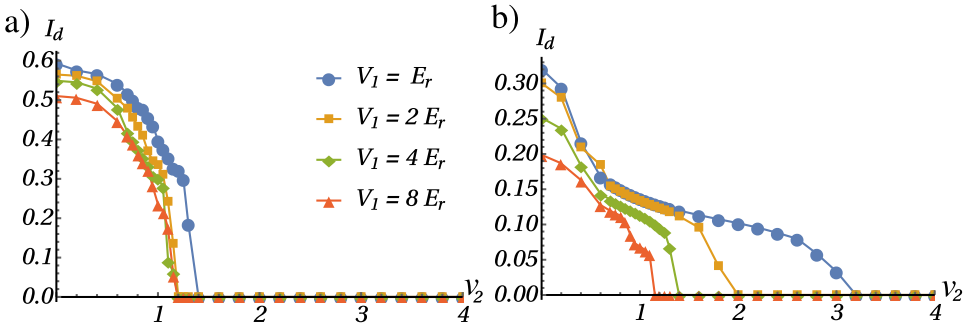

Figure 1.8: Area under the discrete peaks, I_d, as a function of v_2 for various values of V_1, and for a) $N = 15$ and b) $N = 65$ bosons.

For N strongly interacting bosons at the absolute zero, we should not always expect that the first N energy levels are occupied, and, correspondingly, $S(\rho_B) \neq \ln N$. However, we expect the entropy to reach such a value in

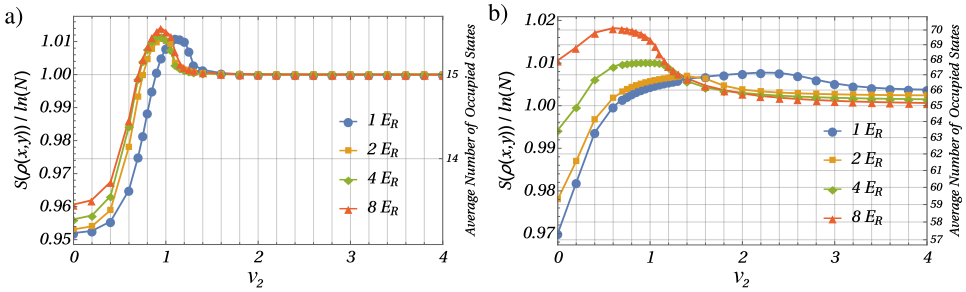

Figure 1.9: Entropy of the RSPDM for (top) $N = 15$ and (bottom) $N = 65$ bosons in the Tonks-Girardeau regime.

the *localized phase*, where *i*) the eigenstates are exponentially localized in space and, therefore, the strong interaction forbids more than one boson to occupy an energy level, and *ii*) there is a one-to-one correspondence between energy eigenfuntions and natural orbitals. As a result, the occupancy of the first N natural orbitals is 1, as for fermions, the non-zero eigenvalues are all equal to $1/N$ and the entropy is $\ln N$. On the other hand, in the delocalised phase, the occupation of natural orbitals changes, with λ_i decreasing almost-exponentially with i, and the entropy can take on an arbitrary value $S(\rho_B) > 0$; e. g. $S(\rho_B) = \ln N_{occ}$ if N_{occ} natural orbitals are equally occupied. For weakly interacting bosons at zero temperature, in the superfluid phase, we have $S(\rho_B) \ll \ln N$ because they all tend to occupy the same energy level. As the interaction is increased (but always remaining within the superfluid phase), we expect bosons to spread in the Hilbert space, resulting in the occupancy of other natural orbitals, allowing for a more dilute distribution. This, in turn, leads to $S(\rho_B) > \ln N$. In Fig. 1.9 we show the entropy

$S(\rho_B)/\ln N$ as a function of v_2 and for different values of the main potential strength V_1 going from the TB to the continuum limits, for the cases of $N = 15$ [Fig. 1.9 a)], and $N = 65$ bosons [Fig. 1.9 b)]. It can be seen that, as expected, deep in the localized phase $v_2 > 1$, the entropy tends to $\ln N$, showing that bosons tend to occupy one natural orbital each. It is interesting to compare the behavior of the entropy for $v_2 < 1$ for low and large numbers of Bosons. In the first case ($N = 15$), the entropy is smaller than $\ln N$ away from the transition point $v_2 \approx 1$, while it exceeds this value around it. In the second case ($N = 65$), the entropy exceeds $\ln N$ even in the delocalized phase for $V_1 \gg E_r$ (TB limit). In this limit, indeed, the eigenfunctions are delocalized across the whole system, but their amplitudes show an increase around the minima of the main potential (i.e. V_1). Therefore two bosons residing in the same single particle eigenfuction would both be localized around the minima; as the interaction increases they naturally tend to occupy other excited states in order to reduce the average overlap of their wavefunctions. This is why they would tend to occupy more eigenstates, resulting in a number of occupied natural orbitals larger than N. On the other hand, as the system is brought in the continuous limit (e.g., for $V_1 \approx E_r$), bosons are allowed to also occupy regions between the minima of the potential, and therefore the above effect is less important and the entropy drops below $\ln N$.

Furthermore we can see that the entropy signals the presence of the ME. To see this we again compare the two cases $N = 15$ and $N = 65$ for $V_1 = E_r$ (blue circles in Fig. 1.9). In the first case, the entropy rapidly reaches the asymptotic value $\ln N$, showing the fermion-like behavior of bosons which occupy one natural orbital each. Conversely, for $N = 65$ the asymptotic value is attained for higher values of v_2, showing that some delocalized states are occupied.

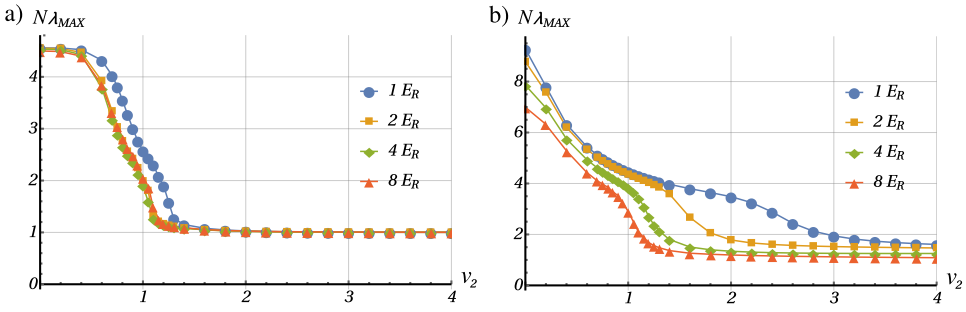

Figure 1.10: Fraction of particles in the most largely occupied natural orbital, given by $N\lambda_{MAX}$ for a) $N = 15$ and b) $N = 65$ bosons in the Tonks-Girardeau regime.

We can also consider the behavior of the largest eigenvalue λ_k of the RSPDM (Fig. 1.10). As expected, in the localized phase it asymptotically

goes to $1/N$ (as all the first N eigenvalues do), whereas, in the delocalized region, it becomes larger. Once again, the presence of the ME in the continuum is witnessed by the fact that λ_k decays less rapidly as a function of v_2 (blue circles in Fig. 1.8 b)).

1.3 Spectral Function in a lattice

In this section, we exploit to study of the properties of the spectral function for the Tonks-Girardeau gas immersed in a periodic lattice, for different system parameters, and compare it with analytical prediction of its asymptotic behavior. In order to perform this analysis, we implement a numerical calculation of the single particle Green's function based on eqs. (1.45a) and (1.45b).

In what follows we will focus on the case of TG bosons on a lattice of $L = 256$ sites, with N particles at $T = 0$ and therefore only the first N single-particle fermionic eigenstates are filled. The Hamiltonian of the system is

$$\hat{H} = -\frac{J}{2}\sum_{i=1}^{L} \hat{b}_i \hat{b}_{i+1} + \text{h.c.} \tag{1.51}$$

and the effect of the interaction is accounted via the mapping into non-interacting fermions. We consider open boundary conditions.

1.3.1 Analysis of the spectral properties

We are now in a position to study the spectral function of a TG gas on a lattice given by eq. (1.24), using the expressions for the Green's functions that we have determined in eqs. (1.45a) and (1.45b) . One example is shown in Fig. 1.11 for a system with $N = 64$ particles and where ϵ_F is the Fermi energy of the corresponding Fermi gas. While the spectral function for non-interacting fermions is $A(k, \omega) = \delta(\omega - \xi(k))$, the one for interacting bosons is very different and displays a more complex structure. The $\omega - e_F \geq (\leq) 0$ part of $A(k, \omega)$ comes from the greater (lesser) Green's function.

Following the discussion of Lieb and Liniger in Ref. [15] for the homogeneous TG, we have identified the single-particle processes, shown in Fig. 1.12, contributing to the limiting curves in Fig. 1.11. The green solid lines in Fig. 1.11 ($e_1(k)$), called particle-like excitation, correspond to the process of exciting a particle from the highest occupied state, with momentum k_F, to a generic non-occupied state with momentum $k_F + q$ (Fig. 1.12a); the pink solid line in Fig. 1.11 ($e_2(k)$), called hole-like excitation, correspond to the process of exciting a particle from a generic occupied state with momentum $k_F - q + 2\pi/L$ to the first non-occupied state with momentum $k_F + 2\pi/L$ (Fig. 1.12b). This two curves are analogous to the ones predicted by Lieb and Liniger [15] for a homogeneous TG gas. In addition to these two curves,

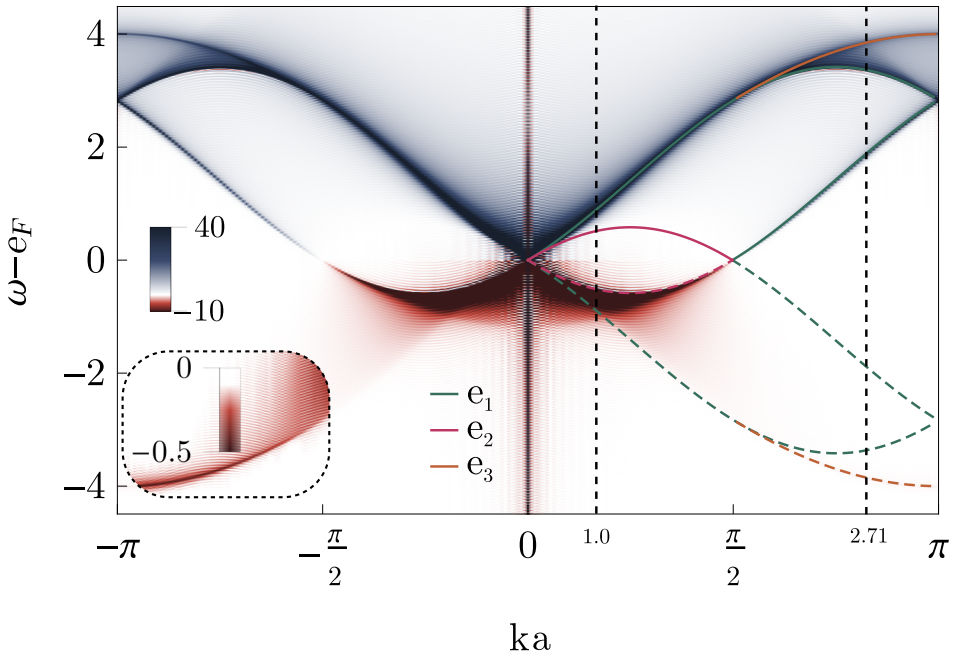

Figure 1.11: Spectral function of TG gas with 256 sites and $n_F = 64$ on a lattice. Purple, green and yellow lines are respectively $e_1(k)$, $e_2(k)$ and $e_3(k)$, that correspond to the elementary processes depicted in Fig. 1.12 and non-analyticities of the SF. It has support outside of the region between $\pm e_2(k)$ and show power law behaviour in the vicinity of the elementary curves. In order to clearly see the effect of the lattice, in the bottom-left of the picture a different color scale has been chosen, as expressed by the different legend.

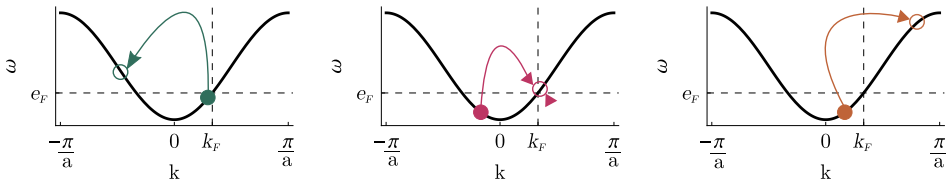

Figure 1.12: Elementary processes corresponding to limiting lines in Fig. 1.11. From left to right $e_1(k)$, $e_2(k)$, $e_3(k)$

we can appreciate a third one ($e_3(k)$) generated by the symmetric excitation of a particle from an occupied state at momentum k to a free one with momentum $\pi/a - k$ (Fig. 1.12c) and corresponding to the yellow curve in Fig. 1.11. This process is a clear signature of the presence of the lattice with the consequent flattening of the single particle dispersion relation at $k \sim \pm\pi/a$ ($\xi(k) = -2J\cos(ka)$) and which has no analogue in the homogeneous case.

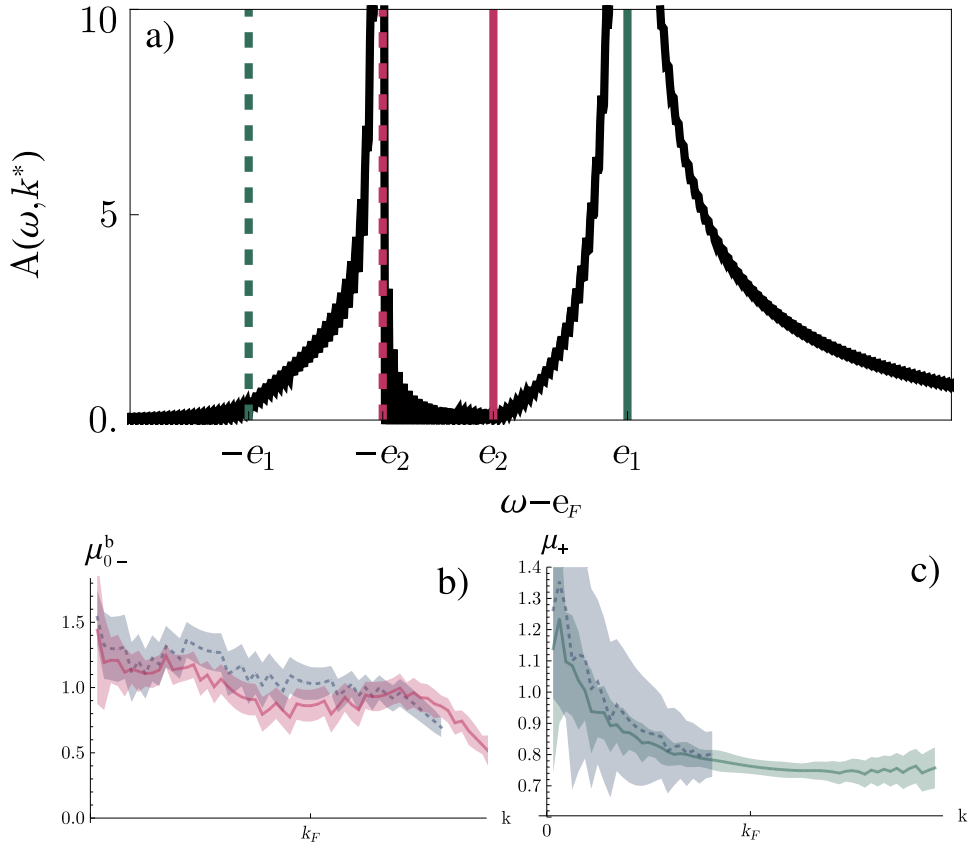

Figure 1.13: a) Cut of the SF of TG gas in a lattice (Fig. 1.11) for $k = 1.0$. It shows power law behaviour in the vicinity of each depicted line $(\pm e_1(k),\ \pm e_2(k))$. b) and c) show the power law exponent behaviour as a function of k for $\omega - e_F \to -e_2^-(k)$ b) and $\omega - e_F \to e_1^+(k)$ c) . The red and green band (solid lines) correspond to the power law exponents for the TG on a lattice while the blue bands (dashed lines) corresponds in both figures to the same coefficient for the SF of the TG in a homogeneous system.

Alike in the homogeneous system, it vanishes in the regions $|\omega - e_F| < e_2(k)$. This condition can be derived from the non-linear Luttinger liquid theory [72]. Moreover, it shows power-law divergent singularity at $\omega - e_F = -e_2(k)$ and converging non-analyticity at $\omega - e_F = e_2(k)$. Other singularities (or non analyticities) occur at $\pm e_1(k)$ and are a manifestation of the integrability of the delta-like interaction model [14, 15, 72]. This behavior can be appreciated in the cut at fixed k of the spectral function shown in Fig. 1.13a).

It is remarkable that these features, first predicted for a homogeneous system in the absence of external potential, persist also in the case of a lattice, and therefore can in principle be observed in current state of the art

experiments.

A third set of curves where the spectral function seems to show a non-analytic behavior is $\pm e_3(k)$. Once again this is peculiar of the presence of the lattice.

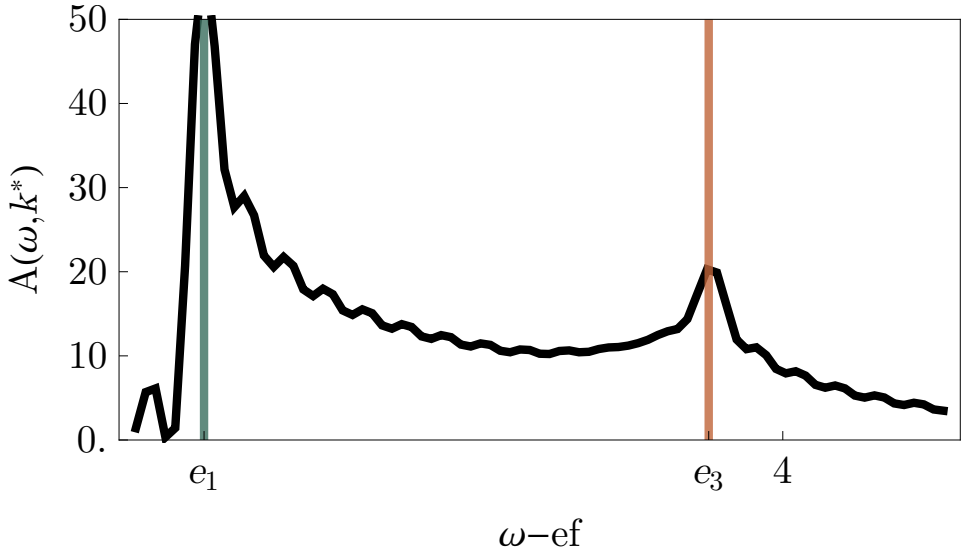

Figure 1.14: Cut of the SF of TG gas in a lattice (Fig. 1.11) for $k = 2.71$ in the vicinity of $e_3(k)$. Vertical lines correspond to $e_1(k)$ and $e_3(k)$. It shows a peak at $\omega - e_F = e_3(k)$

Because of the presence of the lattice, with the consequent boundedness of the single-particle energy spectrum, the maximum allowed energy exchange corresponds to moving a particle from the bottom to the top of the band. This implies that in a non-interacting or weak-interacting system the SF should vanish for $|\omega - e_F| > 4J$. Here, interestingly, it does not happen, as you can see in fig. 1.14, because the strong interaction, embodied in the mapping, changes this simple single-particle scenario giving rise to a finite probability for excitations with $\omega - e_F > 4J$.

1.3.2 Power-law of the spectral function

The behaviour of the spectral function near the non-analyticities has been extensively studied in Ref. [69–72] where a power-law behavior of the form $A(\omega, k(\omega)) \propto \omega^{-\mu}$ has been predicted for the Lieb-Liniger model with exponents depending upon the Luttinger parameter. Our results allow us to observe the predicted power-law behaviour near the limiting curves of the spectral function shown in Fig. 1.11.

We can therefore extract the exponents of the power-law in the presence of the lattice, and compare them with those of a homogeneous system, by

sending the lattice spacing to zero, with the prediction in Ref. [72]. In practice, we considered a system with plane waves and with a dispersion relation of the form $\omega \propto k^2$, which is typical of free-particles.

The results are shown in Fig. 1.13 b) and c). We can see that there are large fluctuations in the value of the exponent due to the closeness of different non-analyticities, expecially at small momenta. Nevertheless the power-law exponent both with and without the lattice are close for $k \sim k_F$, where the single-particle dispersion relation for the lattice is well approximated by a quadratic one (free-particle). This is true for both non-analiticities.

1.4 Conclusions

In this chapter we have studied the TG gas in periodic and quasiperiodic potentials.

In sec. 1.1 we have reviewed the mapping of the many-body wavefunction of the TG gas into that of a non-interacting Fermi gas, and extended it in order to calculate the single particle Green's function in the time domain. They allow to recover the equal time quantities, such as density (RSPDM) and momentum distribution (MD), but also to calculate the spectral function (SF), which contains informations about the elementary excitations of the system.

In sec. 1.2 we have studied the many-body ground state properties of a system of non-interacting fermions and strongly interacting bosons in a one-dimensional bichromatic potential. In the tight-binding regime, we have seen that signatures of the transition are clearly manifested in the many-body properties of both systems. Similarly, the presence of a mobility edge in the continuum changes the many-body properties of the ground state, as shown by comparing the momentum distribution for different numbers of particles in the system. If the number of particles is such that only levels below the mobility edge are filled, then the behavior of the system is similar to that in the tight-binding regime, as all occupied states suddenly localize. On the other hand, an increase in the number of particles results in the mobility edge crossing the region of the occupied states as the second potential is varied. This is clearly visible in the momentum distribution of the system and in the entropy of the reduced single particle density matrix. Moreover in the case of bosons, we have shown that the interaction plays a key role in the localization properties of the system.

Because our expressions for the lesser and greater Green's functions, presented in sec. 1.1, allow a tractable numerical approach to study the dynamics of the TG gas, we have studied in sec. 1.3 the spectral function of a TG gas in a lattice and discussed some of its features. Specifically we compared our results with previous predictions on the behavior of the spectral function and its non-analiticities for a homogeneous TG, and we

showed new features introduced by the presence of the lattice.

2

Orthogonality catastrophe and Fano resonances of a Fermi gas in a periodic potential

Chi va dicendo in giro che odio il mio lavoro
non sa con quanto amore mi dedico al tritolo,
è quasi indipendente ancora poche ore
poi gli darò la voce, il detonatore.

– Fabrizio De André, *Il bombarolo*

We explore the post-quench (time-resolved) dynamics of an ultra-cold atomic gas of fermions, trapped in a finite-size periodic potential, due to the suddenly switched-on interaction with an embedded two-level atom, excited by a fast pulse. Specifically, we look at the Loschmidt echo as a figure of merit for the response of the system and its long-time behavior, which we characterize by two complementary strategies based on the calculation of the probability amplitude that the gas retrieves its pre-quench state, namely the vacuum persistence amplitude. Accordingly, we first use a functional determinant approach, which gives an exact numerical solution for the vacuum persistence amplitude, via the Levitov formula. Then, we comparatively consider a diagrammatic perturbation approach, which employs a linked cluster expansion of the vacuum persistence amplitude, truncated to the lowest three orders. We begin by considering the gas in the metal phase, with its Fermi energy well below the upper edge of its lowest lying, valence band. In this context, we show that the second-order of the linked cluster

expansion well captures the long-time tail of the echo and its power-law behavior, being consistent with the Mahan-Noziéres-De Dominicis theory of a sudden interaction quench, weakly probing a free electron gas. The power law is a signature of the Anderson Orthogonality Catastrophe. Introduced in order to explain X-ray spectra by Hopfield and Anderson in 1967 [84], it accounts for the fact that the overlap of the ground state of a metal, after the creation of a core hole, with the unperturbed one tends to zero in the thermodynamic limit, as a negative power law of the system size ($N^{-\alpha}$), even if the single particle wavefunctions are only slightly modified by the external perturbation. Mahan, Nozieres and de Dominicis [87, 88, 115] developed the dynamical theory that leads to the power law behavior in time of the Loschmidt echo, as explained for our case in appendix 2.A.

Additionally we derive an expression for the critical exponent of the power-law decay of the metal gas and we show that it is in excellent agreement with a numerical fit obtained from the functional-determinant approach. We further show that the second-order approximation may even reasonably describe the blockade of echo decay for sufficiently weak quenches, due to the confinement of the metal gas to a finite spatial region. As the perturbation with impurity atoms gets stronger, the third-order contribution to the linked cluster expansion comes into play, accounting for particle-hole recombination processes that may have a long lifetime in the presence of a large energy gap, between the valence and first excited, conduction bands, i.e., in the tight-binding regime. Then, we move to the more fascinating scenario where the Fermi energy lies at (or above) the upper edge of the valence band, and the orthogonality catastrophe mechanism is suppressed with the gas approaching the band insulator regime. In this case, the response of the system is dominated by oscillations of increasing amplitude as the number of particles in the gas tend to completely fill the valence band. These modes, detected in the functional determinant approach, may be interpreted as Fano-like resonances yielding a characteristic peak pattern in the frequency-domain representation of the vacuum persistence amplitude, or, in the language of quantum thermodynamics, in the distribution of work. We provide evidence that this behavior is a clear manifestation of third-order effects in linked cluster expansion, which do not simply act to correct or renormalize the second-order approximation, but sheds new light on the physics of the Anderson Ortogonality Catastrophe.

2.1 Sudden quench in a trapped Fermi Gas

We consider a (monoatomic) gas of noninteracting cold fermions trapped in an optical lattice, having the form of an infinitely deep potential well of size L, which contains an oscillating, sin-squared potential $U(x) = U_0 \sin^2(kx)$ of depth U_0 and characteristic wavelength $2\pi/k$. The atoms in the trap are

described by the second-quantized (unperturbed) Hamiltonian

$$\hat{H}_0 = \int dx\ \hat{\Psi}^\dagger(x) h_0(x) \hat{\Psi}(x), \quad h_0(x) = -\frac{1}{2}\frac{d^2}{dx^2} + U(x), \tag{2.1}$$

here expressed in units of the atomic mass of the gas and the reduced Planck's constant ($\hbar = 1$, $m = 1$), where $\hat{\Psi}(x)$ denotes the fermion field in real space. The properties of $\hat{H}_0$ depend on the population the spectrum of its single-particle equivalent $\hat{h}_0$, of coordinate representation $h_0(x)$, which we diagonalized by a standard discretization technique on uniform space grids of 10^4 points [1] , to obtain the single-particle eigenstates $|n\rangle$ and corresponding eigenvalues ϵ_n. In doing so, we considered a sufficiently large potential well of length $L = 500$ and an optical wavenumber $k = \pi$, to have the minima of the lattice potential at integer coordinates and a total number of lattice sites $N_s = L$.

In the context of ultracold gases, an important role is played by the *so-called* recoil energy $E_r = k^2/2$, which represents the smallest kinetic energy transferred by the optical lattice to the trapped atoms. The interplay between the kinetic and potential energies establishes the limits of validity of the TB approximation. In particular, the ratio of the potential amplitude U_0 to the recoil energy is commonly used to define a lower threshold for this approximation, safely set at $U_0^*/E_r = 4$. Indeed, the origin of the distinction between the TB and non-TB (or CNT) regimes has to be sought in the spectrum of the single-particle Hamiltonian, which we will always assume, without loss of generality, to be populated in its lowest lying band at zero temperature. Then, the size of the first band gap, compared to the bandwidth of the first band, gives a good control of the difference between the TB and CNT cases, as shown in Fig. 2.1. In the TB regime, the first band gap is typically several order of magnitude larger than the first bandwidth [$U_0 > U_0^*$, Fig. 2.1(a)], therefore exponentially suppressing the population of the second band at low temperatures. On the other hand, in the CNT regime, the first band gap is of the same order as or smaller than the first bandwidth [$U_0 < U_0^*$, Fig. 2.1(b)], thus allowing the second band at least to come into play in the system's dynamics.

In the following we will not resort to the TB limit, but we will rather explore the range of parameters where the TB approximation is usually applied. Henceforth, we will cutoff our analysis to the lowest four bands, and we will reference to the TB limit when the condition $U_0 > U_0^*$ is satisfied.

[1] Altough the one-dimensional Schrödinger equation $h_0(x)\,\langle x|n|x|n\rangle = \epsilon_n\,\langle x|n|x|n\rangle$, admits an analytic solution in terms of the Mathieu functions, we solved it by numerical diagonalization on a uniform space grid, using an MPI-parallelized Fortran 90 code, implemented via the (GNU) ScaLAPACK libraries. We adopted a simple central-difference scheme, which we carefully checked to produce well-converged results within the range of parameters explored in our study. More specifically, we used the solution of the harmonic oscillator as a benchmark to test our code, obtaining an excellent agreement with the analytical solution, for the lowest lying ∼1000 eigenfunctions and eigenenergies.

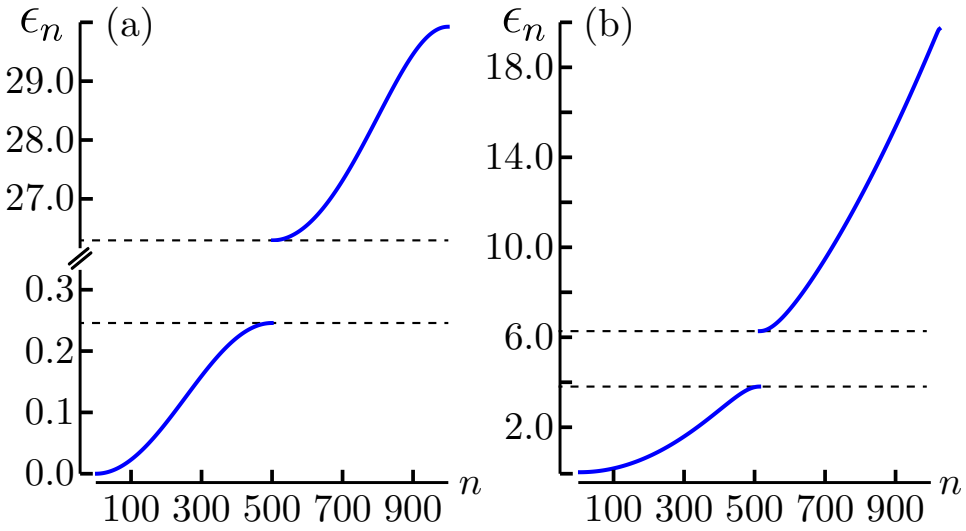

Figure 2.1: Band dispersions of a Fermi gas in the sin-squared lattice potential introduced in the text, with characteristic wavenumber $k = \pi$, confined to a size $L = 500$. The eiegnvalues ϵ_n of $h_0(x)$ [Eq.(2.1)] are plotted *vs* the eigennumber n for (a) $U_0 = 12E_r$ and (b) $U_0 = E_r$. In (a), the ratio between the first band gap and the first bandwidth is ∼106 (TB regime), whereas, in (b), the same quantity takes a value of ∼0.65 (CNT regime).

We now consider that an impurity atom of different species is immersed in our atomic gas. It has two active internal states, denoted $|g\rangle$, $|e\rangle$, and free Hamiltonian $\hat{h}_I = \sum_{i=e,g} \varepsilon_i \, |i\rangle \langle i|$. The mass of the impurity is generally selected to be much larger than the atomic mass of the gas, which can be achieved using a species-selective dipole potential with a very large frequency compared to the characteristic frequency of the trap that contains the gas. Then, the impurity motion is essentially frozen, meaning that the impurity is localized in space (infinite mass limit). We may further assume that the impurity interacts with the gas only when it lies in the excited state $|e\rangle$, with a coupling strength V_0, which can be tuned by means of a Feshbach resonance. The Hamiltonian of the composite (gas+impurity) system is given by: $\hat{H} = \hat{H}_0 + \hat{h}_I + \hat{V} \otimes |e\rangle \langle e|$.

At $t < 0$ the impurity lies in its ground, non-interacting state $|g\rangle$, with the fermions in their equilibrium configuration set by $\hat{H}_0$. Then it is abruptly excited to its interacting state $|e\rangle$, say, by a fast pulse at the time $t = 0$. The gas effectively feels a sudden localized perturbation, of the form $v(x, t) = v(x)\Theta(t)$, with Θ being the Heaviside step-function. We work in a range of temperatures where the gas is enough diluted to let us retain only the s-wave scattering component of the space potential $v(x)$, which may be taken to have the delta-function, structureless form $v(x) = V_0 k^{-1} \delta(x - x_0)$ due to the

extreme localization of the impurity atom. Thus, the impurity perturbation operator reads

$$\hat{V} = V_0 k^{-1} \hat{\Psi}^\dagger(x_0)\hat{\Psi}(x_0), \qquad t > 0, \tag{2.2}$$

and the coupling matrix elements between two eigenstates of $\hat{h}_0$ are given by

$$V_{n'n} = V_0 k^{-1} \langle n'|x_0\rangle\langle x_0|n\rangle. \tag{2.3}$$

To simplify the computational burden, we let the position of the impurity atom x_0 to coincide with a minimum of the lattice potential, at the center of the trap. In this case, only the single-particle wavefunctions $\langle x|n\rangle$ with even parity symmetry, relative to x_0, experience the interaction with the impurity, whereas $\langle x_0|n\rangle = 0$ for odd integer eigennumbers. To further proceed, we express the fermion field in terms of the annihilation operator $\hat{c}_n$ for the state $|n\rangle$, using $\hat{\Psi}(x) = \sum_n \langle x|n\rangle \hat{c}_n$. Then, the unperturbed Hamiltonian results in

$$\hat{H}_0 = \sum_n \epsilon_n \hat{c}_n^\dagger \hat{c}_n, \tag{2.4}$$

the particle number operator reads $\hat{N} = \sum_n \hat{c}_n^\dagger \hat{c}_n$, and the effect of the perturbation on the gas has the form

$$\hat{V} = \sum_{n,n'} V_{nn'} \hat{c}_n^\dagger \hat{c}_{n'}, \qquad t > 0. \tag{2.5}$$

An interesting feature of the just introduced implementation of the sudden quench, as opposed to a simply switch on of a blue detuned delta-like potential at $x = x_0$, is the possibility of reconstructing the many-body response of the Fermi gas by measuring the Ramsey signal of the two-level atom. Such a scheme, proposed in Refs. [76, 77], has also been realized experimentally using a mixture of different atomic species such as, ^{40}K/^{41}K or ^{173}Yb/^{174}Yb, immersed into ^{6}Li [116].

2.2 Loschmidt Echo

The above addressed protocol allows for a direct probing of the many-body dynamics of the Fermi gas, via its response to the sudden excitation of the impurity. A comprehensive characterization of this phenomenon is provided by the Loschmidt echo, which, in the present context, may be defined as

$$\mathcal{L}_\beta(t) = |\nu_\beta(t)|^2, \qquad t > 0, \tag{2.6}$$

where

$$\nu_\beta(t) = \left\langle e^{i\hat{H}_0 t} e^{-i\hat{H}t} \right\rangle_\beta \qquad \hat{H} = \hat{H}_0 + \hat{V} \tag{2.7}$$

represents the probability amplitude for the gas to return to its initial equilibrium state after the switching on of the perturbation, at a time $t > 0$

and inverse temperature β. In other words, the echo is a measure of the stiffness of the gas to the sudden perturbation [44, 76, 77].

Eq. (2.7) introduces a decoherence factor for the probing impurity that controls the dynamical response of a many-particle system, and is usually referred to as the *vacuum persistence amplitude,* with $\langle \cdots \rangle_\beta = \mathrm{Tr}[\cdots \hat{\rho}_0]$ denoting the grand canonical average on the unperturbed density operator $\hat{\rho}_0 = \frac{e^{-\beta(\hat{H}_0 - \mu\hat{N})}}{\mathrm{Tr}[e^{-\beta(\hat{H}_0 - \mu\hat{N})}]}$, at inverse temperature β and chemical potential μ. [2]

Its Fourier transform coincides with the absorption spectrum of the system [77], while, conventionally, the Fourier transform of its complex conjugate denotes the distribution of work in the context of quantum thermodynamics [78]. These two relations are briefly recalled in sec. 2.2.1.

As mentioned in the introductory section, we used two techniques to calculate $\mathcal{L}_\beta(t)$, namely, the FD approach by Levitov [82, 83], providing a formally exact (and computationally affordable) result for $\nu_\beta(t)$, and a many-body perturbation approach, introduced in Ref. [77], which relies on the LCE of $\nu_\beta(t)$ in connected Feynman diagrams. The comparative use of the two approaches gives an extended insight into the different processes, contributing to the global behavior of the system, and allows access to its many-body spectrum.

2.2.1 Relationship with absorption spectrum and work distribution

The frequency-domain representation of the vacuum persistence amplitude $\nu_\beta(t)$, defined via eq. (2.7), is given by the Fourier transform

$$\tilde{\nu}_\beta(\omega) = \int_{-\infty}^{\infty} \frac{dt}{2\pi} \nu_\beta(t) e^{i\omega t}, \tag{2.8}$$

which may be readily interpreted as the absorption spectrum of the Fermi gas due to the suddenly switched-on impurity potential [77].

Its relation to the Loschmidt echo is established by eq. (2.6).

An important feature of the Loschmidt echo is its relation with the so-called distribution of the work, defined as [78]:

$$P_\beta(\omega) = \sum_{i,f} P_i R_{f|i} \delta(\omega + E_i - \tilde{E}_f). \tag{2.9}$$

Here, P_i is the initial population of the many-body eigenstate $|\Psi_i\rangle$ of the unperturbed Hamiltonian $\hat{H}_0$, with energy E_i, and $R_{f|i} = |\left\langle \tilde{\Psi}_f | \Psi_i \right| \tilde{\Psi}_f | \Psi_i \rangle|^2$

[2] To calculate the chemical potential for a fixed number of particles $\langle n_F \rangle$ and for a finite β, we choose a high energy cut-off for the chemical potential μ_∞ and we evaluate iteratively a temporary number of particles $n_t = \sum_i [1 + e^{\beta(\epsilon_n - \mu_\infty)}]^{-1}$ by increasing or decreasing μ_∞ of an arbitrary small amount $\delta\mu$. When the difference between temporary and fixed number of particle reaches an imposed small error $|n_t - \langle n_F \rangle| \simeq 10^{-14}$, we stop the process and we end up with $\mu(n_F, \beta)$

is the conditional probability for the system to be found in the eigenstate $\left|\tilde{\Psi}_f\right\rangle$ of the perturbed Hamiltonian $\hat{H}$ [Eq. (2.7)], with energy $\tilde{E}_f$. Eq. (2.9) explores the non-equilibrium thermodynamics of the system, being at the same time closely related to the vacuum persistence amplitude, via [76–78,117]

$$\nu_\beta^*(t) = \int \mathrm{d}\omega P_\beta(\omega) e^{i\omega t}, \tag{2.10}$$

which makes the dynamic content of the work distribution equivalent to that of the absorption spectrum

$$\mathcal{L}_\beta(t) = \left| \int \mathrm{d}\omega P_\beta(\omega) e^{i\omega t} \right|^2. \tag{2.11}$$

2.2.2 Functional Determinant Approach

The Levitov FD approach gives an exact numerical solution for the vacuum persistence amplitude, reducing the gand-canonical average in Eq. (2.7) to a sum of single-particle determinants, in virtue of the general relation [82, 83]:

$$\left\langle e^{\hat{X}_i t} \dots e^{\hat{X}_N t} \right\rangle_\beta = \mathrm{Det}\left[\hat{n}_- + \hat{n}_+ e^{\hat{x}_i t} \dots e^{\hat{x}_N t}\right]. \tag{2.12}$$

Here, the $\hat{X}_i$'s are one-body operators, each of them being associated with a single-particle representative $\hat{x}_i$, and $\hat{n}_\pm = \left[1 + e^{\pm\beta(\hat{h}_0 - \mu)}\right]^{-1}$ may be interpreted as a first-quantized particle-hole operator, whose eigenvalues coincide with the particle-hole occupations $f_n^\pm = [1 + e^{\pm\beta(\epsilon_n - \mu)}]^{-1}$.

By Eq. (2.12), the two exponential operators in Eq. (2.7) are, respectively, mapped to $e^{-i\hat{h}_0 t}$ and $e^{i\hat{h}t}$, where $\hat{h}$ is the perturbed single-particle hamiltonian, of coordinate representation $h(x) = h_0(x) + v(x)$, associated with $\hat{H}$. Accordingly, we obtain

$$\nu_\beta(t) = \mathrm{Det}\left[\hat{n}_- + \hat{n}_+ e^{-i\hat{h}_0 t} e^{i\hat{h}t}\right]. \tag{2.13}$$

To implement Eq. (2.13), we computed the perturbed eigensystem ($|\tilde{n}\rangle$,$\epsilon_{\tilde{n}}$) of $\hat{h}$ with the same discretization scheme used for the unperturbed eigensystem ($|n\rangle$,ϵ_n) of $\hat{h}_0$. Then, we calculated the change-of-basis matrix elements $\langle n|\tilde{n}\rangle$ and obtained the vacuum persistence amplitude as the single-particle determinant

$$\begin{aligned} &\nu_\beta(t) = \mathrm{Det}\left[S_\beta(t)\right], \quad \text{where} \\ &\left[S_\beta(t)\right]_{nn'} = f_n^- \delta_{nn'} + \sum_{\tilde{n}} f_n^+ e^{i\epsilon_n t} \langle n|\tilde{n}\rangle e^{-i\epsilon_{\tilde{n}} t} \langle \tilde{n}|n'\rangle. \end{aligned} \tag{2.14}$$

Working with sufficiently small impurity perturbations, being such that $V_0 k^{-1}/U_0 = 10^{-1}$-10^{-3}, we used the one-to-one correspondence between the unperturbed bands of $\hat{h}_0$ and the perturbed bands and $\hat{h}$ to truncate the matrix elements in Eq. (2.14) to the lowest four bands, which we verified to produce well converged results.

2.2.3 Linked Cluster Expansion Approach

As it is customary in diagrammatic perturbation theory, we can introduce the perturbation operator $\tilde{V}(t) = e^{i\hat{H}_0 t}\hat{V}e^{-i\hat{H}_0 t}$ to transform Eq. (2.7) in the interaction picture, obtaining

$$\nu_\beta(t) = \left\langle \mathcal{T} e^{-i\int_0^t d\tau \tilde{V}(\tau)} \right\rangle_\beta , \tag{2.15}$$

where $\mathcal{T}$ is the Dyson time-ordered operator.

Then, we can invoke the LCE theorem [118,119] (see also Appendix 2.A for a brief recall of its derivation), which amounts to reducing the grand-canonical average of the time-ordered exponential operator in Eq. (2.15) to an exponential sum of connected Feynman diagrams

$$\nu_\beta(t) = e^{\sum_{l=1}^{\infty} \Lambda_l^\beta(t)} . \tag{2.16}$$

Here, $\Lambda_l^\beta(t)$ denotes the l-vertex loop

$$\begin{aligned}\Lambda_l^\beta(t) =& \frac{(-1)^l}{l!} \sum_{n_1,\dots,n_l} \int_0^t dt_1 \dots \int_0^t dt_l G^0_{n_1}(t_1 - t_2) \\ & \times V_{n_1 n_2} G^0_{n_2}(t_2 - t_3) V_{n_2 n_3} \dots G^0_{n_l}(t_l - t_1) V_{n_l n_1},\end{aligned} \tag{2.17}$$

connected by the unperturbed single-particle propagators

$$G^0_n(t) = -i \left\langle \mathcal{T} \hat{c}_n(t) \hat{c}_n^\dagger(0) \right\rangle_\beta = -i \left[\Theta(t) f_n^- - \Theta(-t) f_n^+ \right] e^{-i\epsilon_n t} \delta_{nn'} . \tag{2.18}$$

In the following, we extend the results from previous studies [77,78], where a more simple form of the trapping potential was adopted, and provide an analysis of the lowest three orders of the LCE, reported in Appendices 2.A.1 and 2.A.2. To implement this part, we separately computed the explicit expressions for $\Lambda_1^\beta(t)$ [Eq. (2.31)], $\Lambda_2^\beta(t)$ [Eq. (2.33)] and $\Lambda_3^\beta(t)$ [Eq. (2.47)] with the unperturbed eigensystem $(|n\rangle, \epsilon_n)$ of $\hat{h}_0$. In doing so, we truncated the unperturbed spectrum to the lowest four bands, which we verified to be a well-converged approximation.

2.3 Long-time dynamics and finite-size effects in the metal phase

We consider the gas to be in a metal phase, with the chemical potential (Fermi level at zero temperature) positioned well below the upper edge of its lowest lying (valence) band. In the limiting case of an infinitely extended trap, the decay of the vacuum persistence amplitude, and therefore of the echo, is a power-law at long-time, governed by the AOC mechanism. This

behavior is strictly followed on arbitrary large time scales, as it has been proved for a Fermi gas in a harmonic-oscillator potential [77–79].

The more realistic scenario presented here allows for a true confinement of the atomic particles to a finite-length range, hence, the decay of the echo is asymptotically blocked in favor of a stationary, oscillating behavior, which produces a sequence of very low-frequency peaks in the absorption spectrum of the system. In general, the presence of these oscillations is unwanted, with the main focus being on long-time phenomena (such as the AOC) for large systems (in the thermodynamic sense).

As we document in the following, both the AOC decay and its blockade are clearly distinguished in the long-time dynamics of echo at sufficiently low temperature, being such that the chemical potential lies in the valence band. Furthermore the FD approach [Eqs. (2.12) and (2.14)] appears in good agrement with the second-order LCE approach [Eqs. (2.16) and (2.17)] in a well defined range of weak impurity perturbations.

However, as the strength of the quench increases, the third-order contribution to the LCE need to be included to adequately describe the behavior of the echo beyond the AOC range. This, in turns, implies that, unlike previous derivations, a third-order expansion of the vacuum persistence amplitude is a necessary requirement to have full access to the whole response of the gas, including the effect of its finite extension.

2.3.1 Power-law decay and AOC

We begin with an analysis of the long- (non-infinite-) time decay of the echo, by comparing the FD response with the LCE approach truncated at the second-order, yielding $\ln[\nu_\beta(t)] \approx \Lambda_1^\beta(t) + \Lambda_2^\beta(t)$. The latter provides three contributions, detailed in Appendix 2.A.1, namely, a shift $\Lambda_1^\beta(t) + \Lambda_{2S}^\beta(t)$ [Eqs. (2.31) and (2.35)], a Gaussian damping $\Lambda_{2G}^\beta(t)$ [Eq. (2.34)] and an oscillating term $\Lambda_{2P}^\beta(t)$ [Eq. (2.36)]. At zero temperature, the chemical potential μ coincides with the Fermi energy ϵ_{n_F}, equivalent to n_F+1 particles populating the gas. Accordingly, the stepwise nature of the occupation factors $f_n^\pm$ cancels the Gaussian damping: $\Lambda_{2G}^\infty(t) = 0$. The long-time behavior of the echo is therefore embodied in the oscillating contribution $\Lambda_{2P}^\beta(t)$, scaling as $-\alpha \ln t$ and providing the power-law decay $\mathcal{L}_\infty(t) \propto t^{-2\alpha}$. This decay, derived in Appendix 2.A.1 by two different cutoff methods [Eqs. (2.42) and (2.44)], matches the long-time response of a free electron gas following a weak interaction quench, due to the sudden creation of a deep core hole. It is, then, a clear signature of the AOC [84, 85], as predicted by the Mahan-Noziéres-De Dominicis (MND) theory [87, 88, 115, 120]. In our case the exponent of the power-law reads

$$\alpha = \frac{|V_{n_F n_F}|^2}{2} g(\epsilon_{n_F})^2, \tag{2.19}$$

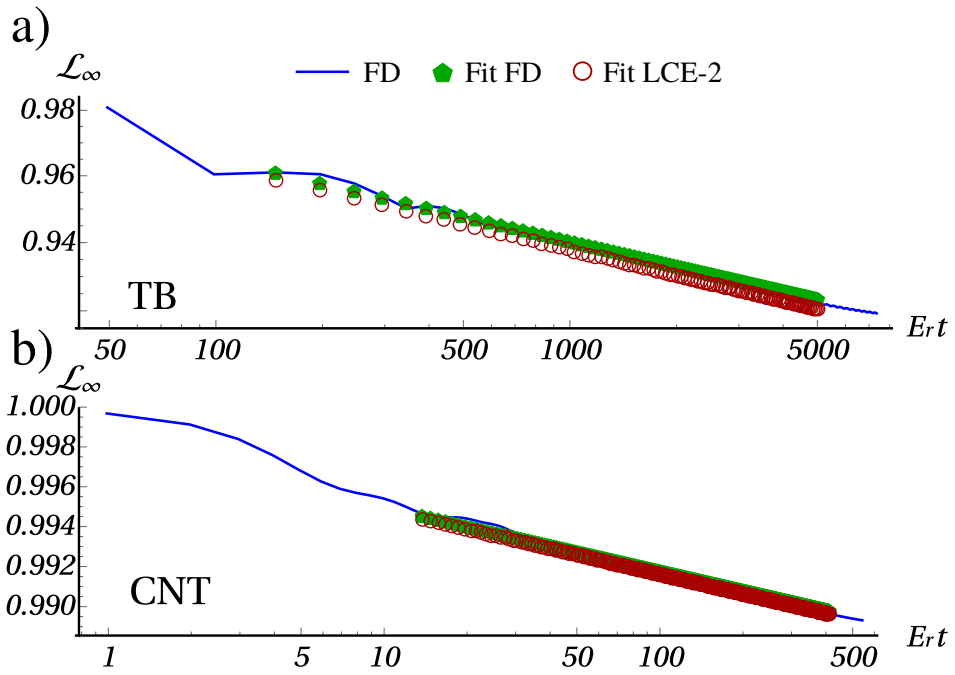

Figure 2.2: Loschmidt echo at zero temperature for a quenched Fermi gas in a sin-squared lattice potential confined to $N_s = 500$ sites, with characteristic wavenumber $k = \pi$ and filling number $n_F = 251$. The lattice potential amplitude spans from the TB [$U_0 = 12E_r$, a)] to the CNT [$U_0 = E_r$, b)] regimes, with the suddenly switched-on impurity potential having a strength V_0 of a) 10^{-2} and b) 10^{-1} for the TB and CNT case respectively. The results obtained from the FD approach of Eq. (2.14) (blue lines) exhibit a long-time, power-law decay (green dots), being consistent the LCE approach of Eq. (2.16), truncated to the second order (red circles).

where $V_{n_F n_F}$ is the impurity induced perturbation, defined in Eq. (2.3), and $g(\epsilon_{n_F})$ the density of states (DOS) at ϵ_{n_F}. Here, we should point out that the factor of $1/2$ comes from the fact that only half of the single-particle unperturbed spectrum may be excited by the impurity potential. An example of power-law decay of $\mathcal{L}_\infty$, reflecting the AOC [84, 85], is reported in Fig.2.2, where we plot the echo obtained by both the FD and second order of the LCE approaches at half-filling, on a sufficiently large time-scale ($20 \lesssim \epsilon_{n_F} t \lesssim 500$), with a choice of parameters suitable for the TB and CNT regimes.

Interestingly enough, it is commonly found in the literature that the exponent α results from a sum over the phase-shifts of the impurity potential [88,121–123]. Eq. (2.19) provides a complementary expression suitable for s-wave-like weak perturbations [119,124], which, perhaps, makes the physical meaning of this quantity more transparent. This relation tells us that the

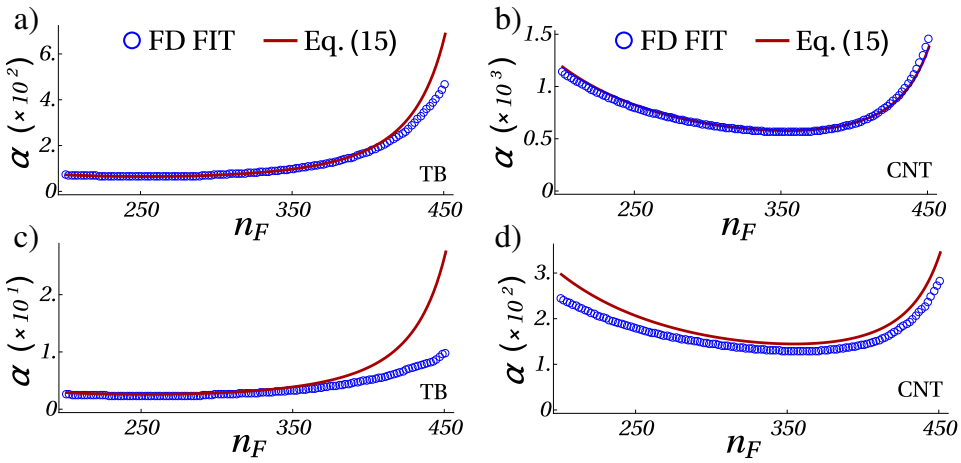

Figure 2.3: Power-law exponent 2α of the echo at zero temperature vs the Fermi number n_F in the TB [$U_0 = 12E_r$, a) and c)] and CNT [$U_0 = E_r$, b) and d)] cases for different amplitude $V_0 k^{-1}$: a) $V_0 k^{-1} = 4 \times 10^{-2} E_r$ and c) $V_0 k^{-1} = 2 \times 10^{-1} E_r$, and b) $V_0 k^{-1} = 4 \times 10^{-1} E_r$ and d) $V_0 k^{-1} = 2 \times 10^{-1} E_r$. Comparison is made between the MND-like form of Eq. (2.19) (red lines), derived from the two-vertex loop of the LCE, and the power index extracted from a fit of the long-time decay given by the FD approach (blue circles). All other parameters are as in Fig. 2.2.

decay of the echo depends upon two different and, apparently, unrelated factors. On one hand, it relies on the external perturbation, through its (typical) strength $|V_{n_F n_F}|^2$ at the Fermi energy. On the other hand, it is controlled by the availability of occupied and empty states around the Fermi energy, which goes to the squared DOS $g(\epsilon_{n_F})^2$ in the limit of zero energy exchange. Then, α is to be considered as a figure of merit of the strength of the many-body perturbation.

Figure 2.3 shows the MND critical exponent, computed by Eq. (2.19) (red solid line) as function of the Fermi number n_F in the CNT [Fig. 2.3(a)] and TB [Fig. 2.3(b)] limits. Such a quantity is in good agreement with the exponent of the power-law decay of $\mathcal{L}_\infty$, as obtained from a fit of the Loschmidt Echo of the FD approach (blue dots) with $t^{-2\alpha}$. As $|V_{n_F n_F}|^2$ does not change appreciably with n_F, the leading term in the exponent α is given by the DOS of the system $g(\epsilon_{n_F})$. The role of the DOS is particularly emphasized in the TB regime when the filling gets close to the first-band edge, which corresponds to a steep increase in the DOS due to the flattening of the spectrum. This is a fingerprint of the presence of a lattice, which has no counterpart in the free fermion unperturbed model of the original MND theory. The same feature is also present, although less pronounced, in the CNT regime.

We now discuss the effect of finite temperature, with the gas keeping its

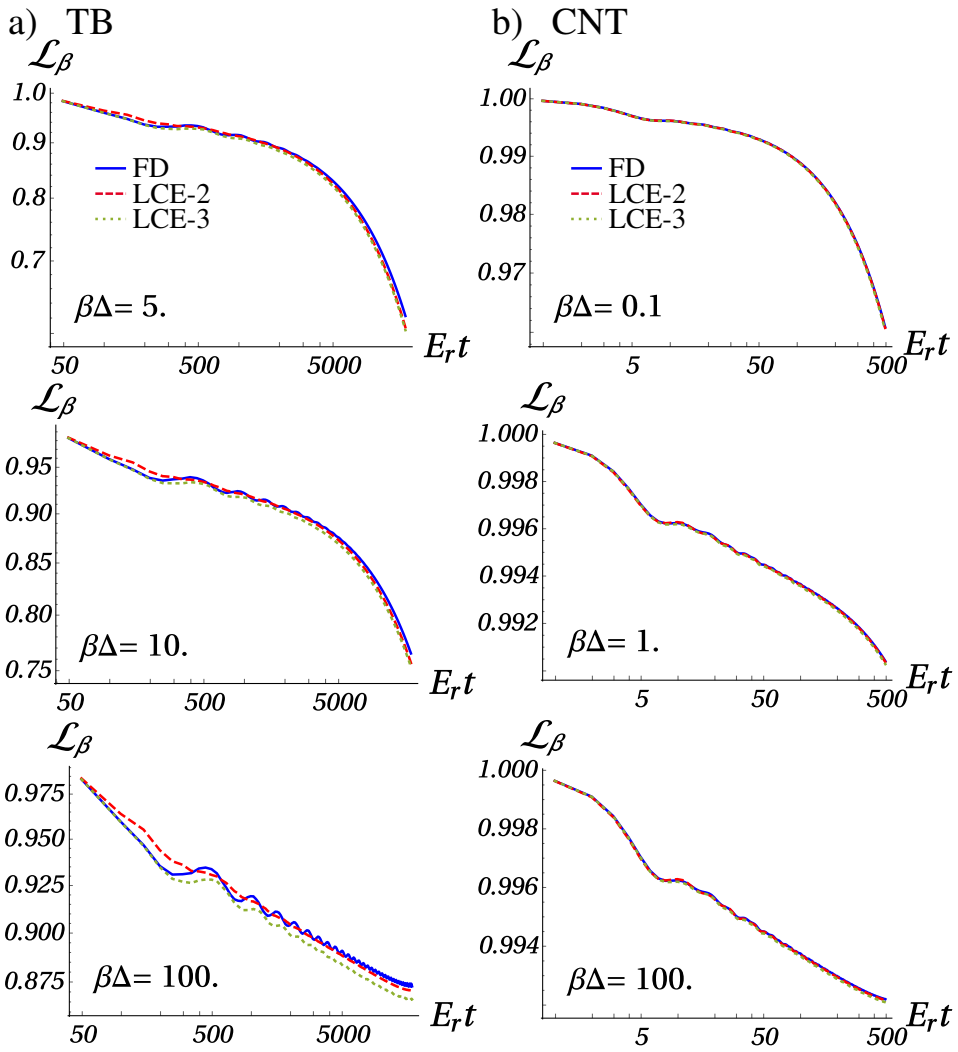

Figure 2.4: Loschmidt echo $\mathcal{L}_\beta(t)$ for a quenched Fermi gas with $N = 351$ fermions confined to the size $L = 500$, at different inverse temperatures β, given in units of first band gap Δ, a) in the TB [$U_0 = 12E_r$, $\Delta{\sim}26.7$, $V_0 k^{-1} = 4 \times 10^{-2} E_r$] and b) CNT [$U_0 = E_r$, $\Delta{\sim}2.5$, $V_0 k^{-1} = 4 \times 10^{-1} E_r$] regimes.

metallic behavior, i.e., with the chemical potential lying below the upper edge of its first valence band. This can be achieved by keeping the ratio of the total particle number N to the total lattice sites N_s well below unity. Accordingly, an increase in temperature of the initial state results in a smearing of the power-law singularity of the echo, with the occupation factors $f_n^{\pm}$ becoming smoother around ϵ_{n_F}. In particular, when only a few states above ϵ_{n_F} are non-negligibly occupied, one recovers the usual broadening induced by particle-hole excitations around Fermi, due to the Gaussian damping term

$\Lambda^{\beta}_{2G}(t)$ [Eq. (2.34)]. This is reported in Fig. 2.4, where we show $\mathcal{L}_{\beta}(t)$ for a fermion density $N/L{\sim}3/5$ and different initial inverse temperatures β, defined in units of the first band gap Δ. We see that TB and CNT regimes display similar trends within the chosen values of $\beta\Delta$, exhibiting a dominant Gaussian decay behavior for $\beta\Delta \ll 1$. The power-law decay is recovered at low temperatures, with crossing points at about $\beta\Delta{\sim}1000$ and $\beta\Delta{\sim}100$ for the CNT and TB cases, respectively.

2.3.2 Finite size effects

We have just seen and discussed the power-law decay of the echo at sufficiently long times, being such that $20{\lesssim}\epsilon_{n_F}t{\lesssim}500$. On the other hand, for $\epsilon_{n_F}t{\gtrsim}1000$, we observe a pattern of non-decaying *revivals* of the initial normalization peak, which are in striking disagreement with the AOC mechanism. This behavior is shown in Fig. 2.5, where the echo, computed from the FD approach, appears to be still in excellent agreement with the LCE approach, truncated to the second order. The revival times, having a non-trivial dependence upon the Fermi energy, correspond to low-frequency modes, of the order the average energy difference between two contiguous eigenvalues of the valence band. They are more clearly observed at zero temperature, where Gaussian damping effects are absent. Further inspection reveals that the revivals occur at increasing times $t^{*}_{n} = n\pi/(\epsilon_{n_F+1} - \epsilon_{n_F})$ with n a positive integer.

We may conclude that, either in the TB or in the CNT regimes, the non-AOC features are an unavoidable consequence of the discretization of the single-particle energy spectrum, induced by the finite extent of the system, i.e., by the confining length-range L. As mentioned in the introduction of this section, the post-quench decay behavior is therefore *blocked* by the finite size of the trap. To support this observation, in Fig. 2.6 we see how the behavior of $\mathcal{L}_{\infty}$ changes with increasing L, i.e., the number of lattice sites N_s. In particular, we observe that the time after which the non-AOC evolution begins, or the first revival time, increases with increasing the system size, becoming infinitely large ($t^{*}_{1} \to \infty$) in the thermodynamic ($L \to \infty$) limit.

2.4 Beyond the orthogonality catastrophe

2.4.1 Non-trivial third order contributions

We have shown that the second order contribution of the LCE describes well the power-law decay and captures the main features of it. On the other hand we observed the appearence of the large-amplitude and long-life time oscillations as the chemical potential (filling) of the system is increased. We show this effect in Fig. 2.7 where we plot the echo as obtained from the FD, the LCE2 and LCE3 both in for Fig. 2.7 a) the TB and Fig. 2.7 b) CNT case.

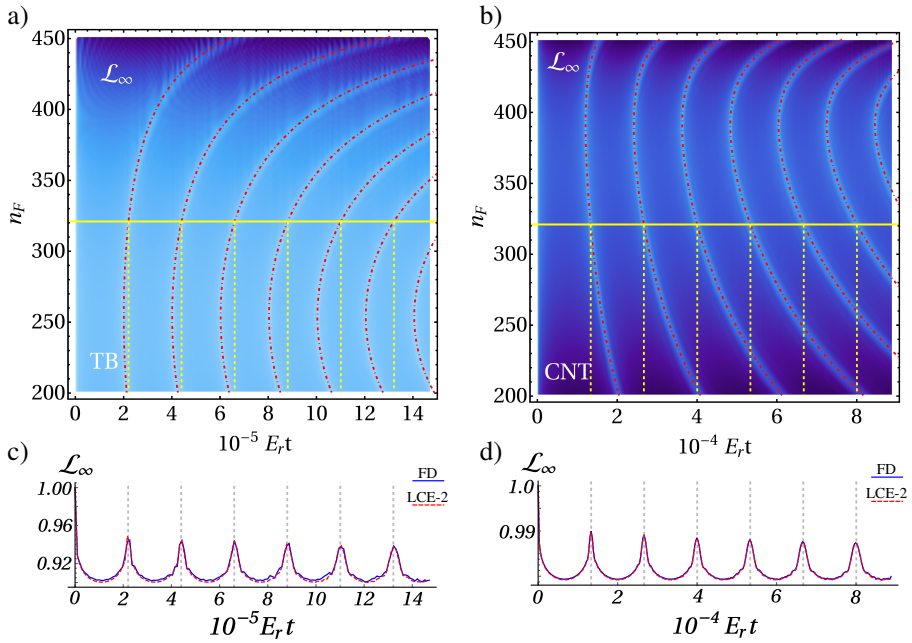

Figure 2.5: Loschmidt echo for the quenched Fermi gas ($L = 500$, $k = \pi$) at zero temperature *vs* the filling number n_F and the time t. Figures show the TB ($U_0 = 12E_r$, $V_0 k^{-1} = 4 \times 10^{-2} E_r$) [a), c)] and CNT ($U_0 = E_r$, $V_0 k^{-1} = 4 \times 10^{-1} E_r$) [b), d)] regimes. The density plots of (a) and (b) are obtained from the FD approach, with the red dashed lines designating the revival times t_n^* as function of n_F. The simple plots of (c) and (d) are computed by fixing $n_F = 351$ with both the FD approach and the LCE, truncated at the second order (LCE-2).

The LCE3 $\Lambda_3^\beta(t)$ has been calculated similarly to what we have done for the two-vertex loop $\Lambda_2^\beta(t)$ [Eq. (2.33) in Appendix. 2.A.1]. The details of the calculation are reported in Appendix 2.A.2. It is possible to reorganize $\Lambda_3^\beta(t)$ into three main contributions [Eqs. (2.51)], namely a Gaussian damping $\Lambda_{3G}^\beta(t)$ [Eq. (2.52)], a shift $\Lambda_{3S}^\beta(t)$ [Eq. (2.54)] and an oscillating term $\Lambda_{3P}^\beta(t)$ [Eq. (2.54)], plus a correlation term $\Lambda_{3C}^\beta(t)$ [Eq. (2.57)] that accounts for a finite-temperature asymmetric broadening of the work distribution. We see from Fig 2.7 that the second order contribution (LCE2) alone fails to capture the oscillations which are clearly visible in the FD approach for both the TB and the CNT case. On the other hand the third order one shows the presence of similar oscilations althought with slightly different frequency and amplitude.

In the next section we discuss the physical origin of these oscillations identifying the terms in the third order contibution which are given, as we shall see, to the finiteness of the band and represent an interesting case where

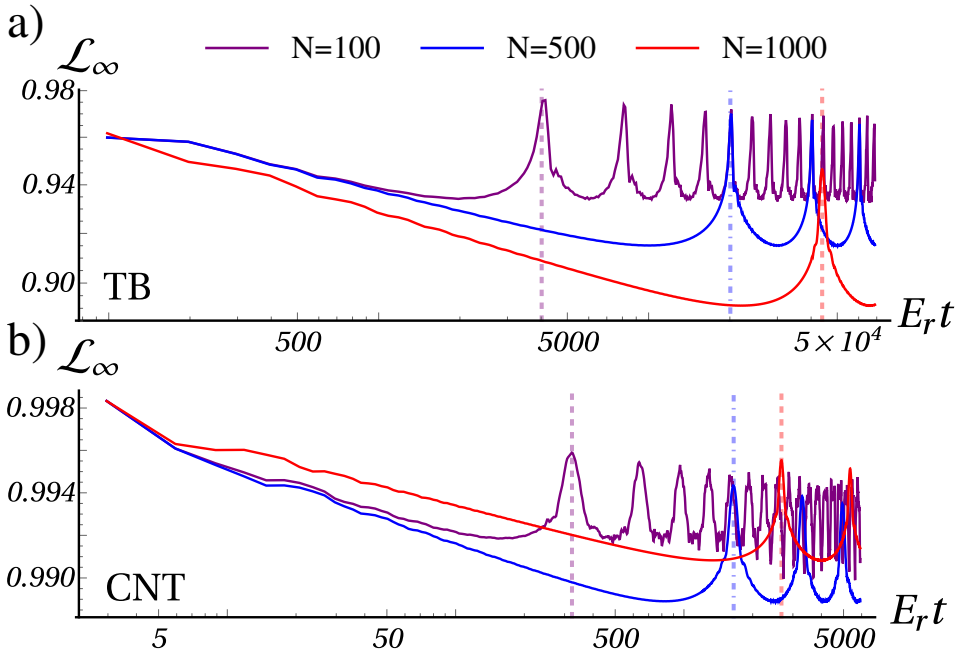

Figure 2.6: Loschmidt echo for the quenched Fermi gas at zero temperature, obtained with the LCE approach, truncated to the second order. Different values of the system-size, namely, $L = 100$ (purple), 500 (blue) and 1000 (red) have been simulated on a discretization grid with uniform spacing L/N and constant filling number N/N_s. In both a) the TB [$U_0 = 12E_r$, $V_0 k^{-1} = 4 \times 10^{-2} E_r$] and b) CNT [$U_0 = E_r$, $V_0 k^{-1} = 4 \times 10^{-1} E_r$] regimes, the revival times tend to be infinitely large in the thermodynamic limit, i.e., $t_n^* \to \infty$ for $L \to \infty$.

the third order contibution are not merely a renormalization of the LCE2 but introduce new, and non-trivial, physical effects.

2.4.2 Fano Resonances at the band edge

The occurrence of the AOC has been so far related to two main features of the system. On one hand the availability of a continuum of single particle states, which couple when the system is perturbed and brought out-of-equilibrium. On the other hand, the persistence of the metal phase during the out-of-equilibrium dynamics, with the chemical potential μ lying well inside the occupied band and plenty of hole states accessible above the Fermi energy. The continuum nature of the spectrum has been used in the derivation of the critical exponent α (see Appendix 2.A.1) to establish an MND-like power-law decay [87, 88] suitable for metallic bands, under the assumption that, in the thermodynamic limit, the amount of energy exchanges around the Fermi

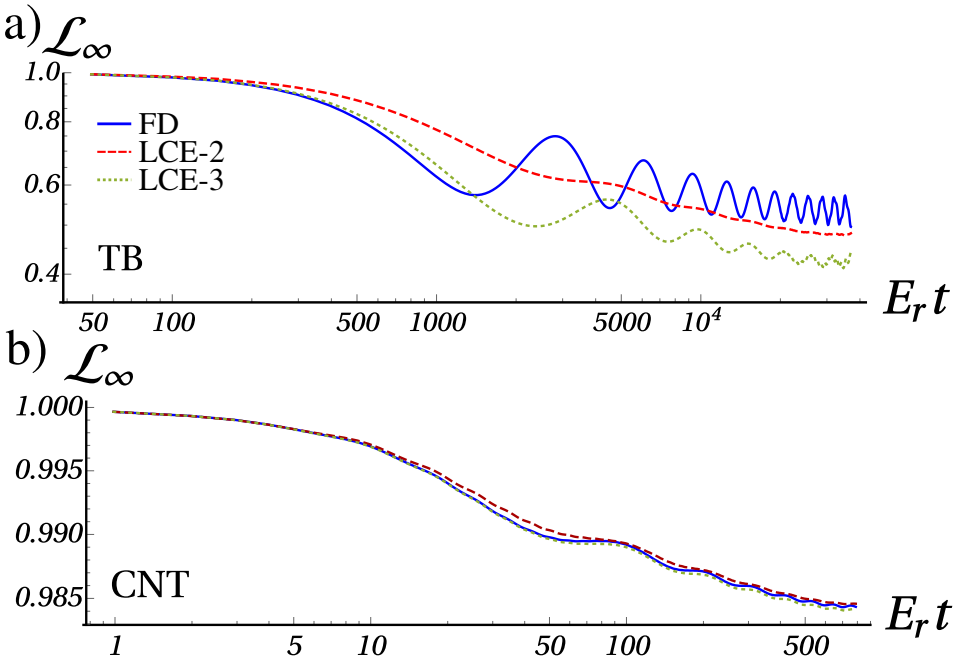

Figure 2.7: Loschmidt echo $\mathcal{L}_\beta(t)$ for a quenched Fermi gas with $N = 451$ fermions confined to the size $L = 500$, at inverse temperatures β, given in units of first band gap Δ, a) in the TB [$U_0 = 12E_r$, $\beta\Delta = 10^6$, $V_0 k^{-1} = 4 \times 10^{-2} E_r$] and b) CNT [$U_0 = E_r$, $\beta\Delta = 10^6$, $V_0 k^{-1} 4 \times 10^{-1} E_r$] regimes.

energy can go continuously to zero.

Much more intriguing is the scenario where we let the chemical potential lie close to the upper band edge or fall inside the first band gap, i.e. when the metal gas approaches the transition towards a semiconductor or an insulator, that we will detail in the following. The consequences of this change of phase are much more significant in the TB limit, where the first band gap is substantially larger than any other energy scale into play and the gas experiences a metal-to-insulator transition, characterized by vanishingly small values of the particles' mobility. On the other hand, in most CNT cases, such as the one discussed here, the gas behaves as a small-gap semiconductor and the chemical potential can be easily tuned to the second band by small temperature changes.

In the context of the TB regime, we can markedly distinguish two mechanisms, which are strongly sensitive to the temperature of the gas and characterize its change of phase. The first is related to the appearance of coherent oscillations in the echo, with the chemical potential approaching the band-edge from the metal side. The second is a freezing of the echo at values of the order of unity, as chemical potential crosses the upper band edge and falls into the first band gap. The latter is a direct manifestation of

the insulating nature of the system, with low-lying particle-hole excitations being suppressed in the absence of accessible holes states.

Figure 2.8 a) shows the two mechanism following an increase in particle number of the gas, that let the chemical potential cross the upper band edge. Working in the TB limit ($U_0 = 12E_r$, $L = 500$ and $V_0 k^{-1} = 4 \times 10^{-2} E_r$) at a reasonably small temperature, equivalent to a thermal energy $\beta\Delta$ of 10^4 in units of the first band gap, we see that the amplitude of the oscillations of the echo increases [$N < 481$, Fig. 2.8 b)], as the chemical potential increases from the metal phase. Once the insulator phase is reached, for a number $N = 481$ of atomic particles [Fig. 2.8 c) (green solid line)], the oscillations persist for large times. Conversely, after the transition point [$N > 481$, Fig. 2.8 c)], the dynamics of echo is frozen, i.e., the echo does not decay, as it is expected in the insulating phase.

The appearance of long living oscillations in the echo are a fingerprint of coherence in time, developed inside the system, which contrasts with the monotonic decay expected by the AOC at large times. These oscillations would be present also when the chemical potential is well inside the band, but they are readily suppressed by the coupling of particle-hole excitations to the background of a continuum of particle and holes. When the chemical potential approaches the band edge, the particle-hole excitations acquire a finite lifetime due to the reduction of the number of available states for these excitations to decay into.

A deeper insight into the nature of these excitations is highlighted by looking at the Fourier transform of the (complex conjugate) of the vacuum persistence amplitude, i.e., the distribution of the work $P_\beta(W)$ (sec. 2.2.1). In Fig. 2.9 we show $P_\beta(W)$ for the same system as in Fig. 2.8 at two different temperatures, corresponding to $\beta\Delta = \times 10^6$ [Fig. 2.9 a) and c)] and $\beta\Delta = 10^4$ [Fig. 2.9 b) and d)], and increasing particle numbers towards the transition point. Besides the primary peak, representing a global energy shift due to the perturbation, we detect a secondary structure, magnified in the insets, with a Fano resonance lineshape. As such, we expect it to arise from the coupling of a bound state to the continuum (almost completely filled) of states of the spectrum. In order to understand the physics behind this process, and confirm that we are looking at a Fano resonance, we analyze the three-vertex loop $\Lambda_3^\beta(t)$ of the LCE. We have already seen in Sec. 2.4.1 that the third order contribution can be recast into a sum of three different contributions similarly to the second order one. The non-trivial content of the dynamics of the gas is provided by $\Lambda_{3P}^\beta(t)$, which includes impurity induced particle-hole excitations, via $\Lambda_{3P_I}^\beta(t)$ [Eq. (2.55)], and particle-hole or hole-particle transitions assisted by particle-hole recombination processes, via $\Lambda_{3P_{II}}^\beta(t)$ [Eq. (2.56)]. While $\Lambda_{3P_I}^\beta(t)$ mostly contributes to renormalize the shake-up term $\Lambda_{2P}^\beta(t)$, $\Lambda_{3P_{II}}^\beta(t)$ has no counterpart in the LCE, and indeed represents an interaction of a *quasibound* particle-hole state with a

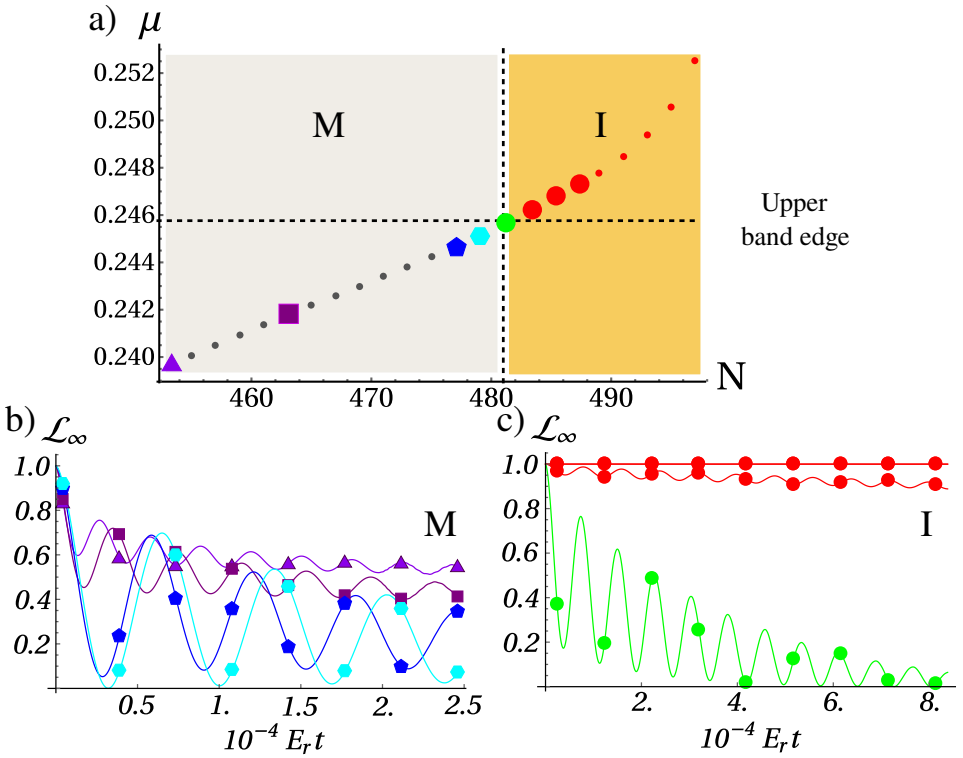

Figure 2.8: Quenched Fermi gas ($L = 500$, $k = \pi$, $V_0 k^{-1} = 4 \times 10^{-2} E_r$) in the TB limit ($U_0 = 12 E_r$) with N =453-497 atomic particles at an inverse temperature $\beta\Delta = 10^4$ in units of the first band gap $\Delta{\sim}5,41 E_r$. a) The chemical potential μ of the system increases with increasing N, crossing the upper limit of the valence band edge at $N = 481$, where a metal-to-insulator transition occurs. Correspondingly, the Loschmidt echo (calculated with the FD approach) has an oscillating behavior in the metal (M) phase b), with the amplitude of the oscillations increasing with increasing N below the complete filling number $N = 481$ c). In the insulator (I) phase c) the echo is approximately constant for very large times.

continuum.

We expect the position of the Fano resonance structures to be given by the typical energy of this *quasibound* state which is made of a particle-hole pair. The energy of such a state will be given, in first approximation, by the difference between the energy of the hole and that of the particle of which it is composed. Due to the divergency of the density of states at the band edge a hole has on average a typical enegy of ϵ_L, where ϵ_L is the energy of the highest particle state in the metal band. On the other hand to transfer a particle to/from the gas to this *quasibound* state an energy equal to the chemical potential is involved. Therefore we expect such a state to have an energy of $\epsilon_L - \mu$. Figure 2.10 shows the position of these structures, relative

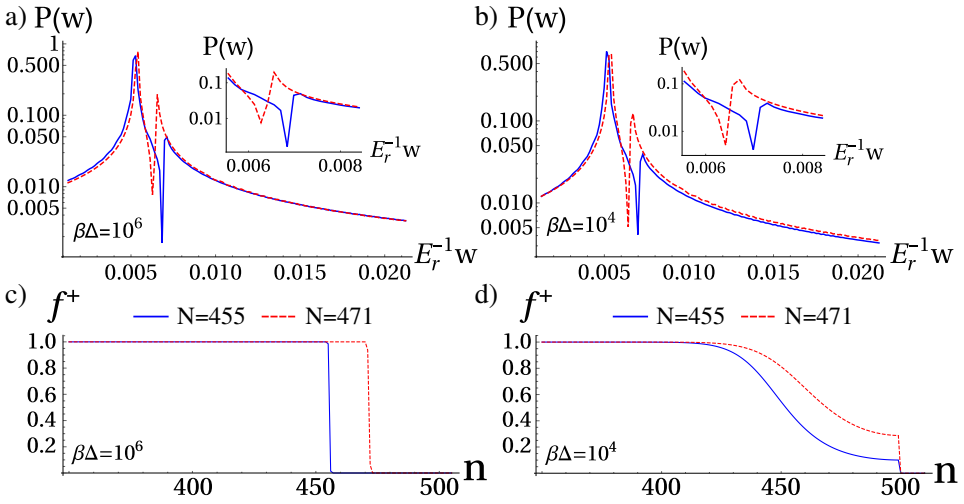

Figure 2.9: Work distributions [a), b)] and corresponding particle occupations [c), d)] for a quenched Fermi gas ($L = 500$, $k = \pi$, $V_0 = 2 \times 10^{-3}$) in the TB limit ($U_0 = E_r$) with N =463 (solid blue) and 471 (dashed red) atomic particles at the inverse temperatures $\beta\Delta = 10^6$ [a),c)] $\beta\Delta = 10^4$ [b),d)] in units of the first band gap $\Delta \sim 5,41 E_r$.

to the main peak of the work distribution, for different particle numbers, as obtained from the FD approach (blue squares) and LCE, truncated to the third-order (red disks). All the other parameters of the Fermi gas and the quench are as in Fig. 2.9. The other set of data (purple triangles) are given by $\epsilon_L - \mu$. We see that our interpretation for the energy of the *quasibound* state at the single particle level, well matches the results obtained from the LCE3 at both zero [Fig. 2.9 a) and c)] and finite temperature [Fig. 2.9 b) and d)]. The result is also qualitatively in good agreement with the result obtained from the FD approch up to a renormalization of the energy which depends upon the chemical potential (number of particles). We have checked (not shown) that the central peak in both the FD and the LCE3 is at the same position up to a discrepancy of $O(10^{-4})$. Therefore the discrepancy in the evaluation of the position of the Fano resonance between the two cases can be ascribed to a renormalization of the energy of the *quasibound* state due to higher order processes which we are unavoidably neglecting.

Once again the work distribution offers a nice explanation in terms of the energy transferred to the system by the quench protocol and how it is distributed across the spectrum of the system. The total energy transferred to the system is given by the first moment of the work distribution [78]. In the insets of Fig. 2.11 we compare the first moment of the work distribution given by the first order LCE [78] (black crosses), with the one obtained from the FD (blue squares) and LCE3 (red disks) approach, and, as expected,

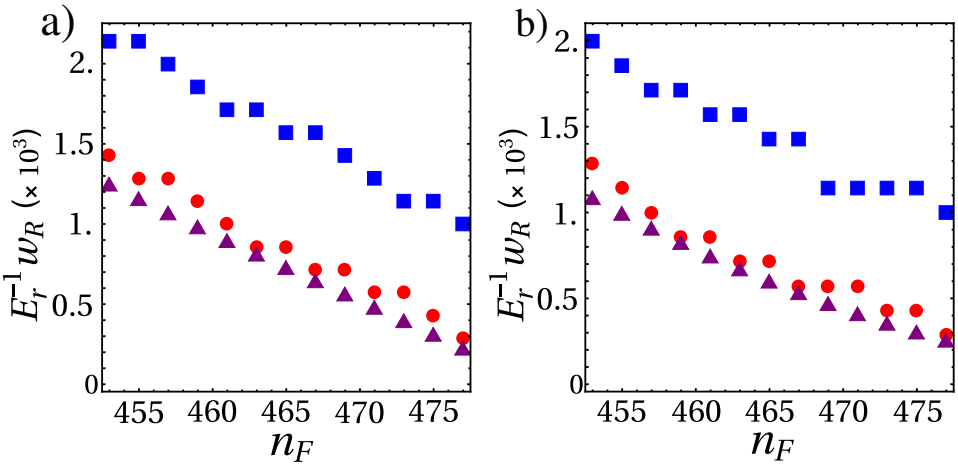

Figure 2.10: Position of the Fano resonances w_R in the work distribution, with respect to the primary peak as a function of the total number of particles N for the same system as in Fig. 2.9. The blue squares refer to the FD approach, whereas red disks are extracted from the LCE, truncated at the third order (LCE-3). The purple triangles label the difference $\epsilon_L - \mu$ between the highest energy of the first band ϵ_L and the chemical potential.

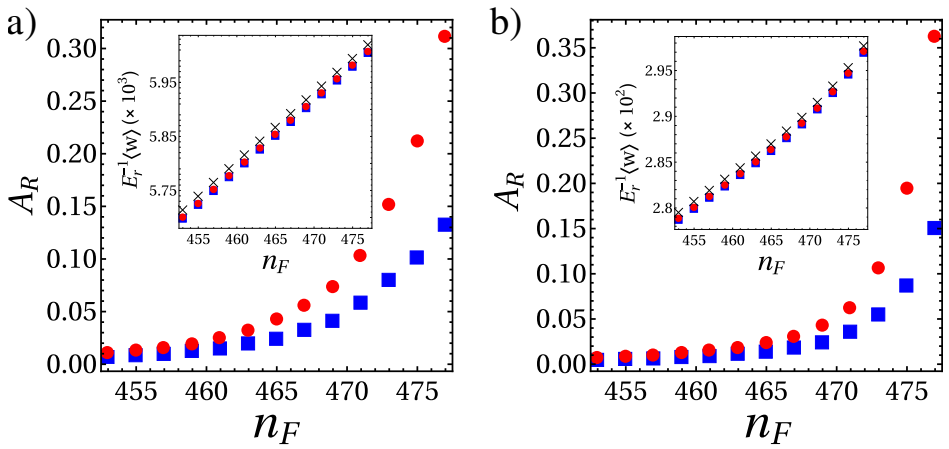

Figure 2.11: Area below the Fano Resonances as a function of the number of particles. All other parameters are the same as in Fig. 2.9 and inverse temperatures $\beta\Delta = 10^6$ [a)] $\beta\Delta = 10^4$ [b)] Insets: First moment of the work distribution. The blue squares refer to the FD approach, whereas red disks are extracted from the LCE, truncated at the third order (LCE-3). The black crosses are the exact value of average work obtained from the first order contribution only [78].

we observe an excellent agreement. The probability to excite the Fano resonance is given by the area below its structure in $P_\beta(w)$, which is typically

larger in the LCE3 than in the FD. This means that LCE3 overesimates the broadening due to the coupling of the *quasibound* state with the continuum, and, due to the conservation of the total area and to the fact that the average work is the same in both approaches, it translates into a lower height and a smaller frequency for the LCE3 than in the FD.

Two conclusions my be drawn from Figs. 2.9, 2.10, and 2.11. First, the resonances are indeed given by the coupling of a particle-hole excitation with the continuum of energy states, namely they are Fano resonances. Second, this effect is not a zero temperature one, but is present also at finite temperature if the thermal energy is not sufficient to overcome the band gap.

2.5 Conclusions

We studied the dynamics of a quantum Fermi gas in an optical lattice following a sudden quench, specifically looking at the Loschmidt echo as a figure of merit of the response of the system to the initial perturbation. We derived the Loschmidt echo via two different strategies based on the calculation of the vacuum persistence amplitude, namely, the functional determinant approach, which is exact, and the linked cluster expansion, truncated at the third order, which is a perturbative technique. We have shown that, when the chemical potential of the system is well inside the valence band, the decay of the echo follows the Mahan-Nozières-De Dominicis power-law decay, which is a signature of the Anderson orthogonality catastrophe. From the second order contribution to the linked cluster expansion we have derived the exponent of the power-law decay and successfully compared it with a fit obtained by the functional determinant approach. We have explored the scenario in which the chemical potential approaches the upper band-edge and, therefore, the system undergoes a transition from a metal to an insulator phase. We have observed that the Loschmidt echo in this case shows oscillations whose amplitude increases with the particle number approaching the transition point. The physical nature of these oscillations has been recast to highlight the role of long living particle-hole excitations interacting with the continuum of particles and holes in the system.

2.A Linked cluster expansion of the vacuum persistence amplitude

The vacuum persistence amplitude of (2.7) may be expanded by the Dyson-Wick series

$$\nu_\beta(t) = 1 + \sum_{m=1}^{\infty} \nu_\beta^{(m)}(t), \tag{2.20}$$

whose coefficients account for processes where the gas retrieves its equilibrium unperturbed configuration after $m = 1, 2, \cdots$ scattering events with the impurity potential:

$$\nu^{(m)}(t) = \frac{(-i)^m}{m!} \int_0^t dt_1 \cdots \int_0^t dt_m \left\langle \mathcal{T} \hat{V}(t_1) \cdots \hat{V}(t_m) \right\rangle_\beta . \tag{2.21}$$

In the interaction picture, with

$$\tilde{V}(t) = \sum_{n,n'} V_{n'n} \tilde{c}^\dagger_{n'}(t) \tilde{c}_n(t), \tag{2.22}$$

the time-evolution of the creation and annihilation operators is the following

$$\tilde{c}^\dagger_{n'}(t) = e^{i\epsilon_{n'}t} \hat{c}^\dagger_{n'}, \qquad \tilde{c}_n(t) = e^{-i\epsilon_n t} \hat{c}_n. \tag{2.23}$$

Accordingly, the grand-canonical average of the time-ordered product in Eq. 2.21 may be written as

$$\begin{aligned} \left\langle \mathcal{T} \tilde{V}(t_1) \cdots \tilde{V}(t_m) \right\rangle_\beta = i^m \sum_{n_1, n'_1} V_{n'_1 n_1} \cdots \sum_{n_m, n'_m} V_{n'_m n_m} \\ \times G^{0(m)}_{n_1 \cdots n_m | n'_1 \cdots n'_m}(t_1 \cdots t_m; t'_1 \cdots t'_m), \end{aligned} \tag{2.24}$$

where

$$\begin{aligned} & G^{0(m)}_{n_1 \cdots n_m | n'_1 \cdots n'_m}(t_1 \cdots t_m; t'_1 \cdots t'_m) \\ & = (-i)^m \left\langle \mathcal{T} \hat{c}_{n_1}(t_1) \ldots \hat{c}_{n_m}(t_m) \hat{c}^\dagger_{n'_m}(t'_m) \cdots \hat{c}^\dagger_{n_1}(t'_1) \right\rangle_\beta . \end{aligned} \tag{2.25}$$

represents an m-body unperturbed Green's function.

We can now use the Wick's theorem to reduce the calculation of Eq. (2.25) to a determinant of the single-particle Green's functions $G^0_n(t)$ given in Eq. (2.18):

$$\begin{aligned} & G^{0(m)}_{n_1 \cdots n_m n'_1 \cdots n'_m}(t_1 \cdots t_m; t'_1 \cdots t'_m) \\ & = \begin{vmatrix} G^0_{n_1}(t_1 - t'_1)\delta_{n_1 n'_1} & \cdots & G^0_{n_1}(t_1 - t'_m)\delta_{n_1 n'_m} \\ G^0_{n_2}(t_1 - t'_1)\delta_{n_2 n'_1} & \cdots & G^0_{n_2}(t_1 - t'_m)\delta_{n_2 n'_m} \\ \vdots & \ddots & \vdots \\ G^0_{n_m}(t_m - t'_1)\delta_{n_m n'_1} & \cdots & G^0_{n_m}(t_m - t'_m)\delta_{n_m n'_m} \end{vmatrix} . \end{aligned} \tag{2.26}$$

Combining Eqs. (2.20) and (2.21) with Eq. (2.24), plus the former determinantal expression (2.26), the different contributions can be organized in such a way that the natural logarithm of the vacuum persistence amplitude $\ln[\nu_\beta(t)]$ equals the sum of the connected diagrams $\Lambda_l^\beta(t)$, given in Eq. (2.17). The disconnected contribution in (2.20) is finally obtained by exponentiating the sum [118], and the first three diagrams of the perturbation expansion are, respectively, given by:

$$\Lambda_1^\beta(t) = \sum_{n_1} V_{n_1 n_1} G^0_{n_1}(0^+) t, \tag{2.27}$$

$$\Lambda_2^\beta(t) = \frac{1}{2} \sum_{n_1,n_2} V_{n_1 n_2} V_{n_2 n_1} \times \int_0^t dt_1 \int_0^t dt_2 G^0_{n_1}(t_1 - t_2) G^0_{n_2}(t_2 - t_1), \quad \text{and} \tag{2.28}$$

$$\Lambda_3^\beta(t) = -\frac{1}{3} \sum_{n_1,n_2,n_3} V_{n_3 n_1} V_{n_1 n_2} V_{n_2 n_3} \times \int_0^t dt_1 \int_0^t dt_2 \int_0^t dt_3 G^0_{n_1}(t_1 - t_2) G^0_{n_2}(t_2 - t_3) G^0_{n_3}(t_3 - t_1). \tag{2.29}$$

2.A.1 Second order expansion of the vacuum persistence amplitude and critical exponent

The application of the LCE up to the second order gives two contributions in the perturbation expansion of Eq. (2.15):

$$\nu_\beta(t) \approx e^{\Lambda_1^\beta(t) + \Lambda_2^\beta(t)} \tag{2.30}$$

The one-vertex loop, given in Eq. (2.27), is just the adiabatic response of the gas, having the form

$$\Lambda_1^\beta(t) = -itE_1^\beta. \tag{2.31}$$

It has been proved that $E_1^\beta = \sum_{n_1} V_{n_1 n_1} f^+_{n_1}$ is the correction to the average equilibrium energy $E_0^\beta = \langle \hat{H}_0 \rangle_\beta = \sum_{n_1} \epsilon_{n_1} f^+_{n_1}$, i.e. that $E_0^\beta + E_1^\beta$ is the exact energy of the gas in equilibrium with the sudden impurity perturbation [77]. This, in turns, implies that the energy shifts E_l^β contained in $\Lambda_l^\beta(t)$ must obey to the sum-rule

$$\sum_{l \geq 2} E_l^\beta = 0. \tag{2.32}$$

The two-vertex loop (2.28) also has a simple structure, once the expression (2.18) for the single particle Green's function is used:

$$\Lambda_2^\beta(t) = -\sum_{n_1,n_2} |V_{n_1 n_2}|^2 \int_0^t dt_1 \int_0^{t_1} dt_2 f^+_{n_1} f^-_{n_2} e^{i(\epsilon_{n_1} - \epsilon_{n_2})(t_1 - t_2)}. \tag{2.33}$$

Here we can distinguish the following three different contributions:

$$\Lambda_{2G}^{\beta}(t) = -\frac{t^2}{2}\sum_{n_1} f_{n_1}^{+}|V_{n_1n_1}|^2 f_{n_1}^{-}, \tag{2.34}$$

$$\Lambda_{2S}^{\beta}(t) = -itE_2^{\beta}, \quad E_2^{\beta} = \sum_{n_1\neq n_2} \frac{f_{n_1}^{+}\,|V_{n_1n_2}|^2\, f_{n_2}^{-}}{\epsilon_{n_1}-\epsilon_{n_2}}, \tag{2.35}$$

$$\Lambda_{2P}^{\beta}(t) = -\sum_{n_1,n_2} \frac{1-e^{i(\epsilon_{n_1}-\epsilon_{n_2})t}}{(\epsilon_{n_1}-\epsilon_{n_2})^2}\,|V_{n_1n_2}|^2\, f_{n_1}^{+} f_{n_2}^{-}, \tag{2.36}$$

which, respectively, represent a Gaussian damping, a second-order energy shift, and an oscillating term, responsible for the Fermi edge singular response of the system [77, 78]. Accordingly, we may write

$$\Lambda_{2}^{\beta}(t) = \Lambda_{2G}^{\beta}(t) + \Lambda_{2S}^{\beta}(t) + \Lambda_{2P}^{\beta}(t) \tag{2.37}$$

where the damping factor $\Lambda_{2G}^{\beta}(t)$ vanishes in the $\beta\to\infty$-limit.

One of the achievements presented in this chapter is the finding of a correspondence between the long-time behavior of the Fermi edge term $\Lambda_{2P}^{\beta}(t)$ and the MND theory [87, 88, 115], via the determination of a critical exponent α, which contains the essence of the shake-up of the gas to the sudden switching of the impurity. Following the original approach by Mahan [87], we use the one-to-one correspondence between the quantum numbers n_i and the one-particle energies $\epsilon_{n_i}\equiv\epsilon_i\geq 0$ to express Eq. (2.34) in the continuous limit. Specifically we replace

$$\sum_{n_1,n_2} \to \int_0^{\epsilon_c} d\epsilon_1 g(\epsilon_1)\int_0^{\epsilon_c} d\epsilon_2 g(\epsilon_2), \tag{2.38}$$

with $g(\epsilon)=dn/d\epsilon$ denoting the density of single-particle states of the unperturbed system, and ϵ_c being a high-energy cut-off of the creder of the first bandwidth. The matrix elements of the perturbation potential (2.3) are easily computed as $V_{n_1n_2}\to V_0\langle x_0|\epsilon_1\rangle\langle\epsilon_2|x_0\rangle$. Then, introducing the weighted density of states $\tilde{g}(\epsilon)=g(\epsilon)|\langle x_0|\epsilon\rangle|^2$, we get:

$$\Lambda_{2P}^{\beta}(t) \to -\frac{V_0^2}{2}\int_0^{\infty} d\epsilon_1\tilde{g}(\epsilon_1)f^{+}(\epsilon_1) \times\int_0^{\infty} d\epsilon_2\tilde{g}(\epsilon_2)f^{-}(\epsilon_2)\frac{1-e^{i(\epsilon_1-\epsilon_2)t}}{(\epsilon_1-\epsilon_2)^2}, \tag{2.39}$$

where the factor of $1/2$ comes from the fact that only half of the single-particle spectrum is involved in the process, say, only the states with even parity, with respect the position x_0 of the impurity, are coupled by the impurity potential. At the absolute zero, the product of the particle-hole distributions

$f^+(\epsilon_1)f^-(\epsilon_2)$ is non-vanishing in the energy intervals $0 < \epsilon_1 < \epsilon_F$ and $\epsilon_F < \epsilon_2 < \epsilon_c$, where we have introduced a high-energy cutoff ϵ_c to compensate the virtually infinite range assumed for the valence band. Then,

$$\Lambda_{2P}^{\infty}(t) \to -\frac{V_0^2}{2}\int_0^{\epsilon_F} d\epsilon_1 \tilde{g}(\epsilon_1)\int_{\epsilon_F}^{\epsilon_c} d\epsilon_2 \tilde{g}(\epsilon_2)\frac{1-e^{i(\epsilon_1-\epsilon_2)t}}{(\epsilon_1-\epsilon_2)^2}. \tag{2.40}$$

We now perform the change of variables $\xi = \epsilon_1 - \epsilon_2$ and $\eta = (\epsilon_1 + \epsilon_2)/2$, which maps the former integral to

$$\Lambda_{\infty}^{(2O)}(t) \to \frac{V_0^2}{2}\iint_{R_{(\epsilon_F|\epsilon_c)}} d\xi d\eta \tilde{g}\left(\eta+\frac{\xi}{2}\right)\tilde{g}\left(\eta-\frac{\xi}{2}\right)\frac{e^{i\xi t}-1}{\xi^2}, \tag{2.41}$$

where

$$\begin{aligned}\iint_{R_{(\epsilon_F|\epsilon_c)}} d\xi d\eta[\cdots] &= \int_{-\epsilon_c}^{-\epsilon_F} d\xi \int_{-\xi/2}^{\xi/2+\epsilon_c} d\eta[\cdots] \\ &+ \int_{-\epsilon_F}^{-\epsilon_c+\epsilon_F} d\xi \int_{\xi/2+\epsilon_F}^{\xi/2+\epsilon_c} d\eta[\cdots] + \int_{-\epsilon_c+\epsilon_F}^{0} d\xi \int_{\xi/2+\epsilon_F}^{-\xi/2+\epsilon_F} d\eta[\cdots]\end{aligned}$$

The integrand in Eq. (2.41) diverges as $\xi \to 0$ and rapidly goes to zero as $\xi \to \infty$. Assuming that the density of states is sufficiently smooth in the region of integration, we can conclude that the dominant contribution to the integral is given in an interval $(-1/\tau_0, 0)$ where $1/\tau_0$ is of the order of $o(t^{-1})$ [87]. In order to extract the leading term in (2.41), it is therefore meaningful to evaluate the integral over η in the region where $\xi \to 0$:

$$\begin{aligned}\iint_{R_{(\epsilon_F|\epsilon_c)}} d\xi d\eta[\cdots] &\approx \int_{-\epsilon_c+\epsilon_F}^{0} d\xi \int_{\xi/2+\epsilon_F}^{-\xi/2+\epsilon_F} d\eta[\cdots] \\ &\approx \int_{-1/\tau_0}^{0} d\xi \int_{\xi/2+\epsilon_F}^{-\xi/2+\epsilon_F} d\eta[\cdots].\end{aligned}$$

Now, assuming $\tau_0\epsilon_F \ll 1$, we may replace the product of density of states with its maximum at ϵ_F, and define $\alpha = V_0^2\tilde{g}^2(\epsilon_F)/2$. Thus, we finally obtain

$$\begin{aligned}\Lambda_{2P}^{\infty}(t) \;\to\; & -\alpha\int_{-1/\tau_0}^{0} d\xi\frac{e^{i\xi t}-1}{\xi} = -\alpha\ln\left(\frac{t}{\tau_0}\right) \\ & -\gamma\alpha - \alpha\int_{1/\tau_0}^{\infty}\frac{\cos(\xi t)}{\xi}d\xi + i\alpha\int_0^{1/\tau_0}\frac{\sin(\xi t)}{\xi}d\xi,\end{aligned} \tag{2.42}$$

with $\gamma \approx 0.577216$ denoting the Euler γ constant. The leading contribution to the former integral provides the long-time power-law behavior of the vacuum persistence amplitude in the MND theory: $e^{\Lambda_{2P}^{\infty}(t)} \to (t/\tau_0)^{-\alpha}$. Interestingly,

the high-energy cutoff in Eq. (2.40) may be replaced the following exponential cutoff

$$\Lambda_{2P}^{\infty}(t) \to -\alpha \int_0^{\epsilon_F} d\epsilon_1 \int_{\epsilon_F}^{\infty} d\epsilon_2 \frac{1-e^{i(\epsilon_1-\epsilon_2)t}}{(\epsilon_1-\epsilon_2)^2} e^{(\epsilon_1-\epsilon_2)\tau_0}, \tag{2.43}$$

which leads to

$$\Lambda_{2P}^{\infty}(t) \to -\alpha \int_{-\infty}^{0} d\xi \frac{e^{i\xi t}-1}{\xi} e^{\xi\tau_0} = -\alpha \ln(1+it/\tau_0). \tag{2.44}$$

Exponentiating this last expression, we get the normalized MND distribution in the time-domain $e^{\Lambda_{2P}^{\infty}(t)} \to \left(\frac{1}{1+it/\tau_0}\right)^{-\alpha}$. Its Fourier transform coincides with the MND excitation spectrum, displaying the Fermi edge singularity

$$\int_{-\infty}^{\infty} \frac{dt}{2\pi} e^{\Lambda_{2P}^{\infty}(t)} e^{i\omega t} = \frac{\tau_0 e^{-\omega\tau_0}\Theta(\omega)}{(\tau_0\omega)^{1-\alpha}\Gamma(\alpha)}, \tag{2.45}$$

in which Γ denotes the Euler gamma function.

2.A.2 Third order contribution to the vacuum persistence amplitude and particle-hole recombination processes

We now discuss the third order of the LCE, which allows us to approximate the vacuum persistence amplitude of Eq. (2.15) as

$$\nu_\beta(t) \approx e^{\Lambda_1^\beta(t)+\Lambda_2^\beta(t)+\Lambda_3^\beta(t)}. \tag{2.46}$$

Specifically, we calculate the three-vertex loop $\Lambda_3^\beta(t)$, starting from Eq. (2.29), and discuss its effect on the total response of the gas.

We begin by properly changing the dummy summation indexes and time variables in the six terms, which are obtained by expanding the product of unperturbed Green's functions in Eq. (2.29). Using the fact that the matrix elements of the impurity potential are real, we can reduce the three-vertex loop to the following two contributions:

$$\begin{aligned}\Lambda_3^\beta(t) = i \sum_{n_1,n_2,n_3} & V_{n_1n_2}V_{n_2n_3}V_{n_3n_1} f_{n_1}^+ f_{n_2}^- f_{n_3}^- A_{n_1n_2n_3}(t) \\ - i \sum_{n_1,n_2,n_3} & V_{n_1n_2}V_{n_2n_3}V_{n_3n_1} f_{n_1}^+ f_{n_2}^- f_{n_3}^+ B_{n_1n_2n_3}(t),\end{aligned} \tag{2.47}$$

where

$$A_{n_1n_2n_3}(t) = \int_0^t dt_1 \int_0^{t_1} dt_2 \int_0^{t_2} dt_3 e^{i\epsilon_{n_1}(t_1-t_2)} e^{i\epsilon_{n_2}(t_2-t_3)} e^{i\epsilon_{n_3}(t_3-t_1)}, \tag{2.48}$$

$$B_{n_1n_2n_3}(t) = \int_0^t dt_1 \int_0^{t_1} dt_3 \int_0^{t_3} dt_2 e^{i\epsilon_{n_1}(t_1-t_2)} e^{i\epsilon_{n_2}(t_2-t_3)} e^{i\epsilon_{n_3}(t_3-t_1)}. \tag{2.49}$$

The first term in Eq. (2.47) is readily interpreted as the scattering of a particle-hole excitation ($f^+_{n_1} f^-_{n_2}$) with a hole ($f^-_{n_3}$), whereas the second term in Eq. (2.47) represents the scattering of the same particle-hole excitation with a particle ($f^+_{n_3}$).

After performing the time-integrals in Eqs. (2.48) and (2.49), we can rearrange the different contributions in Eq. (2.47) similarly to what we have done for the two-vertex loop in Eq. (2.37), obtaining

$$\Lambda^\beta_3(t) = \Lambda^\beta_{3G}(t) + \Lambda^\beta_{3S}(t) + \Lambda^\beta_{3P}(t) + \Lambda^\beta_{3C}(t). \tag{2.50}$$

Here, the first term

$$\Lambda^\beta_{3G}(t) = -\frac{t^2}{2} \sum_{\substack{n_1,n_2 \\ n_1 \neq n_2}} V^2_{n_1n_2} \frac{2 f^+_{n_1} f^-_{n_1} V_{n_1n_1}}{\epsilon_{n_1} - \epsilon_{n_2}} \tag{2.51}$$

is the third-order counterpart of $\Lambda^\beta_{2G}(t)$ [Eq. (2.34)], yielding an additional Gaussian damping to the dynamics of the gas, which becomes vanishingly small as the temperature tends to the absolute zero.

The second term in Eq. (2.50),

$$\Lambda^\beta_{3S}(t) = itE^\beta_3, \tag{2.52}$$

provides the third-order perturbation shift

$$\begin{aligned} E^\beta_3 \;=\; & \sum_{\substack{n_1,n_2,n_3 \\ n_1 \neq n_2 \neq n_3}} \frac{V_{n_1n_2} V_{n_2n_3} V_{n_3n_1}}{\epsilon_{n_1} - \epsilon_{n_3}} \left[\frac{f^+_{n_1} f^+_{n_2} f^-_{n_3}}{\epsilon_{n_2} - \epsilon_{n_3}} - \frac{f^+_{n_1} f^-_{n_2} f^-_{n_3}}{\epsilon_{n_1} - \epsilon_{n_2}} \right] \\ & + \sum_{\substack{n_1,n_2 \\ n_1 \neq n_2}} \frac{V^2_{n_1n_2} V_{n_1n_1}}{(\epsilon_{n_1} - \epsilon_{n_2})^2} \left[f^+_{n_1} f^-_{n_2} - f^+_{n_2} f^-_{n_1} - f^+_{n_1} f^-_{n_1} \left(f^+_{n_2} - f^-_{n_2} \right) \right] \end{aligned} \tag{2.53}$$

to the equilibrium energy of the gas, which combines with the second-order term $\Lambda^\beta_{2S}(t)$ of Eq. (2.34). Nonetheless, as pointed out above, that role of both E^β_2 and E^β_3 is irrelevant, because they are cancelled by terms of the same structure, which appear in the higher-order loops of the LCE [Eq. (2.17)].

The non-trivial content of Eq. (2.50) is, therefore, given by the following oscillating term

$$\Lambda^\beta_{3P}(t) = \Lambda^\beta_{3P_I}(t) + \Lambda^\beta_{3P_{II}}(t), \tag{2.54}$$

where

$$\Lambda^{\beta}_{3P_I}(t) = \sum_{\substack{n_1,n_2 \\ n_1\neq n_2}} \frac{2V^2_{n_1n_2}(V_{n_1n_1}-V_{n_2n_2})}{\epsilon_{n_1}-\epsilon_{n_2}} \frac{1-e^{it\left(\epsilon_{n_1}-\epsilon_{n_2}\right)}}{(\epsilon_{n_1}-\epsilon_{n_2})^2} f^+_{n_1} f^-_{n_2} \tag{2.55}$$

effectively acts to renormalize the shake-up response of the gas $\Lambda^{\beta}_{2P}(t)$, given in Eq. (2.36), and in particular the critical exponent of its continuous limit expression, established by Eq. (2.42) or Eq. (2.44), while

$$\begin{aligned}\Lambda^{\beta}_{3P_{II}}(t) = & \sum_{\substack{n_1,n_2,n_3 \\ n_1\neq n_2\neq n_3}} \frac{V_{n_1n_2}}{\epsilon_{n_3}-\epsilon_{n_2}} f^+_{n_1} f^-_{n_2} f^-_{n_3} \\ & \times \left[\frac{1-e^{it\left(\epsilon_{n_1}-\epsilon_{n_2}\right)}}{(\epsilon_{n_1}-\epsilon_{n_2})^2} - \frac{1-e^{it\left(\epsilon_{n_1}-\epsilon_{n_3}\right)}}{(\epsilon_{n_1}-\epsilon_{n_3})^2}\right] \\ & + \sum_{\substack{n_1,n_2,n_3 \\ n_1\neq n_2\neq n_3}} \frac{V_{n_1n_2}V_{n_1n_3}V_{n_2n_3}}{\epsilon_{n_3}-\epsilon_{n_1}} f^+_{n_1} f^-_{n_2} f^+_{n_3} \\ & \times \left[\frac{1-e^{it\left(\epsilon_{n_1}-\epsilon_{n_2}\right)}}{(\epsilon_{n_1}-\epsilon_{n_2})^2} - \frac{1-e^{it\left(\epsilon_{n_3}-\epsilon_{n_2}\right)}}{(\epsilon_{n_3}-\epsilon_{n_2})^2}\right]\end{aligned} \tag{2.56}$$

has no counterpart in the LCE, truncated to the second order. It accounts for particle ($f^+_{n_3}$) or hole ($f^-_{n_3}$) propagation screened by particle-hole recombination processes ($f^+_{n_1}f^-_{n_2}$). As suggested in Sec. 2.4.2, we believe that this last term plays a non-negligible role in the Fano resonance lineshape that characterizes the absorption spectrum (or the work distribution) of the gas, approaching the metal-to-insulator change of phase, from the metal side.

The last contribution to Eq. (2.50) is the following

$$\begin{aligned}\Lambda^{\beta}_{3C}(t) = & -\frac{it^3}{3!}\sum_{n_1} V^3_{n_1n_1} f^+_{n_1} f^-_{n_1} (f^+_{n_1} - f^-_{n_1}) \\ & + it \sum_{\substack{n_1,n_2 \\ n_1\neq n_2}} \frac{V^2_{n_1n_2} f^+_{n_1} f^-_{n_2} e^{it(\epsilon_{n_1}-\epsilon_{n_2})}}{(\epsilon_{n_1}-\epsilon_{n_2})^2} \left(V_{n_1n_1} f^+_{n_1} - V_{n_2n_2} f^-_{n_2}\right)\end{aligned} \tag{2.57}$$

which allows for non-zero skewness and more complex asymmetries in the absorption spectrum (or work distribution), at finite temperatures.

3

Post quench dynamics of a Fermi gas with singular continuous spectrum

In un vortice di polvere
gli altri vedevan siccità,
a me ricordava
la gonna di Jenny
in un ballo di tanti anni fa.

– Fabrizio De André, *Il suonatore Jones*

In this chapter we investigate the dynamical properties of an interacting many-body system with a non-trivial energy potential landscape, which can induce a singular continuous single-particle energy spectrum. After describing the model in sec. 3.1, we show that the interplay between the quasi-periodicity of the lattice, i.e. the geometry of the system, and the many-body interactions gives rise to anomalous propagation properties, which have been observed in recent experiments [63, 98], secs. 3.2 and 3.3. We provide an explanation of this phenomenon which is based on the nature of the single particle energy spectrum (SPES), in sec. 3.4. We sketch a phase diagram of the AAM in Fig. 3.1, in terms of the interaction strength U, and of the onsite potential λ. We find different dynamical regimes for the system: an ergodic one at small λ with an AC SPES, a localized one at large λ and moderately small U with a PP SPES, and an intermediate anomalous one characterized by a SC SPES. This rich picture arises from a non-trivial competition between the underlying order induced by the potential energy landscape and the many-body interactions. Our study shows that singular-continuous spectra

can be found in interacting systems unlike previously conjectured by treating the interactions in the mean-field approximation. This in turn also shows the importance of the many-body correlations in giving rise to this anomalous dynamics and that it is a signature of a non-trivial interplay between geometry and interactions in many-body systems.

3.1 Model and physical quantities

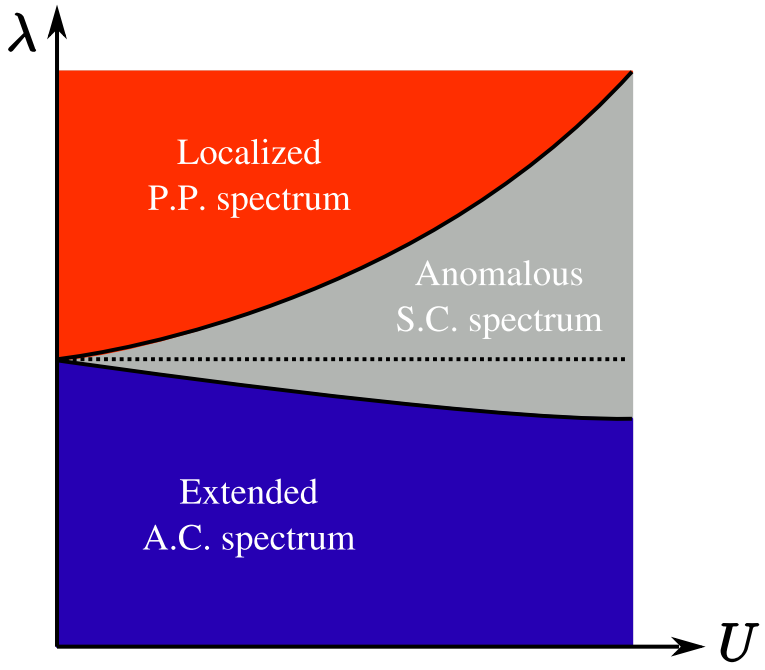

Figure 3.1: Conjectured phase diagram for spin-1/2 AAM consistent with the behaviour of the imbalance at long times and the nature of the SPES.

We consider a gas of spin-1/2 particles in one dimension, described by the Fermi-Hubbard model:

$$\hat{H} = \sum_{n,\sigma} \epsilon_n \hat{c}^\dagger_{n,\sigma} \hat{c}_{n,\sigma} - \frac{J}{2} \left(\hat{c}^\dagger_{n,+1,\sigma} \hat{c}_{n,\sigma} + \text{h.c.} \right) + U \hat{n}_{n,\uparrow} \hat{n}_{n,\downarrow}, \tag{3.1}$$

where ϵ_n is the onsite energy, U the on-site interaction between particles with different spin in the s-wave approximation, $\hat{c}^\dagger_{n,\sigma}(\hat{c}_{n,\sigma})$ are fermion creation (annihilation) operators at site n with spin σ and $\hat{n}_{n,\sigma} = \hat{c}^\dagger_{n,\sigma} \hat{c}_{n,\sigma}$ the corresponding number operator. We work with open boundary conditions not to enforce any artificial periodicity. The AAM is obtained by setting

$\epsilon_n = \Delta \cos(2\pi\tau n)$ [1] with $\tau = \left(\sqrt{5}+1\right)/2$ and $\lambda = \Delta/J$, see sec. 1.1.2.

In this chapter we will compare the results of the AAM with that of another quasicrystal, the on-site Fibonacci model (OFM) obtained by setting $\epsilon_n = \Delta(\lfloor n+1 \rfloor - \lfloor n \rfloor)$ in Eq. (3.1) and again $\lambda = \Delta/J$, whose spectrum has been proved to be SC [125], and that doesn't have any SP phase transition.

If not otherwise stated, we consider an initial state similar to the one in the experiment [98]: two particles with opposite spin on even sites instead of a random distribution of up and down spin particles on even sites, in order to avoid the effective interaction to depend on the particular realization. The subsequent time evolution is then generated by the Hamiltonian in Eq. (3.1)[2]. In the case of ultracold gases, this corresponds to a quench where at the initial time $t = 0$ both nearest-neighbour tunneling and onsite interaction are brought to finite values on a time scale much shorter than the tunneling time J^{-1}, but large enough not to excite transitions to higher bands, for which the TB model does not work anymore [126].

At the single particle level, the dynamics of the system is encoded in the lesser Green's function defined as $G^{<}_{s,s'}(t;t') = i\langle \hat{c}^{\dagger}_{s'}(t')\hat{c}_s(t)\rangle_0$, where the average is on the initial state, and we use the notation $s = n, \sigma$.

To compute this quantity we resort to the non-equilibrium Green's functions technique, by solving numerically the Dyson equation for the single-particle Green's function. Our approach is detailed in [127] and is based on the self-consistent solution of the Dyson equation once a choice for the self-energy is made. It closely follows the one of Refs. [128, 129] and is an extension of the approach presented in Ref. [130] for bosonic systems. The self-energy entering the Dyson equation is calculated in the second-Born approximation [81].

3.2 Geometry-induced anomalous diffusion

We start by looking at the role of the geometry of the potential energy landscape, which affects the spreading of the correlations due to its influence on the nature of the SPES. The spreading of correlations in a non-interacting system with a continuous energy spectrum (corresponding to extended eigenstates) is ballistic with a maximum velocity determined by both the energy spectrum and the initial state but it is always finite and bounded from above

[1] We set the phase of the cos function to zero; its variation has two main effects on the single-particle energy spectrum: a reshuffling of the bulk eigenstates with respect to the eigenenergies and the change in the energy of the two (localized) boundary states. For both these effects do not affect the single-particle energy spectrum and its nature, it has no effects on the results discussed in our work.

[2] It is important to mention that the above beaviour is independent on the choice of the initial state the latter being spread among most of the eigenstates of the system in the delocalized region and therefore the dynamics explores most of its spectrum. This is analogous to the cases analyzed in Ref. [96]

by the Lieb-Robinson bound [131]. In the case of a discrete energy spectrum (with exponentially localized eigenstates), the spreading is suppressed and correlations develop only in a finite region whose size is proportional to the localization length, thus going to zero in the thermodynamics limit.

In order to quantify the the spreading of the correlations we use the variance of the probability distribution defined as $P_i(t) = |G^<_{i_0,i}(0;t)|^2$, similarly to what has been done in Ref. [130]. Due to the absence of interaction, the spin degree of freedom is irrelevant; therefore, the results are identical to the ones for spinless fermions when $U = 0$.

In Fig. 3.2, we show the probability distribution $P_i(t)$ for the AAM with $L = 200$ sites in the metallic (extended) phase ($\lambda = 0.8$) and at the transition point ($\lambda = 1$). It can be clearly seen that below the transition point the spreading is ballistic, whereas, at the transition point, it acquires a (possibly anomalous) diffusive behaviour.

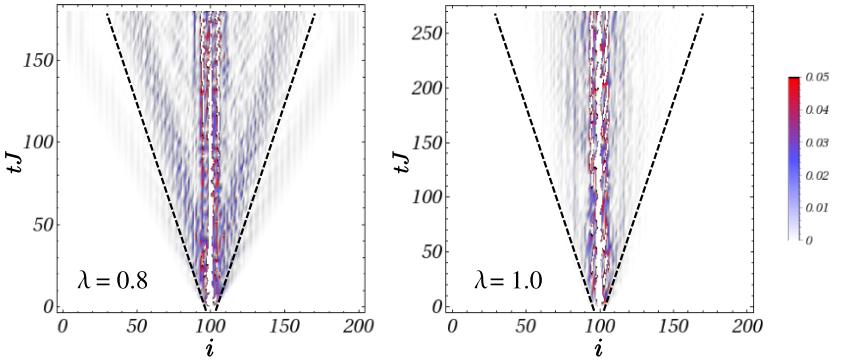

Figure 3.2: Panel **a)**: Correlation function $|G^<_{i_0 i}(0;t)|^2$ for a quench corresponding to an initial system with $N = 100$ particles frozen in the even sites of a lattice with $L = 200$ sites. At $t = 0$, the tunneling is suddenly switched on ($J \neq 0$). Left and right plots refer to the cases $\lambda = 0.8$ and $\lambda = 1$, respectively. Black (dashed) lines are drawn to guide the eye identifying the light cone spreading of correlations.

By focusing on the variance $\sigma(t)$ of $P_i(t)$, and assuming a power law behaviour, $\sigma(t) \propto t^\alpha$ for $Jt \gg 1$, we looked at the behaviour of the exponent α for different system sizes and different values of λ. The results are shown in Fig. 3.3 panel **a)**, where we can see that for the AAM, the expansion tends to be ballistic in the thermodynamic limit ($\alpha = 1$) for $\lambda < 1$ and suppressed for $\lambda < 1$. The residual expansion for $\lambda > 1$ can be attributed to the tails of the exponentially localized eigenstates (due to the finite size). At $\lambda = 1$ curves for different size meet with the exponent dropping to $\alpha \approx 1/2$, thus signaling deviation from both ballistic or localized behaviour.

It is interesting to compare these features with those of the on-site Fibonacci model (OFM), showing a purely SC energy spectrum [125] induced

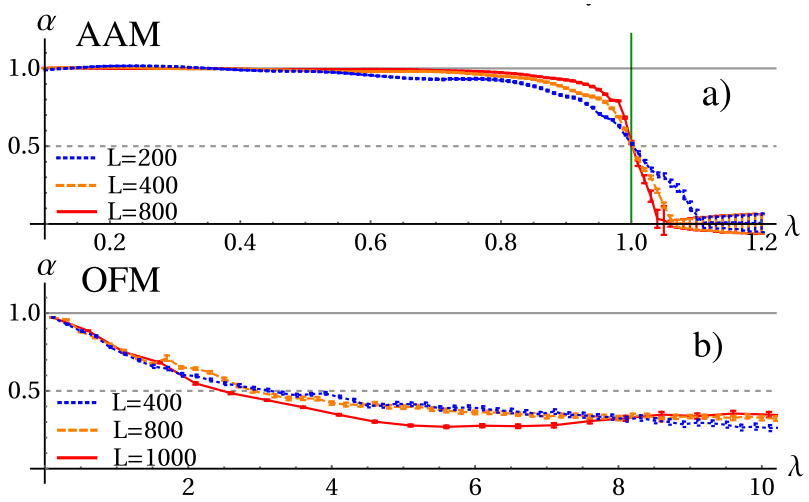

Figure 3.3: Panels **a)** and **b)**: Exponent of the power law $\sigma(t) \propto t^{\alpha}$ as a function of the onsite potential strength λ. **a)** refers to the AAM with $L = 200$ (dotted blue line), $L = 400$ (dashed orange line), $L = 800$ (solid red line), while **b)** refers to the OFM with $L = 400$ (dotted blue line), $L = 800$ (dashed orange line),$L = 1000$ (solid red line). Solid and dashed horizontal lines highlight the values of the exponent $\alpha_B = 1$, $\alpha_D = 0.5$ expected for ballistic and diffusive spreading, respectively. The solid green vertical line at $\lambda = 1$ in panel **a)** is the critical value at which the AAM shows the metal-to-insulator transition in the thermodynamic limit.

by its quasiperiodic geometry [134, 135], and displaying no phase transition. The results are shown in Fig. 3.3 panel **b)**, where we can appreciate a deviation from ballistic spreading at any finite λ. This behaviour can be traced back to the critical nature of the eigenfunctions together with the SC nature of the spectrum [92, 96, 125] and it is shared by other aperiodic structures [132, 133].

We can drawn some conclusions from the above observations. The AAM for $\lambda < 1 (\lambda > 1)$ behaves as any non-interacting system with a continuous (discrete) energy spectrum, inducing ballistic (suppression of) propagation of correlations. At the transition point the spreading turns diffusive, a behaviour usually arising in the presence of interactions and/or phase boundaries (as is the case for the AAM at $\lambda = 1$). In the OFM, the system shows anomalous diffusion despite the absence of any phase transition and/or crossover between different phases. The AAM and the OFM share a common feature: the nature of the single-particle spectrum at the transition point for the AAM and that of the OFM for any finite value of λ is singular continuous with critical eigenstates, which manifest as an anomalous diffusive behaviour.

3.3 Interplay between interaction and geometry

The presence of interaction can alter the transport properties in a substantial way; for example, when the non-interacting single particle eigenfunctions are extended states, the spreading turns from ballistic to diffusive as the interaction strength is increased [126, 130]. On the other hand, we have just shown that an anomalous diffusion can arise in a non-interacting system solely due to the properties of the underlying geometry of the potential energy landscape. A natural question to ask is then how the dynamical properties due to a non-trivial underlying geometry are affected by the interactions. To answer this question, we look at the dynamics of a many-body interacting system described by the Hamiltonian in Eq.(3.1) both for the AAM and the OFM.

We introduce the particle imbalance, defined as $\Delta N(t) = (N_e(t) - N_o(t))/N_{tot}$, where $N_{e(o)}(t)$ is the number of particles at the even(odd) sites at time t and N_{tot} is the total number of particles in the system. This is an experimentally accessible physical quantity [63, 98, 126] and therefore all our results can be readily verified. Moreover it is a good figure-of-merit for the diffusion properties of a system: in a delocalized (ergodic) phase $\Delta N(t) \to 0$ on a single-particle time scale ($\sim J^{-1}$) and all particles will be redistributed among different sites. In a localized phase, $\Delta N(t) \to \bar{N}(\lambda, U) \neq 0$ at long times ($Jt \gg 1$). In Refs. [63, 98] it has been shown that this is true away from the zero-interaction transition point. Close to $\lambda = 1$, $\Delta N \to 0$ with a power-law behaviour. The latter is a signature of a non-trivial interplay between the effect of interaction and geometry, that we want to investigate here in more detail.

Fig. 3.4 **a)** reports the imbalance $\Delta N(t)$ for the AAM and for $U = 0.4J$ and for different values of λ. We fitted[3] the imbalance with a power-law of the form $\Delta N(t) = at^{-\beta}$ (inset). The exponent β is shown in Fig.3.5 **a)**, **b)** and **c)**. For $\lambda < 1$ $\Delta N(t) \to 0$ and a super-diffusive behaviour ($1/2 < \beta \lesssim 1$) is observed with β decreasing with U as expected for 1D systems at small interactions in the ergodic phase [126]. For $\lambda > 1$ there are two appreciably different behaviours depending on the interactions. There exists a critical value of the interaction $U_c(\lambda)$ such that: for $U < U_c(\lambda)$ $\Delta N(t) \to \bar{N} \neq 0$, $\beta \approx 0$, thus signaling localization at long times and the exponent grows with U; for $U \geq U_c(\lambda)$, $\Delta N(t) \to 0$ with a power-law whose exponent is smaller than in the delocalized phase showing a sub-diffusive behaviour ($0 < \beta \lesssim 1/2$). In this latter region of parameters the time scale of the dynamics shows an anomalous dilation compared to the single particle one

[3] All fits have been done by excluding the first few tunneling times and specifically for $J^{-1}t \geq 5$. The same procedure has been applied in ref. [98]. The reason is grounded in the idea of excluding the initial transient in which the dynamics is ruled by single particle tunneling and retain only the asymptotic behaviour.

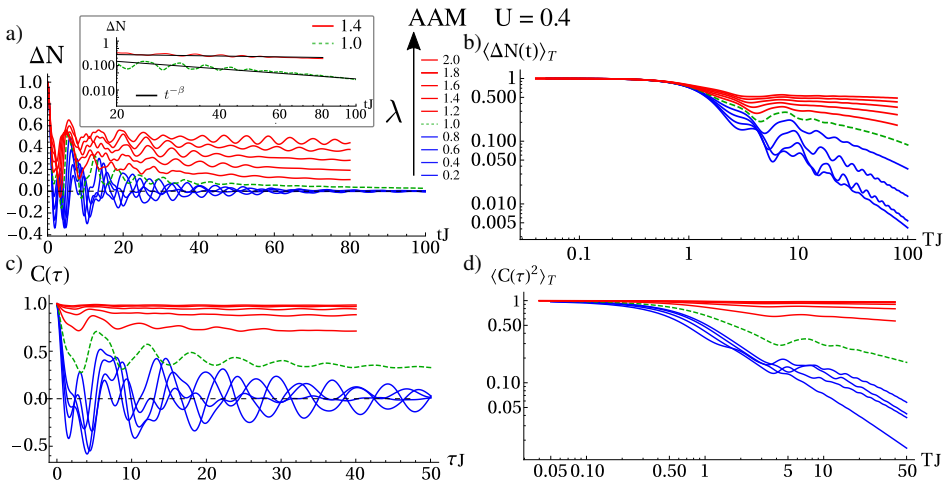

Figure 3.4: **a)** Particle imbalance between even and odd sites, $\Delta N(t)$, **b)** Time-average $\langle \Delta N(t) \rangle_T$, **c)** autocorrelation function and **d)** its time-averaged square $\langle C^2(\tau) \rangle_T$ for a system with $L = 40$ sites in the interacting AAM for $U = 0.4J$ for different values of λ. The inset in panel **a)** shows the signal and the corresponding power-law fit for the cases (dashed green) $\lambda = 1.0$ and (solid red) $\lambda = 1.4$

but it is still far from being strongly localized.

Fig. 3.5 **c)** shows also that the exponents of our fits are quantitatively comparable with those extracted from the experiment in Ref. [98].

3.4 SC spectrum in interacting systems

We shall show that this time-scale-dilation is not a legacy of the transition at $U = 0$ but it has a deeper origin. This statement is supported by the behaviour of the interacting OFM. In Fig. 3.6 **a)**, we show the imbalance $\Delta N(t)$. For small values of λ, $\Delta N(t) \to 0$; for large λ, a power-law behaviour emerges similarly to the AAM. We therefore conjecture that the slowing down arises as a result of the non-trivial competition between the geometry of the underlying energy-landscape and the two-body interaction. To give to the above conjecture a more solid ground we shall show that the geometry-interaction interplay affects the nature of the SPES [4] and that there is a relation between the slowing-down and its SC nature. Let us introduce the following quantities: the time-averaged imbalance $\langle \Delta N(t) \rangle_T = T^{-1} \int_0^T dt \;\; \Delta N(t)$, the time-

[4]Here by single particle spectrum we mean the single particle excitation spectrum, see appendix 3.A

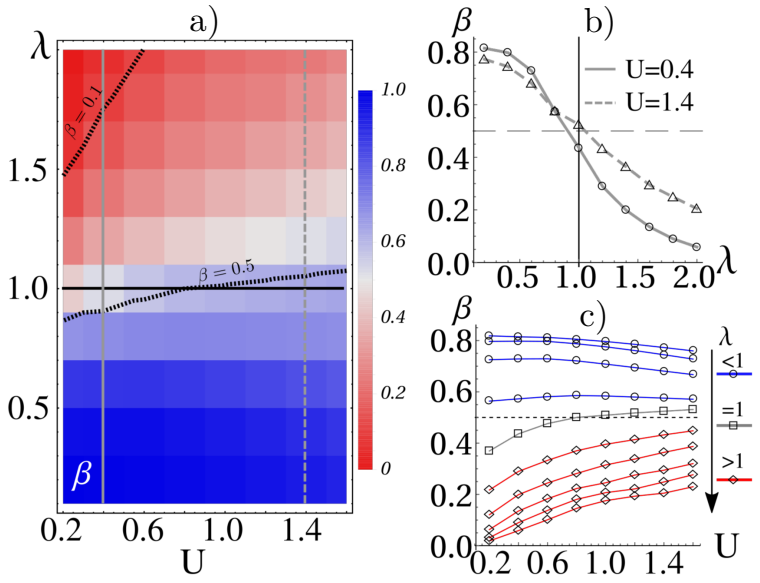

Figure 3.5: a) Exponent of the power-law behaviour $\Delta N(t) \propto a\ t^{-\beta}$ for the imbalance for the AAM as a function of the potential strength λ and interaction U. The black dashed curves identify $\beta = const$ levels whereas the vertical gray lines are the $U = const$ cuts shown in panel b). b) Exponent β for two different interactions (solid) $U = 0.4$ and (dashed) as a function of λ. c) Exponent β as a function of U for different values of λ.

averaged autocorrelation function $C(\tau) = \langle \Delta N^2(t) \rangle^{-1} \langle \Delta N(t) \Delta N(t+\tau) \rangle$ and its time average $\langle |C(\tau)|^2 \rangle_T = T^{-1} \int_0^T d\tau\ |C(\tau)|^2$. By following the discussions in Refs. [94, 130, 136, 137], we can use them to investigate the nature of the SPES. Specifically we make use of the Ruelle-Amrein-Georgescu-Enss (RAGE) theorem and the Wiener's lemma, and the Lebesgue-Riemann theorem. They help us in establishing the conditions for the system to have a SC component (appendix 3.B): $\lim_{T\to\infty} \langle \Delta N(t) \rangle_T = 0 \wedge \lim_{\tau\to\infty} C(\tau) \neq 0$. The first condition excludes the presence of a PP part whereas the second ensures that no AC part is present (appendix 3.B). The quantity $\langle C^2(\tau) \rangle_T$ plays a similar role as $\langle \Delta N(t) \rangle_T$, but due to numerical limitations it is more difficult to extract information on the whole parameter region spanned. It is nevertheless important to check that its behaviour is consistent with that of $\langle \Delta N(t) \rangle_T$ (appendix 3.B). Theses quantities for the data in Fig.3.4 **a)** are shown in Fig.3.4 **b)-d)**. In each of them we can distinguish markedly different behaviours: a fast decay to zero, a slow decay towards zero and a decay towards a non-zero asymptotic value. In order to discuss their decay properties on a more quantitative grounds we plot in Fig. 3.7 the exponents

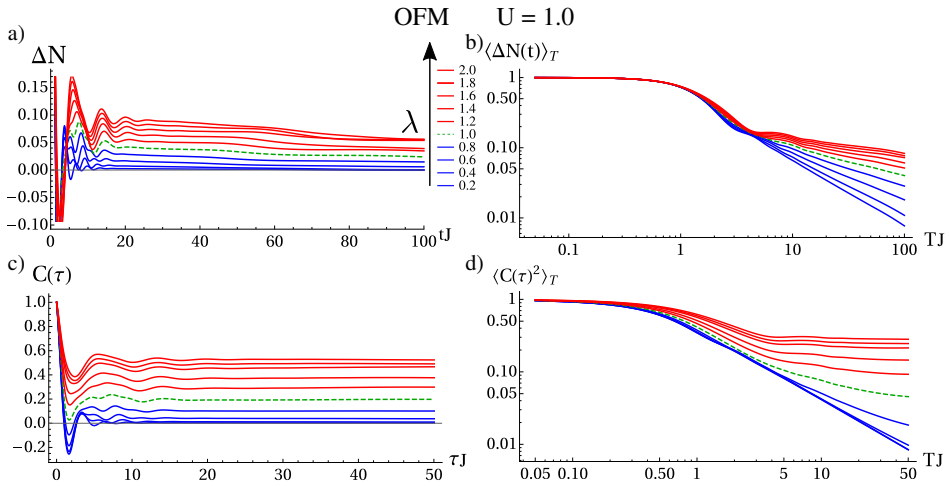

Figure 3.6: **a)** Particle imbalance between even and odd sites, $\Delta N(t)$, **b)** Time-average $\langle \Delta N(t) \rangle_T$, **c)** autocorrelation function and **d)** its time-averaged square $\langle C^2(\tau) \rangle_T$ for a system with $L = 40$ sites in the interacting OFM for $U = 1.0J$ for different values of λ.

of the fit for a power-law functional dependency for $\langle \Delta N(t) \rangle_T \propto T^{-\gamma}$ **(a)**) and $C(\tau) \propto \tau^{-\delta}$ **(b)**). We see that there is a region for which $\gamma < 0.1$ which we assume as a threshold for a non-decaying signal. According to the RAGE theorem, for the set of points below this line ($\gamma > 0.1$) the SPES does not have a PP component. We have also added a second threshold at $\gamma = 0.4$ which is the value around which the $\lambda = 1$ point develops by increasing the interaction. Below this line ($\gamma > 0.4$) we expect the system to have only purely AC spectrum, but the presence of a SC part cannot be excluded by our analysis. If we now look at the values for δ, we see that there is a region where $\delta < 0.2$, for which $C(\tau)$ decays very slowly and we expect the system not to have any AC component in its spectrum. Putting all together we can say that in the region of parameters such that $\gamma > 0.1$ and $\delta < 0.2$ the spectrum of the system is purely SC. It is important to note that the region in which a SC component is present can be larger as we are looking at regions where the spectrum is *purely* SC. We cannot exclude that there is a SC component also in the region $\delta > 0.2$ meaning that the overall region in which the SC part is present could be larger than the one we identified with our analysis.

With the help of Fig. 3.5 **a)** we observe that there is a good overlap between the region in which the anomalous slowing-down of $\Delta N(t)$ is observed and the region in which the system has a SC SPES.

In Figs. 3.6 **b)-d)**, we can appreciate the same qualitative behaviour for the OFM. Once again this rules out the role of the the transition at $\lambda = 1$

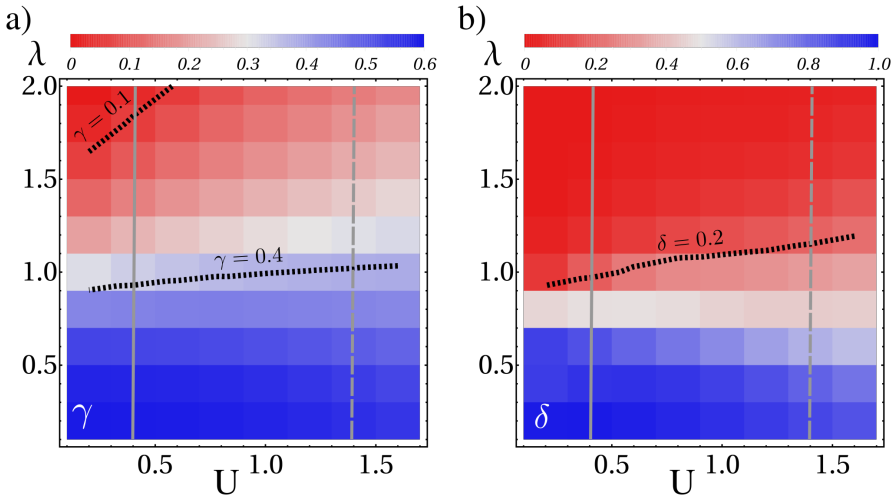

Figure 3.7: Exponents of the power-laws: a) for the the time-averaged imbalance and $\langle \Delta N(t) \rangle_T \propto T^{-\gamma}$ b) for the time-averaged autocorrelation function $C(\tau) \propto \tau^{-\delta}$ in the AAM as a function of the potential strength λ and interaction U. The black dashed curves identify $\gamma = const$ and $\delta = const$.

and $U = 0$ for the AAM as the mechanism responsible for the slowing-down in the presence of interactions and instead strengthens our conclusions on the emergence of the properties of SC spectra in the dynamics of the system.

As a side result, we demonstrated that SC spectra are robust when many-body interactions are added, thus leaving hope of observing the unusual properties of quasicrystalline materials also in moderately interacting systems. This is in constrast with previous predictions [117,138] based on effective non-interacting models. We can also conclude that many-body correlations are a key ingredient in the development of the discussed anomalous behaviour.

3.5 Conclusions

To summarize, we have investigated the redistribution of particles initially held in an uncorrelated state with an inhomogeneous spatial distribution. We have found an anomalous behaviour in the AAM in a finite region of the plane (U, λ), which occurs only at the transition point in the non-interacting case. Aiming at showing that this behaviour is not a legacy of the non-interacting transition point, we looked for a comparison at the interacting on-site Fibonacci model, which lacks transitions of any type in

the non-interacting case. We have found that an anomalous redistribution of particles occurs for this model as well. In order to explain this behaviour, we resorted to the Lesbegue decomposition of positive measures to show that the power-law behaviour is a consequence of the singular continuous nature of the single particle spectrum of the interacting system .

We conjecture that the microscopic mechanism behind this phenomenon has to be sough in the critical nature of the single-particle natural orbitals of the reduced density matrix of the interacting system at stationarity, similarly to the case of non-interacting systems with quasicrystalline geometries [92].

3.A Single particle energy spectrum

We want to clarify what the meaning of "single-particle energy spectrum" used in the main text in the case of an interacting many-body system. We will follow loosely the treatment given in Ref. [81] (Chap. 6). In the main text we have chosen the local density as a figure of merit to analyze the spectral properties, which in terms of the Green's function is simply given by $n_i(t) = -iG^<_{ii}(t;t)$. The latter can be written as:

$$G^<_{ii}(t;t) = i \left\langle e^{i\hat{H}t} \hat{n}_i e^{-i\hat{H}t} \right\rangle_{\hat{\rho}_0} \tag{3.2}$$

We now introduce the identity operator:

$$\hat{\mathbb{I}} = \int_\sigma d\epsilon \ |\Psi(\epsilon)\rangle\langle\Psi(\epsilon)| \tag{3.3}$$

where the integral is over the *whole* spectrum σ of the Hamiltonian $\hat{H}$, namely over the closure of the complement of the resolvent set define as $\rho = \{\lambda | (H - \lambda\mathbb{I})^{-1}$ is a bounded operator$\}$ with respect to $\mathbb{R}$. According to the Lebesgue decomposition theorem the spectrum is the union of three components $\sigma = \sigma_{ac} \cup \sigma_{sc} \cup \sigma_{pp}$ where ac, sc and pp stand for absolutely continuous, singular continuous and pure point respectively. When ϵ belongs to the pp part of the spectrum the integral notation is assumed to be replaced by a sum. Inserting two identities into the expression for the lesser Green's function we obtain:

$$G^<_{ii}(t;t) = i \int_\sigma d\epsilon d\epsilon' \ \ e^{i(\epsilon' - \epsilon)t} f_i(\epsilon, \epsilon') \tag{3.4}$$

where $f_i(\epsilon, \epsilon') = \langle\Psi(\epsilon)|\hat{\rho}_0|\Psi(\epsilon')\rangle \ \langle\Psi(\epsilon')|\hat{n}_i|\Psi(\epsilon)\rangle$. The above expression can be recast into the form:

$$G^<_{ii}(t;t) = i \int_{-\infty}^{\infty} e^{i\omega t} \, d\omega \ \mu_i(\omega) \tag{3.5}$$

where we defined: $\mu_i(\omega) = \int_\sigma d\epsilon d\epsilon' \ \ \delta(\omega - (\epsilon' - \epsilon)) \ f_i(\epsilon, \epsilon')$

In this form the mean value of the the number of particle at site i and time t can be interpreted as the Fourier transform of a measure μ_i which has support on the spectrum of the total Hamiltonian $\hat{H}$. Moreover from the expression of μ_i we see that the measure is computed on the differences $\epsilon' - \epsilon$, namely it runs over all particle-hole like excitations of the many-body system. In this respect it can be seen as the single particle excitation spectrum. To better understand this concept let us look at a specific example. Let us consider the case of a Fermi gas of N particles at zero temperature and at equilibrium, whose Hamiltonian is $\hat{H}_0$. If we now add a one-body perturbation the total Hamiltonian reads $\hat{H} = \hat{H}_0 + \delta\hat{V}$ and $\delta\hat{V}$ a small perturbation. Let us assume that at time $t = 0$ we suddenly switch this perturbation on (quantum quench). We then expect that the explored spectrum will be that of all particle-hole excitations around the initial Fermi energy.

In the case of the initial state considered in the work presented in the main text we expect to explore most of the single-particle excitation spectrum as the initial state is a very highly excited one.

3.B Analysis of the spectral properties

The link between the dynamics of the system and the nature of the support of the spectrum of the single-particle energy spectrum can be highlighted by resorting to the theory of spectral analysis of operators. It will be useful in the following to define the continuous component of a spectrum given by $\sigma_c = \sigma_{ac} \cup \sigma_{sc}$.

Let us introduce the RAGE (Ruelle-Amrein-Georgescu-Enss) theorem [136, 139] which relates the time average of the mean of a compact operator to the presence of a continuous part. Given a compact operator $\hat{A}$ we define the time average of its expectation value at time t as:

$$\langle\langle \hat{A} \rangle\rangle_T = \frac{1}{T} \int_0^T dt \, \langle \hat{A}(t) \rangle_{\hat{\rho}_0} \tag{3.6}$$

The RAGE theorem states that

$$\lim_{T\to\infty} \langle\langle A \rangle\rangle_T = 0 \Leftrightarrow \sigma \subseteq \sigma_c \tag{3.7}$$

The RAGE theorem gives a way to infer the presence of a pure-point component in the single-particle energy spectrum which is guaranteed by the condition $\lim_{T\to\infty}\langle\langle A\rangle\rangle_T \neq 0$.

The number operator is a compact operator as it is a linear combination of projection operators; for the same reason also the imbalance operator is a compact operator and therefore the RAGE theorem applies to the quantity $\langle \Delta N(t) \rangle_T$ considered in the main text.

The RAGE theorem alone still does not rule out the presence of an absolutely continuous part whenever the time average goes to zero at long times. In order to assess the presence (or absence) of the absolutely continuous part we look at the autocorrelation function:

$$C(\tau) = \frac{\left\langle \left\langle \hat{A}(t) \right\rangle_{\hat{\rho}_0} \left\langle \hat{A}(t+\tau) \right\rangle_{\hat{\rho}_0} \right\rangle_t}{\left\langle \left\langle \hat{A}(t) \right\rangle^2_{\hat{\rho}_0} \right\rangle_t} \tag{3.8}$$

In the spectral analysis of signals the autocorrelation functions are a powerful method to asses the presence of correlations in time-series at different time lags and can be therefore used to make statements on the nature of the spectrum without having direct access to the harmonic analysis of the signal itself. Loosely speaking if the spectrum has a pure point spectrum one expects sustained oscillations in the autocorrelation function showing order in the time. The autocorrelation function will instead decay to zero if the signal is not correlated at long times, a feature to be expected in the presence of a continuous spectrum. This physical intuition finds a more rigorous mathematical formulation which will try to present briefly in the following. It easy to see that in the case of the imbalance operator $\Delta\hat{N} \equiv \sum_i (-1)^i \hat{n}_i$ the autocorrelation function is given by :

$$C(\tau) = \int_{-\infty}^{\infty} e^{i\omega\tau} d\omega \;\; |f(\omega)|^2 \tag{3.9}$$

with $\mu(\omega) = \sum_i (-1)^i \mu_i(\omega)/N$ with $N = \int_{-\infty}^{\infty} d\omega \quad |\sum_i (-1)^i \mu_i(\omega)|^2$. Therefore the autocorrelation functions are nothing but the Fourier transform of a (positive) measure. Comparing it with Eq. 3.5 we see that this measure is the squared modulus of the sum of measures giving the occupation number at different sites.

Therefore it turns out that the averaged autocorrelation function is nothing but the Fourier transform of the measure $d\omega|f(\omega)|^2$. We can use its asymptotic behaviour to detect the presence of an absolutely continuous component of the spectrum. Specifically the Riemann-Lebesgue theorem tells us that $\lim_{\tau\to\infty} C(\tau) = 0$ is a necessary condition for the spectrum to be *purely* absolutely continuous. This means that $\lim_{\tau\to\infty} C(\tau) \neq 0$ implies that the spectrum is such that $\sigma \subseteq \sigma_s$ where $\sigma_s = \sigma_{pp} \cup \sigma_{sc}$ is the singular part of the spectrum.

Therefore the condition for the single particle excitation spectrum to be *purely* singular continuous can be written as:

$$\lim_{T\to\infty} \langle\langle A \rangle\rangle_T = 0 \quad \text{(no PP component is present)} \tag{3.10}$$

$$\lim_{\tau\to\infty} C(\tau) \neq 0 \quad \text{(no AC component is present)} \tag{3.11}$$

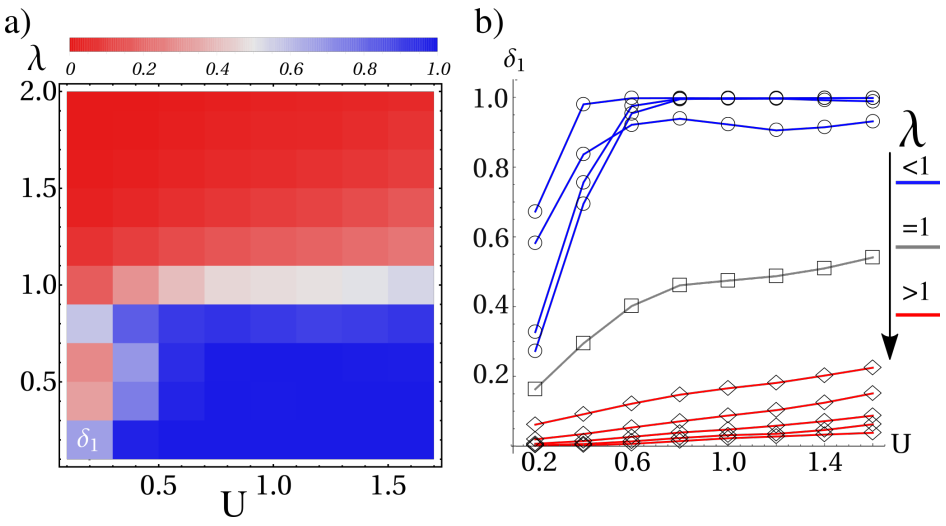

Figure 3.8: a) Exponent of the power-law $\langle |C(\tau)|^2 \rangle_T \propto T^{-\delta_1 t}$ for the interacting OFM as a function of the potential strength λ and interaction U. b) Cuts of the density plot of fig. a) for different value of λ.

It is important to stress that even in the case $\lim_{T\to\infty}\langle\langle A\rangle\rangle_T = 0 \wedge \lim_{\tau\to\infty} C(\tau) = 0$ a singular continuous component can still be present. This is due to the fact that from the Riemann-Lebesgue theorem the condition $\lim_{\tau\to\infty} C(\tau)$ is necessary but not sufficient to guarantee the presence of an AC component. In this respect the conditions 3.10 to detect the presence of a singular continuous component are more strict that what needed.

In the main text we also presented a third quantity, namely the average of the square of the autocollaration function $\langle |C(\tau)|^2 \rangle_T$. This quantity can be used as well to witness the absence of a pure point component through Wiener's lemma: [140]:

$$\lim_{T\to\infty} \langle |C(\tau)|^2 \rangle_T = \sum_k \sigma^2(\lambda_k) \tag{3.12}$$

where $\lambda_k \in \sigma_{pp}$. Basically Wiener's lemma states that the time average of the square of the autocorrelation function is equal to the measure of the pure point part. Therefore $\lim_{T\to\infty}\langle |C(\tau)|^2 \rangle_T = 0$ implies that the spectrum does not contain a pure point part. Assuming a power law decay for this quantity $\langle |C(\tau)|^2 \rangle_T \propto T^{-\delta_1 t}$ we can extract the value of the exponent for the different set of parameters considered in the main text. In Fig. 3.8 we show the result of these fits, which have been done with the same criteria of the other ones in the main text. We can see that the behaviour is similar to that of $\langle\langle \hat{A} \rangle\rangle_T$. Nevertheless this quantity gives non-accurate results on

the time scales accessible with our numerical approach. This can be seen in the region $\lambda \leq 0.8$ and $U < 0.6$ where we expect no PP component at all and therefore $\delta_1 \approx 1$. The reason for such a discrepancy can be easily understood by looking at the original signal $\Delta N(t)$ in this parameter region. It displays oscillations whose amplitude will eventually decay, but on a larger time scale than the one accessible with our numerical simulations. $\langle |C(\tau)|^2 \rangle_T$ is very sensitive to these oscillations and captures an order in the time signal which will eventually disappear at longer times. If we consider this and we use again the $\lambda = 1$ curve as a reference, we see that the region in which the presence of the PP part is absent is similar to that inferred from the behaviour of δ for $\langle \Delta N(t) \rangle_T$.

Conclusions

This thesis discusses a series of works aiming at investigating how the spatial geometry and many-body interactions compete to determine the physical properties of many-body systems, which can be experimentally analyzed in the framework of ultracold gases in optical lattices. To this aim, various observables and systems have been investigated.

The first chapter focuses mainly on the Tonks-Girardeau gas, addressing its static and dynamical properties.In sec. 1.1, the mapping of the many-body wavefunction of the TG gas into that of a non-interacting Fermi gas is reviewed, and it is extended to calculate the single particle Green's function in the time domain.It is shown that with this approach it is possible to recover the equal time quantities, such as density (RSPDM) and momentum distribution (MD). This allows a fast numerical implementation in every spatial potential of both static and dynamical properties of a TG gas. Two different applications are presented in the same chapter. In sec. 1.2 it is reported the study of a TG gas in a quasiperiodic potential. The single particle system shows a metal to insulator transition, with the appearance of the mobility edge if the main lattice lies under a certain threshold. Comparing the static properties of the TG gas (MD and RSPDM) with the those of non-interacting fermions, reveals that a signature of the mobility edge is reflected into many-body measurable properties. Sec. 1.3 focuses on dynamical properties of the TG gas. Numerically implementing the ingredients presented in sec. 1.1 for Green's functions at different times, we have studied the spectral function of the system in a periodic potential. A study of the asymptotic behavior of the SF near the nonanalyticities has been presented ,and the results compared with the existing literature.

In chap. 2, it is examined how the interaction of a Fermi gas in a periodic potential with an impurity influences the long time behavior. The Loschmidt echo, which describes the response of the system to an initial perturbation, is the figure of merit used. We have used two different but complementary methods: a perturbative approach (linked cluster expansion) up to the third order, which provides information about which processes are associated to each observed behavior, and an exact calculation, i. e. the functional determinant approach, which allows us to verify to which order we could truncate the perturbation expansion. We have confirmed that second order

contribution captures the Anderson Orthogonality Catastrophe even in the presence of a lattice, and characterized completely the exponent of the power law behavior. Conversely, we have shown that third order contributions are essential to describe the Fano resonance oscillations, that emerge when the initial chemical potential of the gas approaches the upper band-edge, and the system undergoes an insulating phase.

Finally, in chap. 3, it is shown that the interplay between a quasiperiodic geometry and the many-body interaction of a spinfull Fermi gas gives rise to anomalous propagation properties, which have been recently observed in ultracold gas experiments. We have looked at single-particle correlations functions, distribution of particles and its correlations, after a quench of the hamiltonian that drives the system out of equilibrium. We have sketched a phase diagram for the interacting André-Aubry model. Comparing it with the on-site Fibonacci model, it has been shown that the microscopic mechanism behind the appearance of the critical region, which manifests for intermediate strength of interaction and lattice potential, has to be sought in the singular continuous nature of the single-particle energy spectrum of the AAM.

Bibliography

[1] M. Lewenstein, A. Sanpera, and V. Ahufinger, *Ultracold Atoms in Optical Lattices: Simulating quantum many-body systems*, vol. 1. Oxford University Press, 2012.

[2] I. Bloch, J. Dalibard, and W. Zwerger, "Many-body physics with ultracold gases," *Reviews of Modern Physics*, vol. 80, pp. 885–964, jul 2008.

[3] M. Lewenstein, A. Sanpera, V. Ahufinger, B. Damski, A. Sen(De), and U. Sen, "Ultracold atomic gases in optical lattices: Mimicking condensed matter physics and beyond," *Advances in Physics*, vol. 56, pp. 243–379, mar 2007.

[4] P. Courteille, R. S. Freeland, D. J. Heinzen, F. A. van Abeelen, and B. J. Verhaar, "Observation of a feshbach resonance in cold atom scattering," *Physical Review Letters*, vol. 81, pp. 69–72, jul 1998.

[5] A. Polkovnikov, K. Sengupta, A. Silva, and M. Vengalattore, "Colloquium: Nonequilibrium dynamics of closed interacting quantum systems," *Reviews of Modern Physics*, vol. 83, pp. 863–883, aug 2011.

[6] I. Bloch, J. Dalibard, and S. Nascimbène, "Quantum simulations with ultracold quantum gases," apr 2012.

[7] T. Kinoshita, T. Wenger, and D. S. Weiss, "Observation of a one-dimensional Tonks-Girardeau gas," *Science*, vol. 305, no. 5687, pp. 1125–1128, 2004.

[8] B. Paredes, a. Widera, V. Murg, O. Mandel, S. Foelling, I. Cirac, G. V. Shlyapnikov, T. W. Hansch, and I. Bloch, "Tonks-Girardeau gas of ultracold atoms in an optical lattice," *Nature*, vol. 429, no. 6989, pp. 277–281, 2004.

[9] T. Kinoshita, T. Wenger, and D. S. Weiss, "A quantum Newton's cradle," *Nature*, vol. 440, no. 7086, pp. 900–903, 2006.

[10] A. H. Van Amerongen, J. J. Van Es, P. Wicke, K. V. Kheruntsyan, and N. J. Van Druten, "Yang-Yang thermodynamics on an atom chip," *Physical Review Letters*, vol. 100, no. 9, pp. 13–15, 2008.

[11] S. Palzer, C. Zipkes, C. Sias, and M. Köhl, "Quantum transport through a Tonks-Girardeau gas," *Physical Review Letters*, vol. 103, no. 15, pp. 1–4, 2009.

[12] T. Jacqmin, J. Armijo, T. Berrada, K. V. Kheruntsyan, and I. Bouchoule, "Sub-poissonian fluctuations in a 1D bose gas: From the quantum quasicondensate to the strongly interacting regime," *Physical Review Letters*, vol. 106, no. 23, pp. 1–4, 2011.

[13] M. Girardeau, "Relationship between systems of impenetrable bosons and fermions in one dimension," *Journal of Mathematical Physics*, vol. 1, no. 6, pp. 516–523, 1960.

[14] E. H. Lieb and W. Liniger, "Exact analysis of an interacting bose gas. I. the general solution and the ground state," *Physical Review*, vol. 130, no. 4, pp. 1605–1616, 1963.

[15] E. H. Lieb, "Exact analysis of an interacting bose gas. II. the excitation spectrum," *Physical Review*, vol. 130, no. 4, pp. 1616–1624, 1963.

[16] A. Lenard, "Momentum distribution in the ground state of the one-dimensional system of impenetrable bosons," *Journal of Mathematical Physics*, vol. 5, no. 7, pp. 930–943, 1964.

[17] P. Vignolo and A. Minguzzi, "Universal Contact for a Tonks-Girardeau Gas at Finite Temperature," *Physical Review Letters*, vol. 110, no. 2, pp. 1–5, 2013.

[18] R. Pezer and H. Buljan, "Momentum Distribution Dynamics of a Tonks-Girardeau Gas: Bragg Reflections of a Quantum Many-Body Wave Packet," *Physical Review Letters*, vol. 98, p. 240403, jun 2007.

[19] W. Xu and M. Rigol, "Expansion of one-dimensional lattice hard-core bosons at finite temperature," *Physical Review A*, vol. 95, no. 3, pp. 1–8, 2017.

[20] J. Settino, N. Lo Gullo, A. Sindona, J. Goold, and F. Plastina, "Signatures of the single-particle mobility edge in the ground-state properties of Tonks-Girardeau and noninteracting Fermi gases in a bichromatic potential," *Physical Review A*, vol. 95, p. 033605, mar 2017.

[21] A. Lenard, "One-dimensional impenetrable bosons in thermal equilibrium," *Journal of Mathematical Physics*, vol. 7, no. 7, pp. 1268–1272, 1966.

[22] M. Jimbo, T. Miwa, Y. Môri, and M. Sato, "Density matrix of an impenetrable Bose gas and the fifth Painlevé transcendent," *Physica D: Nonlinear Phenomena*, vol. 1, no. 1, pp. 80–158, 1980.

[23] P. J. Forrester, N. E. Frankel, T. M. Garoni, and N. S. Witte, "Painlev\'e transcendent evaluations of finite system density matrices for 1d impenetrable Bosons," *Communications in Mathematical Physics July 2003, Volume 238, Issue 1–2, pp*, vol. 285, pp. 257–285, 2002.

[24] Y. Castin, "Simple theoretical tools for low dimension Bose gases," *J. Phys. IV France*, vol. 116, pp. 1–47, 2004.

[25] V. I. Yukalov and M. D. Girardeau, "Fermi-Bose mapping for one-dimensional Bose gases," *Laser Physics Letters*, vol. 2, pp. 375–382, aug 2005.

[26] M. Rigol, "Finite-temperature properties of hard-core bosons confined on one-dimensional optical lattices," *Physical Review A - Atomic, Molecular, and Optical Physics*, vol. 72, no. 6, pp. 1–5, 2005.

[27] G. Lang, "Correlations in low-dimensional quantum gases," 2017.

[28] Y. Y. Atas, D. M. Gangardt, I. Bouchoule, and K. V. Kheruntsyan, "Exact nonequilibrium dynamics of finite-temperature Tonks-Girardeau gases," *Physical Review A*, vol. 95, no. 4, pp. 1–6, 2017.

[29] K. K. Das, M. D. Girardeau, and E. M. Wright, "Interference of a Thermal Tonks Gas on a Ring," *Physical Review Letters*, vol. 89, no. 17, pp. 17–20, 2002.

[30] M. Rigol and A. Muramatsu, "Nonequilibrium Dynamics of Tonks–Girardeau Gases on Optical Lattices," *Laser Physics*, vol. 16, no. 2, pp. 348–353, 2006.

[31] R. Boumaza and K. Bencheikh, "Analytical results for the time-dependent current density distribution of expanding ultracold gases after a sudden change of the confining potential," *Journal of Physics A: Mathematical and Theoretical*, vol. 50, no. 50, 2017.

[32] A. Bastianello, M. Collura, and S. Sotiriadis, "Quenches from bosonic Gaussian initial states to the Tonks-Girardeau limit: Stationary states and effects of a confining potential," *Physical Review B*, vol. 95, no. 17, pp. 1–12, 2017.

[33] J. Yago Malo, E. P. Van Nieuwenburg, M. H. Fischer, and A. J. Daley, "Particle statistics and lossy dynamics of ultracold atoms in optical lattices," *Physical Review A*, vol. 97, no. 5, pp. 1–7, 2018.

[34] M. Mikkelsen, T. Fogarty, and T. Busch, "Static and dynamic phases of a Tonks-Girardeau gas in an optical lattice," *arXiv:1808.05478v1*, 2018.

[35] S. Aubry and G. André, "Analyticity breaking and anderson localization in incommensurate lattices," *Ann. Israel Phys. Soc*, vol. 3, no. 133, p. 18, 1980.

[36] P. G. Harper, "Single Band Motion of Conduction Electrons in a Uniform Magnetic Field," *Proceedings of the Physical Society. Section A*, vol. 68, pp. 874–878, oct 1955.

[37] S. Y. Jitomirskaya, "Metal-insulator transition for the almost Mathieu operator," *Annals of Mathematics*, vol. 150, pp. 1159–1175, nov 1999.

[38] M. Modugno, "Exponential localization in one-dimensional quasi-periodic optical lattices," *New Journal of Physics*, vol. 11, p. 033023, mar 2009.

[39] M. Albert and P. Leboeuf, "Localization by bichromatic potentials versus Anderson localization," *Physical Review A - Atomic, Molecular, and Optical Physics*, vol. 81, p. 013614, jan 2010.

[40] C. Aulbach, A. Wobst, G. L. Ingold, P. Hänggi, and I. Varga, "Phase-space visualization of a metal-insulator transition," *New Journal of Physics*, vol. 6, pp. 1–17, jul 2004.

[41] D. R. Grempel, S. Fishman, and R. E. Prange, "Localization in an incommensurate potential: An exactly solvable model," *Physical Review Letters*, vol. 49, pp. 833–836, sep 1982.

[42] G.-L. Ingold, A. Wobst, C. Aulbach, and P. Hänggi, "Delocalization and Heisenberg's uncertainty relation," *The European Physical Journal B*, vol. 30, pp. 175–179, nov 2002.

[43] M. L. Sun, G. Wang, N. B. Li, and T. Nakayama, "Localization-delocalization transition in self-dual quasi-periodic lattices," *EPL*, vol. 110, p. 57003, jun 2015.

[44] N. Lo Gullo and L. Dell'Anna, "Spreading of correlations and Loschmidt echo after quantum quenches of a Bose gas in the Aubry-André potential," *Physical Review A - Atomic, Molecular, and Optical Physics*, vol. 92, p. 063619, dec 2015.

[45] G. Roux, T. Barthel, I. P. McCulloch, C. Kollath, U. Schollwöck, and T. Giamarchi, "Quasiperiodic Bose-Hubbard model and localization in one-dimensional cold atomic gases," *Physical Review A - Atomic, Molecular, and Optical Physics*, vol. 78, p. 023628, aug 2008.

[46] T. Roscilde, "Bosons in one-dimensional incommensurate superlattices," *Physical Review A - Atomic, Molecular, and Optical Physics*, vol. 77, p. 063605, jun 2008.

[47] X. Deng, R. Citro, A. Minguzzi, and E. Orignac, "Phase diagram and momentum distribution of an interacting Bose gas in a bichromatic lattice," *Physical Review A - Atomic, Molecular, and Optical Physics*, vol. 78, p. 013625, jul 2008.

[48] J. Biddle and S. Das Sarma, "Predicted mobility edges in one-dimensional incommensurate optical lattices: An exactly solvable model of anderson localization," *Physical Review Letters*, vol. 104, p. 070601, feb 2010.

[49] J. Biddle, D. J. Priour, B. Wang, and S. Das Sarma, "Localization in one-dimensional lattices with non-nearest-neighbor hopping: Generalized Anderson and Aubry-André models," *Physical Review B - Condensed Matter and Materials Physics*, vol. 83, p. 075105, feb 2011.

[50] D. J. Boers, B. Goedeke, D. Hinrichs, and M. Holthaus, "Mobility edges in bichromatic optical lattices," *Physical Review A - Atomic, Molecular, and Optical Physics*, vol. 75, p. 063404, jun 2007.

[51] R. B. Diener, G. A. Georgakis, J. Zhong, M. Raizen, and Q. Niu, "Transition between extended and localized states in a one-dimensional incommensurate optical lattice," *Physical Review A - Atomic, Molecular, and Optical Physics*, vol. 64, p. 7, aug 2001.

[52] S. Pilati and V. K. Varma, "Localization of interacting Fermi gases in quasiperiodic potentials," *Physical Review A*, vol. 95, p. 013613, jan 2017.

[53] R. Roth and K. Burnett, "Ultracold bosonic atoms in two-colour superlattices," *J. Opt. B*, vol. 5, p. S50, apr 2003.

[54] M. Larcher, F. Dalfovo, and M. Modugno, "Effects of interaction on the diffusion of atomic matter waves in one-dimensional quasiperiodic potentials," *Physical Review A - Atomic, Molecular, and Optical Physics*, vol. 80, p. 053606, nov 2009.

[55] M. C. Gordillo, C. Carbonell-Coronado, and F. De Soto, "Bosonic hard spheres in quasi-one-dimensional bichromatic optical lattices," *Physical Review A - Atomic, Molecular, and Optical Physics*, vol. 91, p. 043618, apr 2015.

[56] M. D. Reichl and E. J. Mueller, "Dynamics of pattern-loaded fermions in bichromatic optical lattices," *Physical Review A*, vol. 93, p. 031601, mar 2016.

[57] B. Damski, J. Zakrzewski, L. Santos, P. Zoller, and M. Lewenstein, "Atomic Bose and Anderson Glasses in Optical Lattices," *Physical Review Letters*, vol. 91, p. 080403, aug 2003.

[58] L. Fallani, J. E. Lye, V. Guarrera, C. Fort, and M. Inguscio, "Ultracold atoms in a disordered crystal of light: Towards a bose glass," *Physical Review Letters*, vol. 98, p. 130404, mar 2007.

[59] V. Guarrera, L. Fallani, J. E. Lye, C. Fort, and M. Inguscio, "Inhomogeneous broadening of a Mott insulator spectrum," *New Journal of Physics*, vol. 9, pp. 107–107, apr 2007.

[60] L. Fallani, C. Fort, and M. Inguscio, "Bose-Einstein Condensates in Disordered Potentials," 2008.

[61] G. Roati, C. D'Errico, L. Fallani, M. Fattori, C. Fort, M. Zaccanti, G. Modugno, M. Modugno, and M. Inguscio, "Anderson localization of a non-interacting Bose-Einstein condensate," *Nature*, vol. 453, pp. 895–898, jun 2008.

[62] L. Tanzi, E. Lucioni, S. Chaudhuri, L. Gori, A. Kumar, C. D'Errico, M. Inguscio, and G. Modugno, "Transport of a bose gas in 1D disordered lattices at the fluid-insulator transition," *Physical Review Letters*, vol. 111, p. 115301, sep 2013.

[63] M. Schreiber, S. S. Hodgman, P. Bordia, H. P. Lüschen, M. H. Fischer, R. Vosk, E. Altman, U. Schneider, and I. Bloch, "Observation of many-body localization of interacting fermions in a quasirandom optical lattice," *Science*, vol. 349, pp. 842–845, aug 2015.

[64] V. V. Volchkov, M. Pasek, V. Denechaud, M. Mukhtar, A. Aspect, D. Delande, and V. Josse, "Measurement of Spectral Functions of Ultracold Atoms in Disordered Potentials," *Physical Review Letters*, vol. 120, no. 6, 2018.

[65] J. T. Stewart, J. P. Gaebler, and D. S. Jin, "Using photoemission spectroscopy to probe a strongly interacting Fermi gas," *Nature*, vol. 454, no. 7205, pp. 744–747, 2008.

[66] A. Damascelli, "Probing the Electronic Structure of Complex Systems by ARPES," *Physica Scripta*, vol. T109, pp. 61–74, 2004.

[67] T. L. Dao, I. Carusotto, and A. Georges, "Probing quasiparticle states in strongly interacting atomic gases by momentum-resolved Raman photoemission spectroscopy," *Physical Review A - Atomic, Molecular, and Optical Physics*, vol. 80, no. 2, pp. 1–10, 2009.

[68] M. Khodas, M. Pustilnik, A. Kamenev, and L. I. Glazman, "Fermi-Luttinger liquid: Spectral function of interacting one-dimensional fermions," *Physical Review B - Condensed Matter and Materials Physics*, vol. 76, no. 15, pp. 1–23, 2007.

[69] A. Imambekov and L. I. Glazman, "Exact exponents of edge singularities in dynamic correlation functions of 1D bose gas," *Physical Review Letters*, vol. 100, no. 20, pp. 1–4, 2008.

[70] A. Imambekov and L. I. Glazman, "Universal theory of nonlinear luttinger liquids," *Science*, vol. 323, no. 5911, pp. 228–231, 2009.

[71] A. Imambekov and L. I. Glazman, "Phenomenology of one-dimensional quantum liquids beyond the low-energy limit," *Physical Review Letters*, vol. 102, no. 12, pp. 12–15, 2009.

[72] A. Imambekov, T. L. Schmidt, and L. I. Glazman, "One-dimensional quantum liquids: Beyond the Luttinger liquid paradigm," *Reviews of Modern Physics*, vol. 84, no. 3, pp. 1253–1306, 2012.

[73] Z. Ristivojevic, "Excitation spectrum of the Lieb-Liniger model," *Physical Review Letters*, vol. 113, no. 1, pp. 0–7, 2014.

[74] L. Markhof and V. Meden, "Spectral function of the Tomonaga-Luttinger model revisited: Power laws and universality," *Physical Review B*, vol. 93, no. 8, pp. 1–16, 2016.

[75] A. Altland and T. Micklitz, "Field Theory Approach to Many-Body Localization," *Physical Review Letters*, vol. 118, p. 127202, mar 2017.

[76] J. Goold, T. Fogarty, N. Lo Gullo, M. Paternostro, and T. Busch, "Orthogonality catastrophe as a consequence of qubit embedding in an ultracold Fermi gas," *Physical Review A - Atomic, Molecular, and Optical Physics*, vol. 84, p. 063632, dec 2011.

[77] A. Sindona, J. Goold, N. Lo Gullo, S. Lorenzo, and F. Plastina, "Orthogonality catastrophe and decoherence in a trapped-fermion environment," *Physical Review Letters*, vol. 111, p. 165303, oct 2013.

[78] A. Sindona, J. Goold, N. Lo Gullo, and F. Plastina, "Statistics of the work distribution for a quenched fermi gas," *New Journal of Physics*, vol. 16, p. 045013, apr 2014.

[79] A. Sindona, M. Pisarra, M. Gravina, C. V. Gomez, P. Riccardi, G. Falcone, and F. Plastina, "Statistics of work and orthogonality catastrophe in discrete level systems: An application to fullerene molecules and ultra-cold trapped Fermi gases," *Beilstein Journal of Nanotechnology*, vol. 6, pp. 755–766, mar 2015.

[80] M. A. Cazalilla, R. Citro, T. Giamarchi, E. Orignac, and M. Rigol, "One dimensional bosons: From condensed matter systems to ultracold gases," *Reviews of Modern Physics*, vol. 83, no. 4, pp. 1405–1466, 2011.

[81] G. Stefanucci and R. van Leeuwen, *Nonequilibrium Many-Body Theory of Quantum Systems*, vol. 54. 2013.

[82] L. S. Levitov, H. Lee, and G. B. Lesovik, "Electron counting statistics and coherent states of electric current," *Journal of Mathematical Physics*, vol. 37, pp. 4845–4866, jun 1996.

[83] I. Klich, "An Elementary Derivation of Levitov's Formula," in *Quantum Noise in Mesoscopic Physics*, pp. 397–402, Dordrecht: Springer Netherlands, 2003.

[84] P. W. Anderson, "Infrared catastrophe in fermi gases with local scattering potentials," *Physical Review Letters*, vol. 18, pp. 1049–1051, jun 1967.

[85] P. W. Anderson and G. Yuval, "Exact results in the kondo problem: Equivalence to a classical one-dimensional coulomb gas," *Physical Review Letters*, vol. 23, pp. 89–92, jul 1969.

[86] P. W. Anderson, G. Yuval, and D. R. Hamann, "Exact results in the Kondo problem. II. Scaling theory, qualitatively correct solution, and some new results on one-dimensional classical statistical models," *Physical Review B*, vol. 1, pp. 4464–4473, jun 1970.

[87] G. D. Mahan, "Excitons in metals: Infinite hole mass," *Physical Review*, vol. 163, pp. 612–617, nov 1967.

[88] P. Nozieres, J. Gavoret, and B. Roulet, "Singularities In X-Ray Absorption and Emission Of Metals .2. Self-Consistent Treatment Of Divergences," *Phys. Rev.*, vol. 178, pp. 1084—-&, feb 1969.

[89] D. Shechtman, I. Blech, D. Gratias, and J. W. Cahn, "Metallic phase with long-range orientational order and no translational symmetry," *Physical Review Letters*, vol. 53, pp. 1951–1953, nov 1984.

[90] A. P. Tsai, A. Inoue, and T. Masumoto, "A stable quasicrystal in al-cu-fe system," *Japanese Journal of Applied Physics*, vol. 26, pp. 1505–1507, sep 1987.

[91] J.-M. Dubois, "Useful Quasicrystals," in *Useful Quasicrystals*, pp. 167–243, WORLD SCIENTIFIC, apr 2005.

[92] S. Roche, G. T. De Laissardière, and D. Mayou, "Electronic transport properties of quasicrystals," *Journal of Mathematical Physics*, vol. 38, pp. 1794–1822, jun 1997.

[93] P. J. Steinhardt, "Quasicrystals: A brief history of the impossible," in *Rendiconti Lincei*, vol. 24, pp. 85–91, feb 2013.

[94] J. X. Zhong and R. Mosseri, "Quantum dynamics in quasiperiodic systems," *Journal of Physics: Condensed Matter*, vol. 7, pp. 8383–8404, oct 1995.

[95] R. Ketzmerick, G. Petschel, and T. Geisel, "Slow decay of temporal correlations in quantum systems with Cantor spectra," *Physical Review Letters*, vol. 69, pp. 695–698, aug 1992.

[96] N. Lo Gullo, C. V. Ambarish, T. Busch, L. Dell'Anna, and C. M. Chandrashekar, "Dynamics and energy spectra of aperiodic discrete-time quantum walks," *Physical Review E*, vol. 96, p. 012111, jul 2017.

[97] A. Avila and S. Jitomirskaya, "The ten Martini problem," *Annals of Mathematics*, vol. 170, pp. 303–342, jul 2009.

[98] H. P. Lüschen, P. Bordia, S. Scherg, F. Alet, E. Altman, U. Schneider, and I. Bloch, "Observation of Slow Dynamics near the Many-Body Localization Transition in One-Dimensional Quasiperiodic Systems," *Physical Review Letters*, vol. 119, p. 260401, dec 2017.

[99] P. Naldesi, E. Ercolessi, and T. Roscilde, "Detecting a many-body mobility edge with quantum quenches," *SciPost Physics*, vol. 1, p. 010, oct 2016.

[100] H. Moritz, T. Stöferle, M. Köhl, and T. Esslinger, "Exciting collective oscillations in a trapped 1d gas," *Physical Review Letters*, vol. 91, p. 250402, dec 2003.

[101] M. Olshanii, "Atomic scattering in the presence of an external confinement and a gas of impenetrable bosons," *Physical Review Letters*, vol. 81, pp. 938–941, aug 1998.

[102] H. G. Vaidya and C. A. Tracy, "One-particle reduced density matrix of impenetrable bosons in one dimension at zero temperature," *Physical Review Letters*, vol. 42, pp. 3–6, jan 1979.

[103] G. J. Lapeyre, M. D. Girardeau, and E. M. Wright, "Momentum distribution for a one-dimensional trapped gas of hard-core bosons," *Physical Review A - Atomic, Molecular, and Optical Physics*, vol. 66, pp. 1–6, aug 2002.

[104] M. D. Girardeau, E. M. Wright, and J. M. Triscari, "Ground-state properties of a one-dimensional system of hard-core bosons in a harmonic trap," *Physical Review A - Atomic, Molecular, and Optical Physics*, vol. 63, pp. 1–6, feb 2001.

[105] A. Minguzzi, P. Vignolo, and M. P. Tosi, "High-momentum tail in the Tonks gas under harmonic confinement," *Physics Letters, Section A: General, Atomic and Solid State Physics*, vol. 294, pp. 222–226, feb 2002.

[106] T. Papenbrock, "Ground-state properties of hard-core bosons in one-dimensional harmonic traps," *Physical Review A - Atomic, Molecular, and Optical Physics*, vol. 67, p. 4, apr 2003.

[107] P. J. Forrester, N. E. Frankel, T. M. Garoni, and N. S. Witte, "Finite one-dimensional impenetrable Bose systems: Occupation numbers," *Physical Review A - Atomic, Molecular, and Optical Physics*, vol. 67, p. 17, apr 2003.

[108] G. P. Berman, F. Borgonovi, F. M. Izrailev, and A. Smerzi, "Irregular Dynamics in a One-Dimensional Bose System," *Physical Review Letters*, vol. 92, p. 4, jan 2004.

[109] A. Minguzzi and D. M. Gangardt, "Exact coherent states of a harmonically confined tonks-girardeau gas," *Physical Review Letters*, vol. 94, p. 240404, jun 2005.

[110] M. Rigol and A. Muramatsu, "Expansion of Tonks-Girardeau gases on a one-dimensional optical lattice," in *AIP Conference Proceedings*, vol. 850, pp. 47–48, aug 2006.

[111] M. Rigol and A. Muramatsu, "Fermionization in an expanding 1D gas o hard-core bosons," *Opt. ˜ Commun. ˜*, vol. 243, p. 33, jun 2004.

[112] M. Rigol, V. Dunjko, V. Yurovsky, and M. Olshanii, "Relaxation in a completely integrable many-body Quantum system: An Ab initio study of the dynamics of the highly excited states of 1D lattice hard-core bosons," *Physical Review Letters*, vol. 98, p. 050405, feb 2007.

[113] M. Pillai, J. Goglio, and T. G. Walker, "Matrix Numerov method for solving Schrödinger's equation," *American Journal of Physics*, vol. 80, pp. 1017–1019, nov 2012.

[114] E. Maciá, "Physical nature of critical modes in fibonacci quasicrystals," *Physical Review B - Condensed Matter and Materials Physics*, vol. 60, pp. 10032–10036, oct 1999.

[115] P. Nozières and C. T. De Dominicis, "Singularities in the X-ray absorption and emission of metals. III. One-body theory exact solution," *Physical Review*, vol. 178, pp. 1097–1107, feb 1969.

[116] R. Schmidt, M. Knap, D. A. Ivanov, J. S. You, M. Cetina, and E. Demler, "Universal many-body response of heavy impurities coupled to

a Fermi sea: A review of recent progress," *Reports on Progress in Physics*, vol. 81, p. 024401, feb 2018.

[117] N. Lo Gullo and L. Dell'Anna, "Spreading of correlations and Loschmidt echo after quantum quenches of a Bose gas in the Aubry-André potential," *Physical Review A - Atomic, Molecular, and Optical Physics*, vol. 92, p. 063619, dec 2015.

[118] R. D. Mattuck, *A guide to Feynman diagrams in the many-body problem*. New York: McGraw-Hil, second edi ed., 1976.

[119] S. Doniach and E. H. Sondheimer, *Green's Functions for Solid State Physicists*. published by imperial college press and distributed by world scientific publishing co., jun 1998.

[120] B. Roulet, J. Gavoret, and P. Nozières, "Singularities in the X-ray absorption and emission of metals. I. First-order parquet calculation," *Physical Review*, vol. 178, pp. 1072–1083, feb 1969.

[121] R. Brako and D. M. Newns, "The electron-hole mechanism for sticking of adsorbates: A soluble model," *Solid State Communications*, vol. 33, pp. 713–715, feb 1980.

[122] K. Schönhammer and O. Gunnarsson, "Sticking probability on metal surfaces: Contribution from electron-hole-pair excitations," *Physical Review B*, vol. 22, pp. 1629–1637, aug 1980.

[123] R. Brako and D. M. Newns, "Slowly varying time-dependent local perturbations in metals: A new approach," *Journal of Physics C: Solid State Physics*, vol. 14, pp. 3065–3078, jul 1981.

[124] K. D. Schotte and U. Schotte, "Tomonaga's Model and the Threshold Singularity of X-Ray Spectra of Metals," *Physical Review*, vol. 182, pp. 479–482, jun 1969.

[125] A. Süto, "Singular continuous spectrum on a cantor set of zero Lebesgue measure for the Fibonacci Hamiltonian," *Journal of Statistical Physics*, vol. 56, pp. 525–531, aug 1989.

[126] J. P. Ronzheimer, M. Schreiber, S. Braun, S. Hodgman, S. Langer, I. P. McCulloch, F. Heidrich-Meisner, I. Bloch, and U. Schneider, "Expansion dynamics of interacting bosons in homogeneous lattices in one and two dimensions," *Physical Review Letters*, vol. 110, p. 205301, may 2013.

[127] N. W. Talarico, S. Maniscalco, and N. Lo Gullo, "A Scalable Numerical Approach to the Solution of the Dyson Equation for the Non-Equilibrium Single-Particle Green's Function," *physica status solidi (b)*, p. 1800501, mar 2019.

[128] A. Stan, N. E. Dahlen, and R. Van Leeuwen, "Time propagation of the Kadanoff-Baym equations for inhomogeneous systems," *Journal of Chemical Physics*, vol. 130, p. 224101, jun 2009.

[129] R. A. Lynn and R. Van Leeuwen, "Development of non-equilibrium Green's functions for use with full interaction in complex systems," in *Journal of Physics: Conference Series*, vol. 696, p. 012020, IOP Publishing, mar 2016.

[130] N. Lo Gullo and L. Dell'Anna, "Self-consistent Keldysh approach to quenches in the weakly interacting Bose-Hubbard model," *Physical Review B*, vol. 94, p. 184308, nov 2016.

[131] E. H. Lieb and D. W. Robinson, "The finite group velocity of quantum spin systems," *Communications in Mathematical Physics*, vol. 28, pp. 251–257, sep 1972.

[132] J. M. Luck, "Cantor spectra and scaling of gap widths in deterministic aperiodic systems," *Physical Review B*, vol. 39, pp. 5834–5849, mar 1989.

[133] M. Queffélec, *Substitution Dynamical Systems - Spectral Analysis*, vol. 1294 of *Lecture Notes in Mathematics*. Berlin, Heidelberg: Springer Berlin Heidelberg, 2010.

[134] N. Lo Gullo, L. Vittadello, M. Bazzan, and L. Dell'Anna, "Equivalence classes of Fibonacci lattices and their similarity properties," *Physical Review A*, vol. 94, p. 023846, aug 2016.

[135] N. L. Gullo, L. Vittadello, L. Dell'Anna, M. Merano, N. Rossetto, and M. Bazzan, "A study of the brightest peaks in the diffraction pattern of Fibonacci gratings," *Journal of Optics (United Kingdom)*, vol. 19, p. 055613, may 2017.

[136] Y. Last, "Quantum dynamics and decompositions of singular continuous spectra," *Journal of Functional Analysis*, vol. 142, pp. 406–445, dec 1996.

[137] A. S. Pikovsky, M. A. Zaks, U. Feudel, and J. Kurths, "Singular continuous spectra in dissipative dynamics," *Physical Review E*, vol. 52, pp. 285–296, jul 1995.

[138] H. Hiramoto and M. Kohmoto, "Electronic spectral and wavefunction properties of one-dimensional quasiperiodic systems: a scaling approach," *International Journal of Modern Physics B*, vol. 06, pp. 281–320, feb 1992.

[139] M. Reed and B. Simon, *Methods of Modern Mathematical Physics III: Scattering theory*. 1979.

[140] W. Amrein, *Non-relativistic quantum dynamics*, vol. 2. Reidel Dordrecht, 1981.